A Test Facility for New Non-Rare-Earth Pulse Tube Cryocooler Regenerator Plates

by

Eric Alar

A thesis submitted in partial fulfillment of
the requirements for the degree of

Master of Science

(Mechanical Engineering)

at the

UNIVERSITY OF WISCONSIN – MADISON

2013

This page intentionally left blank

APPROVED BY

_____

PROFESSOR SANFORD A. KLEIN

_____

PROFESSOR GREGORY F. NELLIS

DATE:_____

This page intentionally left blank

Abstract

Pulse tube cryocoolers are a type of refrigeration system being used in high-speed computing, superconducting magnets, infrared technology for national defense and weather science, and many other areas. One major limiting factor behind the cooling power and the efficiency of these devices are their regenerators. A new type of non-rare-earth regenerator is being developed that could be significantly more efficient than previous regenerators. A quantitative method that could show that the new proprietary regenerator is better than others currently being used is needed; this method is the main focus of the research.

This thesis explains the modeling, construction, and the testing of the regenerator facility that is meant to work with helium at 4.2 K and 1 MPa of pressure. The most important property of the regenerator is its specific heat capacity, although due to the adsorption property of the proprietary material, a traditional vacuum calorimeter cannot be used to measure this. Therefore, a method that measures the thermal diffusive time constant and then calculates specific heat using conductivity and density of the proprietary material has been developed. The facility was modeled, constructed, and tested.

The test that was performed verified the difference in thermal diffusivity between stainless steel 304L and copper RRR 50 at cryogenic temperatures inside the test facility. The difference in diffusivities was shown by the test apparatus and many things were discovered about the test method that will make future runs more accurate. Although the proprietary material has not yet been successfully delivered, this test facility and test method should be able to show that a difference exists between the proprietary regenerator and a control specimen.

Acknowledgments

First of all I would like to thank Greg Nellis, as my main advisor throughout this project. The level of intellectual and academic rigor that he maintains has been inspirational to me as a student and as a human. Writing this thesis was important, but the sound reasoning Greg challenged me to on a daily basis might have been more important. I cannot say enough.

Secondly, I would like to thank Sandy Klein, who hired me so fast for this degree that I could not say no. I can only wish to be as genuinely curious-and correct-about the world. Sandy has motivated me to become much more efficient with my time; the amount of things he can get done in a day is unbelievable. Few instructors exist who possess all of the qualities Sandy does. After this degree, before I write, say, or do anything, I will say out loud to myself, "Why?"

A few people went out of their way to help me with my experiment. Gabe Bernhardt helped me so many times; he is a cryogenic wizard and a great guy. John Pfotenhauer was very generous with his infinitely deep pool of experimental knowledge; his cryogenics class was extremely useful. Brad Moore dropped everything he was doing to help me with my facility on multiple occasions, thank you so much man. Diego Fonseca is a great engineer, he could probably pull 10^{-5} torr on a wooden house. Franklin Miller, I wish I would have gotten to work with you more, thank you for the hilarious conversations. Rogelio Rosas, thanks for the Friday night BF3 sessions.

I could list off individual things each of these Solar Energy Lab students did to help me or boost my mood on a rainy day, but I'd much rather meet at the library to discuss such matters. Thanks to the following: Amir Jahromi, Greg Marsicek, Amanda Pertzborn, Dan Schick, Doug Gavic, Russell Knudson, Kendra Passow, Mark Rodarte, Wenjie Zhou, John Dyreby, Dongsheng

Zhang, Nevzat Akkurt, John Edlebeck, Brad Knier, Rodrigo Barraza, Bill Brey, Brian Leyde, and Nathan Haggerty.

I would like to thank the Wisconsin Space Grant Consortium for providing financial support.

Lastly, thanks to my family: Nicole and Mom. Although some friends were not willing to wait to see me through this, I was lucky to have you two to encourage me when times were tough.

Table of Contents

Table of Figures

List of Tables

Nomenclature

Section 1

c_p	specific heat capacity at constant pressure (J/kg-K)
∂h	differential specific enthalpy (J/kg)
∂T	differential temperature (K)
p	pressure (Pa)
h	enthalpy (J/kg)
u	specific internal energy (J/kg)
pv	work term associated with change in volume at constant pressure (J/kg)
∂u	differential specific internal energy (J/kg)
∂pv	differential pressure-volume work term (J/kg)
c_v	specific heat capacity at constant volume (J/kg-K)
α_1	volume expansion coefficient (1/K)
T	temperature (K)
v	Specific volume (m^3/kg)
β	volume expansion coefficient (m^2/N)
Q	energy required to heat calorimeter and sample (J)
Q_0	energy required to heat just the bomb and copper sleeve (J)
m	mass (kg)
ΔT	change in temperature (K)
T_g	glass transition temperature (K)
T_c	crystallization temperature (K)
T_m	melting temperature (K)
q	heat flow (W)

c	specific heat capacity (J/kg-K)
α	thermal diffusivity (m^2/s)
k	conductivity (W/m-K)
ρ	density (kg/m^3)
$T_{Initial}$	initial temperature of an infinitely long solid (K)
T_{Hot}	temperature on the hot side of an infinitely long solid (K)
t_N	the time of a thermal penetration depth (s)
δ_N	the thermal penetration depth (m)
t	time (s)
L	length (m)

Section 2

τ	thermal diffusive time constant (s)
k_p	overall average conductivity of a composite plate (W/m-K)
k_{he}	conductivity of the helium (W/m-K)
k_{ads}	conductivity of the adsorbent (W/m-K)
k_{si}	conductivity of the silicon (W/m-K)
A_{chan}	cross sectional area (void space) of the involute channels (m^2)
A_{ads}	cross sectional area of the adsorbent center (m^2)
A_o	cross sectional area of the outer ring of just silicon (m^2)
A_{total}	total cross sectional area of the channels, silicon, and adsorbent (m^2)
$k_{si,pl}$	overall effective conductivity of the silicon plate (W/m-K)
$\dot{q}$	heat flow through the regenerator (W)
R	thermal resistance (K/W)

k_{eff}	effective conductivity of composite regenerator (W/m-K)
k_{nylon}	conductivity of nylon PA66 (W/m-K)
th_{nyl}	thickness of the nylon sections (m)
th_{sil}	thickness of the silicon layer (m)
th_{p}	thickness of the composite plate (m)
ρ_{eff}	total effective density of plates and spacer (kg/m^3)
ρ_{nyl}	density of nylon (kg/m^3)
ρ_{si}	density of silicon (kg/m^3)
ρ_{ads}	density of adsorbent (kg/m^3)
ρ_{he}	density of helium (kg/m^3)
V_{spacer}	volume of nylon spacer (m^3)
V_{o}	volume of outer silicon (m^3)
V_{ads}	volume of inner adsorbent (m^3)
V_{chans}	volume of the involute channels (m^3)
V_{total}	volume of adsorbent, silicon, and channels (m^3)
$V_{sil,spv}$	volume of just the silicon in the 100 μm silicon section (m^3)
N	number of plates (-)
C	total heat capacity of regenerator with spacers (J/K)
c_{eff}	effective specific heat capacity of regenerator with spacers (J/kg-K)
V_{stack}	volume of the total composite stack (m^3)
R_{nylon}	thermal resistance of the nylon (K/W)
R_{pl}	thermal resistance of the plate (K/W)
$R_{si,pl}$	thermal resistance of the silicon plate (K/W)
Cap_{nylon}	capacitance of the nylon section (J/K)

Cap_p	the capacitance of the composite plate (J/K)
$Cap_{si,pl}$	the capacitance of the silicon plate (J/K)
t_{regen}	time response of the proprietary regenerator (s)
$t_{control}$	time response of a control regenerator (s)
c_{regen}	the specific heat capacity of the proprietary regenerator (J/kg-K)
$c_{control}$	the specific heat capacity of a control regenerator (J/kg-K)
c_{calc}	calculated specific heat capacity (J/kg-K)
t_{meas}	thermal diffusive time measurement (s)

Section 3

ε_B	emissivity of the base of the Dewar (-)
A	cross sectional area of the radiation shields (m^2)
ε_N	emissivity of the aluminum radiation shields (-)
ε_T	emissivity of the base of the stainless steel top plate (-)
$F_{B,1}$	view factor between the base and the first radiation shield (-)
$F_{N,N+1}$	view factor between successive radiation shields (-)
$F_{N,T}$	view factor between the last shields and the top plate (-)
Q	radiation heat transfer between the top plate and the bottom of the Dewar (W)
Eb_B	blackbody emissive power of the bottom of the Dewar (W/m^2)
Eb_T	blackbody emissive power of the top plate (W/m^2)
R_{total}	total special resistance ($1/m^2$)
T_{Top}	temperature of the top plate (K)
T_{Bottom}	temperature of the bottom plate (K)
σ	Stefan-Boltzmann constant ($W/m^2\text{-}K^4$)

q_{cond}	axial conduction heat transfer (W)
k_{int}	integrated thermal conductivity (W/m)
A_{tot}	cross sectional area of a support member (m^2)
L	length of a support member (m)
V_{meas}	measured voltage across a temperature sensor (V)

Section 4

t	time (s)
δ	the thermal penetration depth (m)
α	thermal diffusivity (m^2/s)
c	specific heat capacity (J/kg-K)
k	conductivity (W/m-K)
ρ	density (kg/m^3)
τ	thermal diffusive time constant (s)

Section 5

$t_{1/2}$	half-rise time of thermal wave (s)

This page intentionally left blank

1 Introduction

1.1 Applications of Pulse Tube Crycoolers

Pulse tube cryocoolers (PTCs) are a type of refrigeration system that provide cooling at temperatures at or below 120 K. They have no moving parts in their cold end, making them more reliable than other low temperature refrigeration systems. PTCs can be as small as a few hundred millimeters in length and as large as 50 feet long. A mini pulse tube cryocooler is shown in Figure 1.1.

Figure 1.1: A type of pulse tube crycooler that can provide cooling at temperatures between 10-80 K and cooling powers between 300 mW and 5 W (Air Liquid 2010).

The applications of pulse tube cryocoolers are myriad. The military uses PTCs to cool the infrared sensors used in missile guidance and detection. Infrared sensors used to analyze the atmosphere for global warming effects also have been cooled using PTCs. Semiconductor fabrication and the use of these in high speed computers both require cooling that has been provided by PTCs. The medical industry has used PTCs to cool superconducting magnets in MRI machines, to liquefy oxygen in portable home units and at hospitals, and for cryosurgery. The liquefaction of natural gas has been accomplished using a Thermo-Acoustic Driven Orifice Pulse Tube Refrigerator (TADOPTR) that provides 2.0 kW of cooling power at 120 K. Many

other industries that require the cooling of superconducting magnets also use pulse tube refrigerators (Radebaugh 2000). PTCs will be discussed in greater detail in Section 1.4.

1.2 Thermal Properties

1.2.1 Specific Heat Capacity

Specific heat capacity is defined as the energy required to raise the temperature of a unit of mass one degree. In the SI system, specific heat capacity has units J/kg-K. Specific heat capacity can be defined either at constant pressure, c_p, or constant volume, c_v (Janna 2009). For many solids, only one value of specific heat is reported; this is explained in Equations 1.1-1.5. Specific heat at constant pressure is defined by Equation 1.1.

$$c_p = \left(\frac{\partial h}{\partial T} \right)_p \tag{1.1}$$

where h is specific enthalpy, T is temperature, and p is pressure.

Specific enthalpy is defined by Equation 1.2.

$$h = u + p\,v \tag{1.2}$$

Substituting Eq. 1.2 into Eq. 1.1 produces Eq. 1.3.

$$c_p = \left(\frac{\partial u}{\partial T} \right)_p + \left(\frac{\partial pv}{\partial T} \right)_p \tag{1.3}$$

In Equation 1.3, the product pv barely changes for solids in most temperature ranges, therefore the second derivative on the right side is nearly zero and Equation 1.3 becomes:

$$c_p = \left(\frac{\partial u}{\partial T} \right)_p \tag{1.4}$$

Specific heat capacity at constant volume is defined by Equation 1.5.

$$c_v = \left(\frac{\partial u}{\partial T} \right)_v \tag{1.5}$$

Since most solids are essentially incompressible, even if pressure is kept constant when measuring specific heat as shown in Equation 1.4, the volume will remain nearly constant for solids. This is equivalent to saying that c_v and c_p are nearly identical for solids. This becomes an even better assumption at low temperatures because the difference in c_p and c_v, represented in Equation 1.6, approaches zero as temperature decreases.

$$c_p - c_v = \frac{\alpha_1^2 T v}{\beta} \tag{1.6}$$

where β is the compressibility, T is the temperature, v is the specific volume, and α_1 is the volume expansion coefficient of a substance (Pillai 2005).

Specific heat in solids can be measured using a few different techniques. An objective of this project is to measure the specific heat of a novel material under unique conditions. Therefore these alternative measurement techniques will be described here.

One strategy for measuring specific heat capacity is by using an adiabatic calorimeter. Although nothing is truly adiabatic, the objective of such a device is to attempt to eliminate heat transfer between an object that is being heated and its test chamber. Figure 1.2 shows an example of a low temperature adiabatic calorimeter.

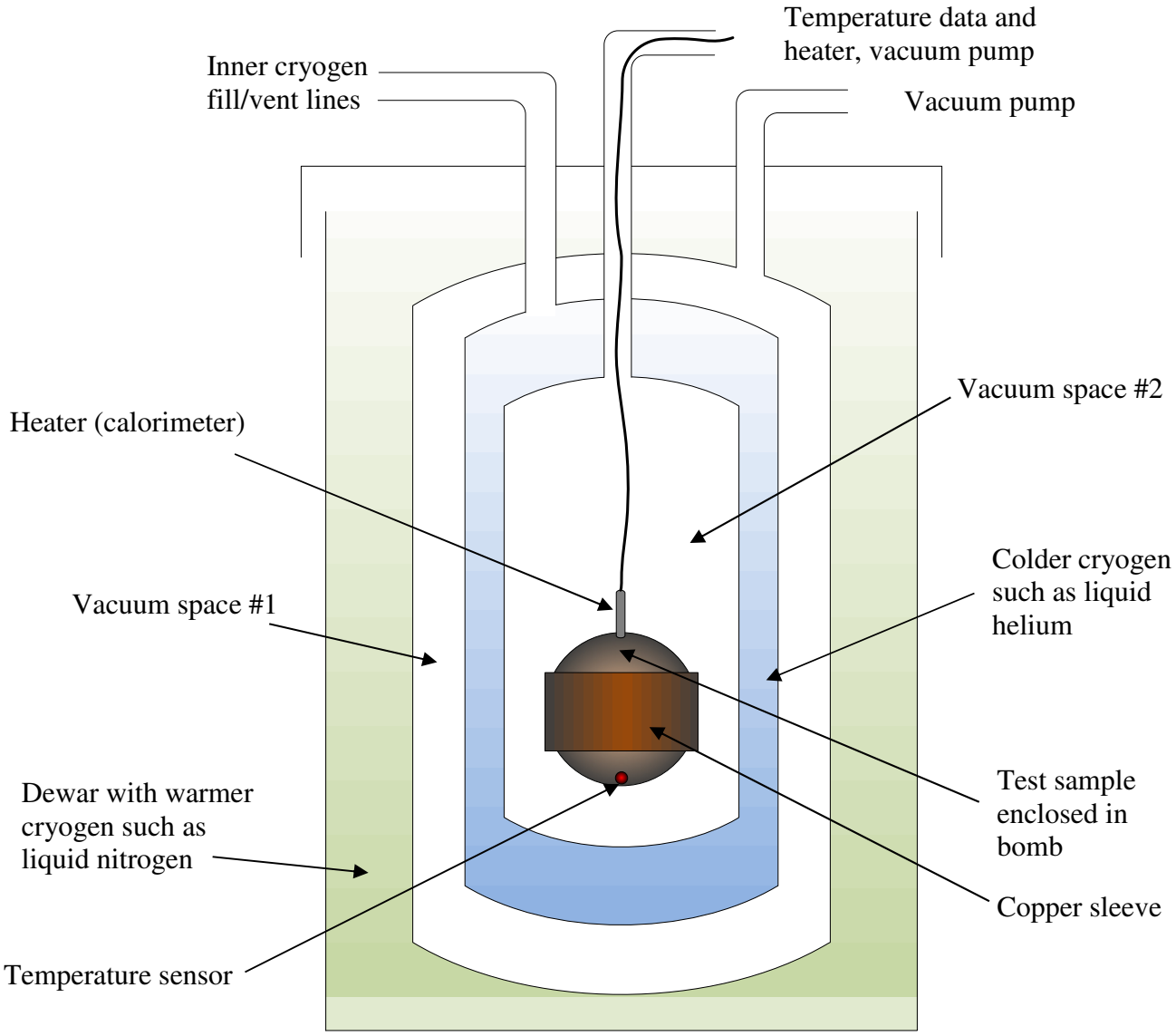

Figure 1.2: An adiabatic low temperature calorimeter used in measuring the specific heat of a solid.

The spherical bomb is just the bomb container and copper sleeve at first, containing no test specimen; energy is added until a specified temperature is achieved. The bomb is kept nearly isothermal by a copper jacket. Then, the test is repeated with the test sample inside of the bomb. There are very few residual gas molecules inside of the inner vacuum space that is maintained at approximately $2.5 * 10^{-5}$ torr, therefore, almost no convection heat transfer can occur between the bomb and the inner chamber walls. Also, to eliminate radiation heat transfer between the

bomb and the inner walls, a temperature controller is used to maintain the chamber walls at the same temperature as the bomb. The amount of energy required to heat the inner apparatus is measured and the specific heat is calculated using Equation 1.6.

$$c = \frac{Q - Q_0}{m \Delta T} \tag{1.6}$$

where Q is the energy required to heat the bomb and the sample, Q_0 is the energy required to heat just the bomb and copper sleeve, m is the mass of the test material, and ΔT is the temperature rise (Goodwin 1961, Magee 1991).

Another technique used to measure specific heat is called differential scanning calorimetry. Two containers are simultaneously heated; one contains a test sample and the other is empty, as shown in Figure 1.3.

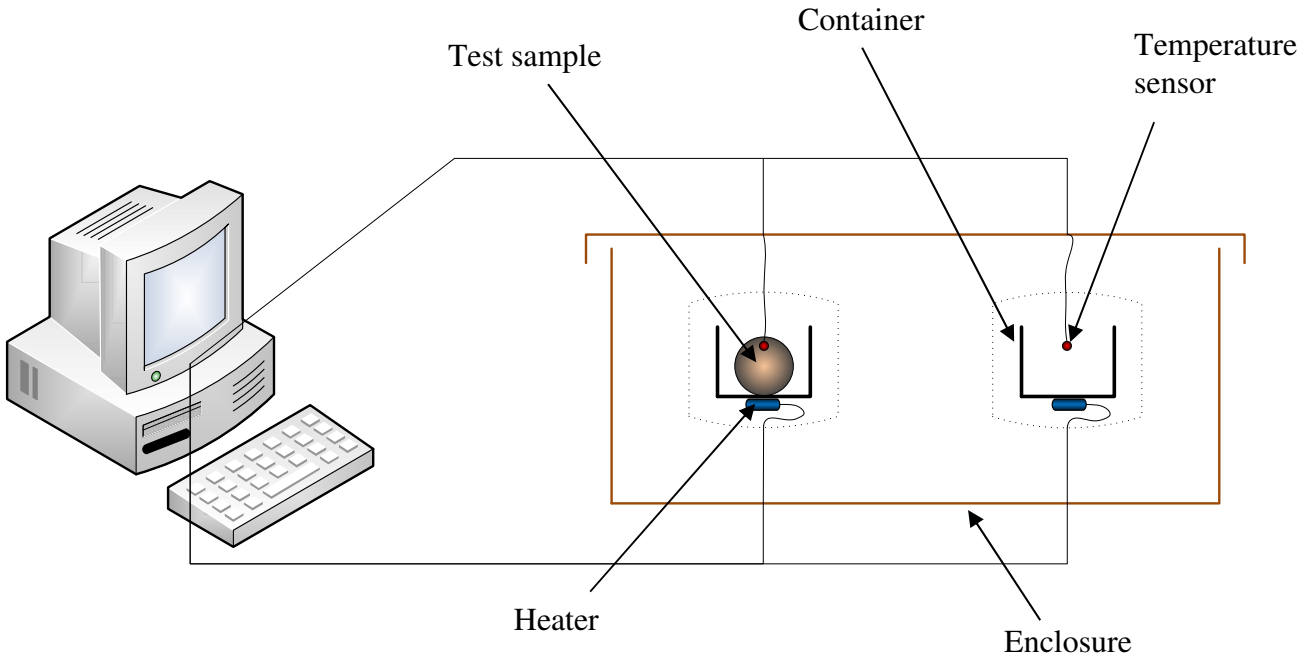

Figure 1.3: A simplified diagram of a differential scanning calorimeter.

The container with the test sample will require more energy to reach the same temperature as the empty container; this additional energy is recorded as a function of the set temperature of the system. A typical differential scanning calorimeter (DSC) plot is shown in Figure 1.4.

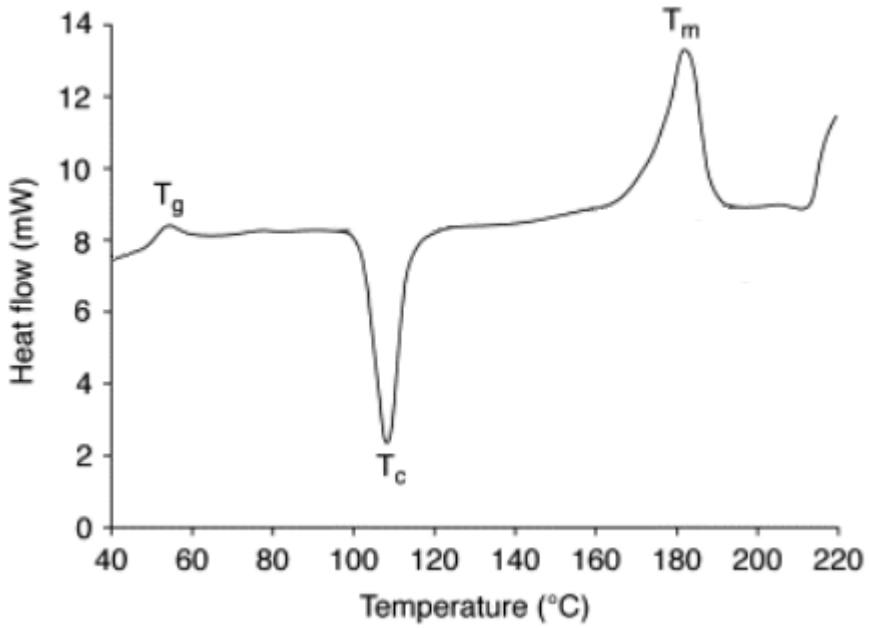

Figure 1.4: An example of a readout from a differential scanning calorimeter. Heat flow is shown as a function of temperature. T_g, T_c, and T_m refer to glass transition, crystallization, and melting temperatures of a polymer that is typically measured in a DSC (Clas 1999).

The information shown in Figure 1.4 can be used to obtain specific heat at nearly any point within the temperature range when heat flow has a positive slope with respect to temperature. Heat flow is also known as a function of time, so integrating heat flow with respect to time produces a unit of energy q. The temperature at each time boundary is known, and therefore the integral energy term can be divided by the ΔT (i.e., change in temperature) between each time to obtain specific heat, as shown in Equation 1.7.

$$\frac{q}{m\Delta T} = c \tag{1.7}$$

The mass of the substance being measured is represented by m.

Another method of indirectly measuring specific heat is described in Section 1.2.2.

1.2.2 Thermal Diffusivity

Thermal diffusivity is an intensive thermal property that is defined as the thermal conductivity divided by the product of density and specific heat capacity, as shown by Equation 1.8.

$$\alpha = \frac{k}{\rho c} \tag{1.8}$$

The thermal diffusivity behavior of copper and nylon over a wide temperature range is shown in Figure 1.5.

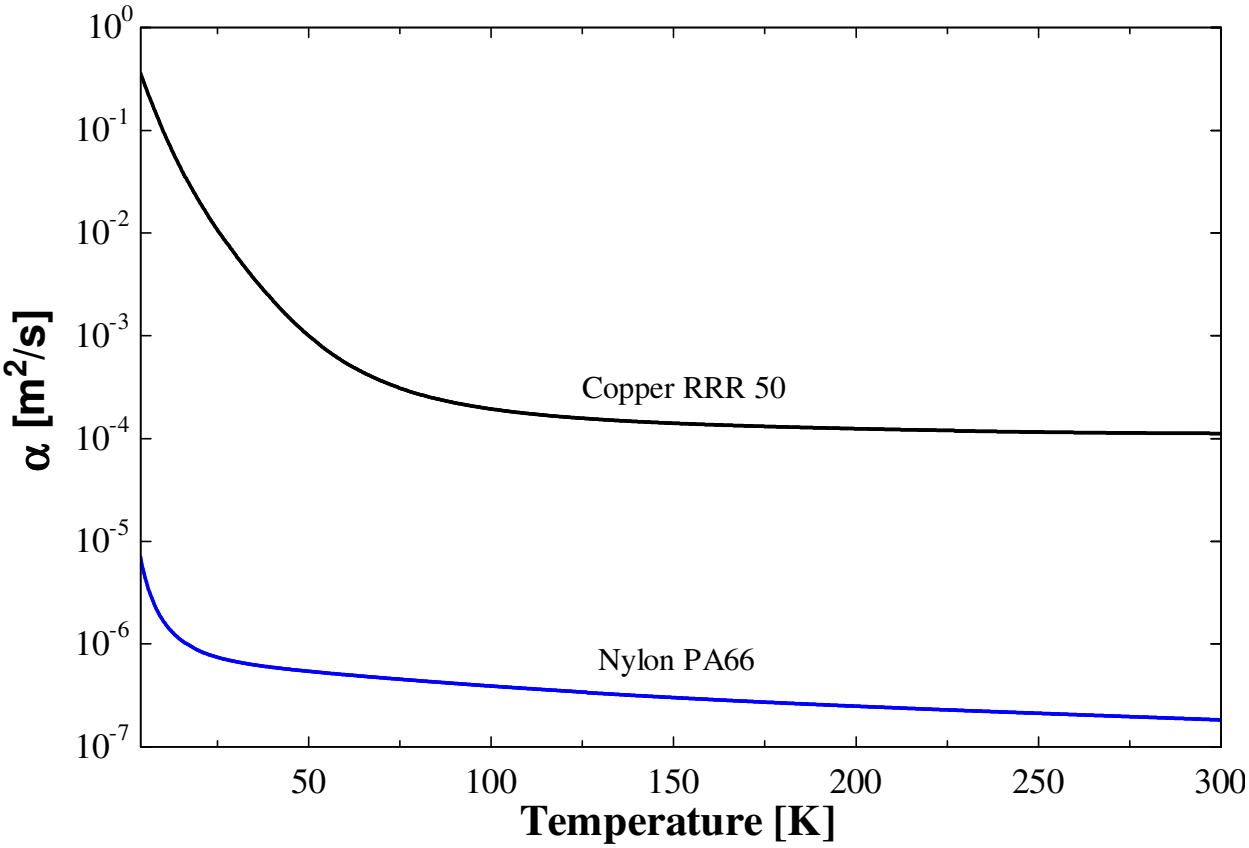

Figure 1.5: The thermal diffusivity of copper RRR 50 and nylon PA66 as a function of temperature between 4 and 300 K (Marquardt 2000).

A material such as copper shown in Figure 1.5 allows heat to travel rapidly through it because of its higher thermal diffusivity, while heat flows slowly through a substance such as nylon.

One technique that exists to measure the thermal diffusivity of materials is the flash method. In the flash method, a high-intensity, short burst of radiant energy is applied to a uniform surface area on a homogeneous substance. Temperature on the opposite side of the few-millimeter thick sample is recorded by thermocouples and imaging devices. By analyzing the shape of the resulting curve, an estimate of thermal diffusivity can be made. At room temperature with pure substances, specific heat and thermal conductivity have been predicted as well (Parker 1961). The same technique has been used to measure the thermal diffusivity of

copper at 77 K (Penco 2001). The measuring technique used in this experiment is similar to the flash method, as described in Section 2.

1.2.3 Diffusive time constant

The diffusive time constant is a convenient way to express the time it takes a thermal wave to travel through a material. First, consider an infinitely long wall that is initially some uniform temperature, for example 300 K. Next, a heat source is placed at one side of the plate to maintain this at a constant temperature, for example 400 K. A thermal wave travels at a distance δ *i*n time *t* as shown in Figure 1.6.

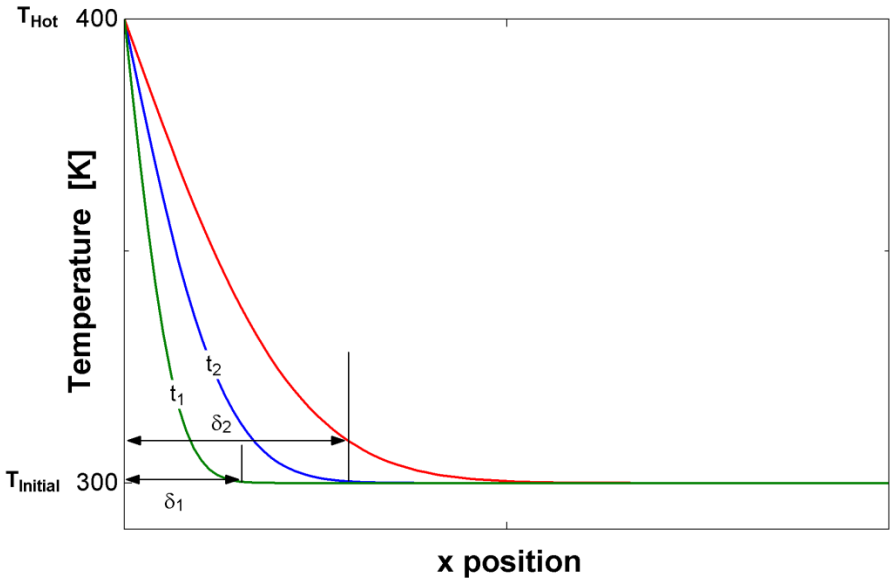

Figure 1.6: Shown is the behavior of a thermal wave traveling through an infinitely long solid that is initially at a temperature of $T_{Initial}$ = 300 K. The thermal wave is created by a heat source that remains at a constant temperature T_{Hot} = 400 K. The wave travels a distance of δ in time *t*. Deeper into the infinitely long material, the temperature will still be at $T_{Initial}$ (Nellis 2009).

The depth of the wave δ in Figure 1.6 grows in proportion to the right side of Equation 1.9.

$$\delta \approx 2\sqrt{\alpha t} \tag{1.9}$$

where α is the thermal diffusivity of the material as shown in Equation 1.8 (Nellis 2009).

Solving Equation 1.9 for time produces:

$$t = \frac{\delta^2}{4\alpha} \tag{1.10}$$

If the penetration depth of a thermal wave is assumed to be the overall length of a material, then the final relationship is:

$$t = \frac{L^2 \rho c}{4k} \tag{1.11}$$

Equation 1.11 is the thermal diffusive time constant.

1.3 Helium 4

Helium exists naturally as two isotopes; Helium 4 (He^4) and Helium 3 (He^3). 99.9999% of helium gas is He^4, and this is the isotope that will be used in the experiment. Helium can be liquefied, it has a boiling point of 4.214 K at atmospheric pressure. The density of liquid helium near its boiling point is 124.8 kg/m^3; compared to the density of water that is 996.6 kg/m^3 at 300 K, liquid helium is not very dense. He^4 can be frozen, although it must be pressurized to do so. The enthalpy of vaporization of helium is approximately 20.8 kJ/kg. This can be compared to the enthalpy of vaporization of liquid nitrogen which is approximately 199.6 kJ/kg, or 9.6 times greater than that of helium; although, nitrogen's heat of vaporization occurs at a much higher boiling point of 77.36 K. Helium is likely the most studied of cryogenic fluids because it has fascinating low temperature properties. Helium has the lowest boiling point of any element, making it a popular coolant in cryogenics for both cryostats (i.e., baths) and cryocoolers as the operating fluid. He^4 has a specific heat that actually can increase at low temperatures as shown in Figure 1.8, unlike most substances. At a condition of 5 K and atmospheric pressure, helium gas has a volumetric specific heat of 81 kJ/m^3-K, whereas copper at the same temperature has a

specific heat of only 1390 J/m^3-K. Figure 1.8 compares the specific heat of helium with several other materials at low temperatures. If helium is cooled below its boiling point, He^4 can enter a superfluid state known as Helium II; in its normal state it is known at Helium I, as shown in Figure 1.7. Superfluid Helium II can reach thermal conductivities of 85 kW/m-K, which is over 200 times the thermal conductivity of copper at room temperature. It can act as if it has zero viscosity and has many other interesting transport properties that keep helium in the forefront of cryogenic studies (Barron 1985). In this experiment, He^4 serves as the operating fluid used by the pulse tube cryocooler regenerator that is being studied, as explained in Section 1.4.

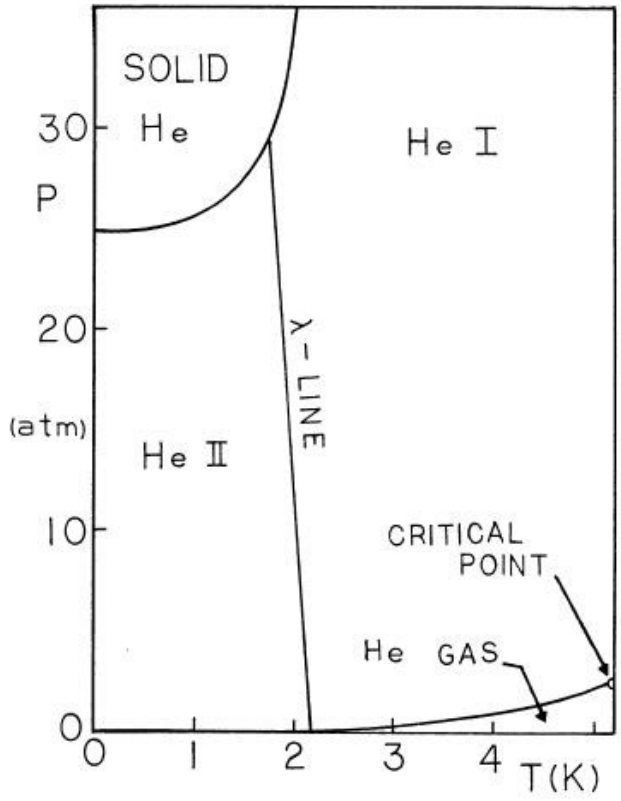

Figure 1.7: A phase diagram of liquid helium that shows pressure as a function of temperature (Frederking 2005).

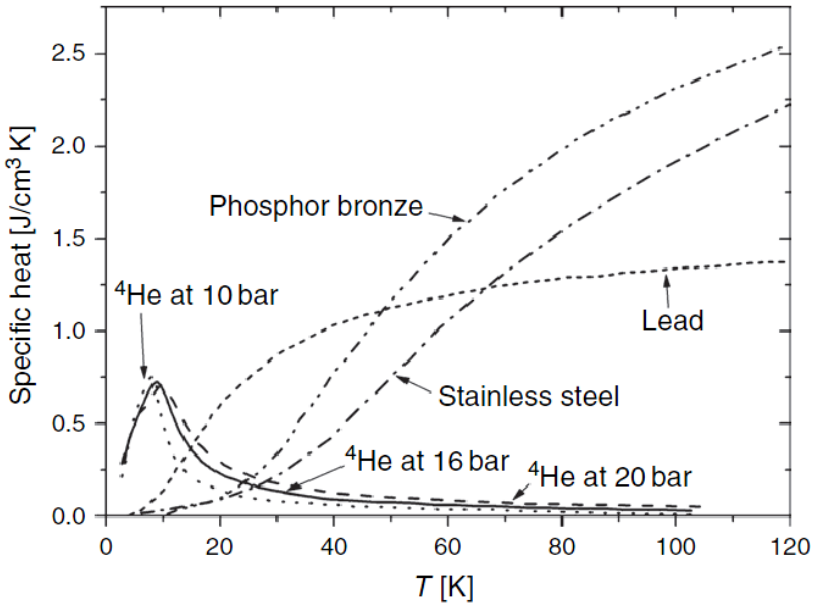

Figure 1.8: The specific heat of helium and a few other common substances as a function of temperature (Ventura 2008).

1.4 The Regenerator

The regenerator is a critical component of a pulse tube cryocooler; it is a heat exchanger that works to reclaim energy from one part of a cycle to another. The regenerator is different from a traditional heat exchanger because the same space is occupied by hot fluid and cold fluid at different times. After many cycles, an equilibrium condition is established where there is a temperature gradient along the regenerator that is maintained as fluid cyclically flows in to and out of the exchanger. Regenerators used in PTCs are typically composed of some porous rare-earth material used in screens with alternating spacers to limit conduction heat transfer along the axis. A schematic of a regenerator inside of a pulse tube cryocooler is shown in Figure 1.9.

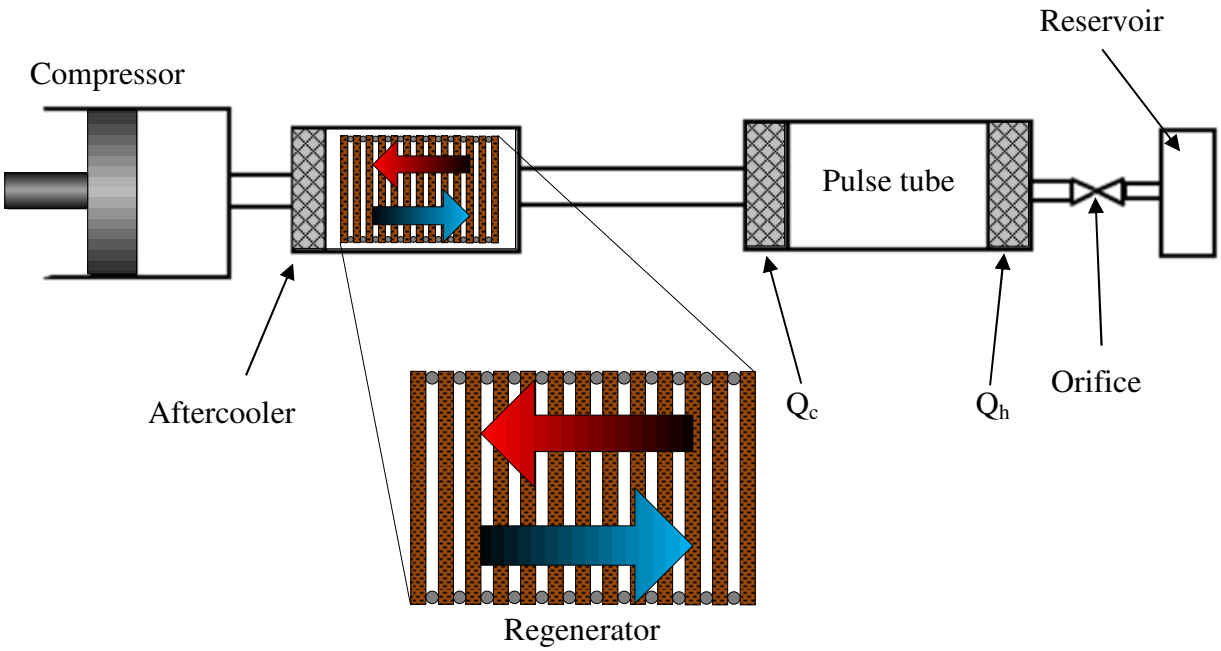

Figure 1.9: A simplified model of a pulse tube cryocooler showing the location of the regenerator. The compressor works to send oscillating pressure waves through the system. The aftercooler, Q_c, and Q_h are heat exchangers. The orifice is a flow restriction into an open reservoir. The regenerator is shown as copper porous plates with stainless steel wire spacers.

1.4.1 Common Regenerator Materials

Regenerators are made out of many different substances. Although stainless steel and copper meshes are used, substances that have high heat capacities at low temperatures are ideal because a steady temperature gradient can be established that does not change with each new cycle. Regulating the temperature of helium in PTCs is difficult because helium maintains a high specific heat, as discussed in Section 1.3. Other substances exist that have unusual behaviors that allow them to maintain high specific heats at low temperatures, as shown in Figure 1.10.

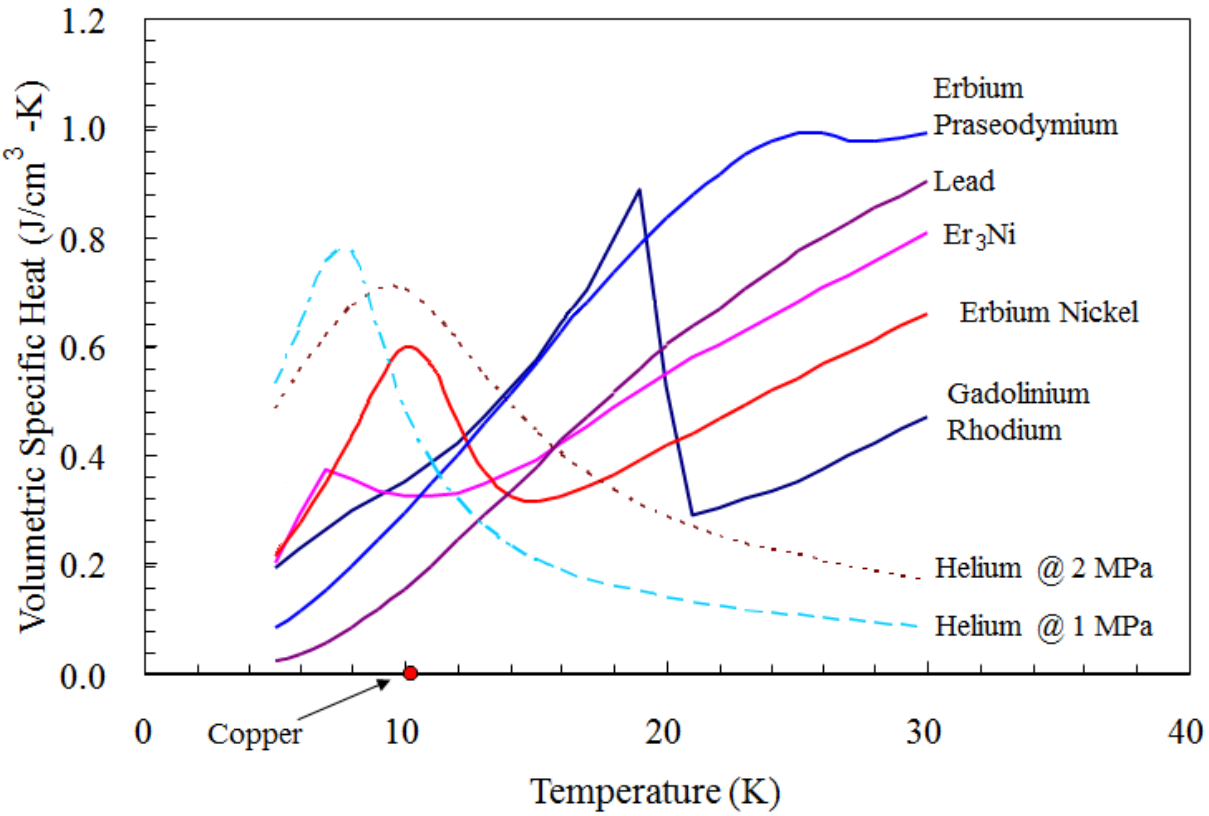

Figure 1.10: Specific heat as a function of temperature for various regenerator materials compared to helium at low temperatures. (Creare 2012).

As shown in Figure 1.10, besides lead, all other common, effective, regenerator materials are composed of rare elements. A few of the substances shown in Figure 1.10 are really only used for regenerative heat exchange at low cryogenic temperatures.

1.4.2 Adsorption, a New Regenerator

Adsorption is a surface phenomenon that refers to the binding of molecules to a surface. Energy in an amount that is similar to the surface energy for surface tension is required for molecules to be adsorbed to a surface (Brunauer 1938). Activated carbon is commonly used as an adsorbent because it has a large surface area compared to its mass. Theoretically, helium atoms could be adsorbed onto a surface as represented in Figure 1.11.

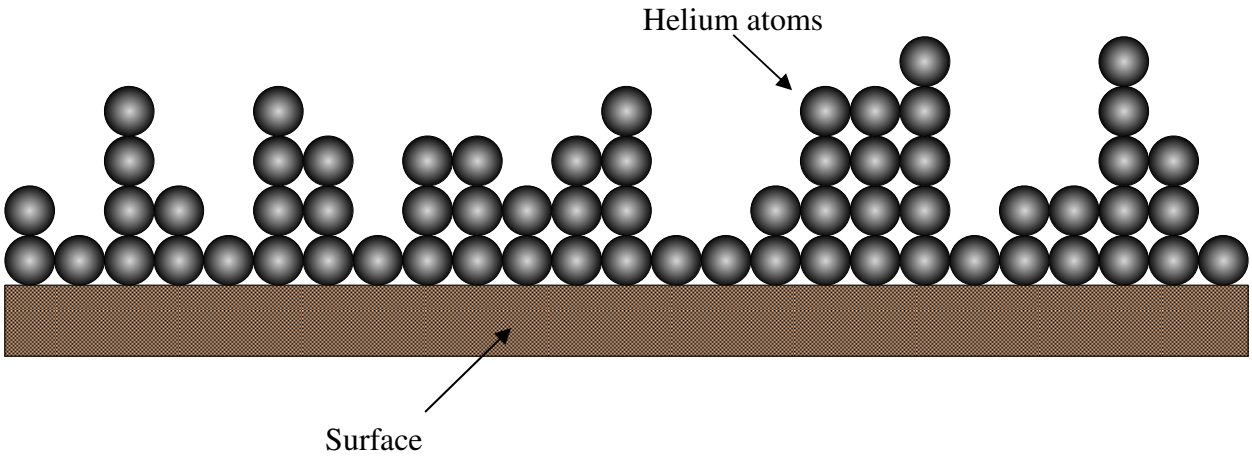

Figure 1.11: The adsorption of helium molecules onto a surface.

Creare Incorporated is developing a proprietary material using adsorption to bind helium to a surface, creating what could be a significant improvement in pulse tube cryocooler regenerators. Depending on whether the amount of adsorbed helium changes during a cycle, either the binding energy of the adsorption process or the heat capacity of the entrained helium atoms allow the material to maintain a high specific heat capacity at low temperatures. A regenerator with a high heat capacity could lead to higher cooling powers and/or high efficiency at low temperatures. Therefore, the purpose of this experiment is to develop a method that can be used to measure the heat capacity of a regenerator, to build a facility capable of the measurement, and finally to verify the facility experimentally. If a higher heat capacity in the proprietary material is measured, then a more efficient regenerator in PTCs is possible using the material. The method of measuring the heat capacity will be discussed in Section 2.

References

[1] Air Liquid 2010, *http://www.airliquideadvancedtechnologies.com/en/our-offer/space/equipments/cryo-refroidisseurs-tube-a-gaz-pulse-10-k-80-k.html.*

[2] Brunauer, S., Emmett, P. H., Teller, E., 1938, *Adsorption of Gases in Multimolecular Layers.* Journal of the American Chemical Society, 60(2) 309-319.

[3] Barron, R.F. (1985). *Cryogenic Systems.* New York, NY: Oxford University Press, Inc.

[4] Clas, S.D., Dalton, C. R., Hancock, B. C., 1999, *Differential scanning calorimetry: applications in drug development.* PSTT Vol. 2, No. 8

[5] Creare, 2012, Creare Incorporated, Contact: Chen, W.

[6] Frederking, T. H. K., Yuan. S. W. K., (2005), *Cryogenics: Low Temperature Engineering Applied Sciences.* Santa Monica, California: Yutopian Enterprises.

[7] Goodwin, R.D., 1961, Journal of Research of the National Institute of Standards and Technology, 65C:231.

[8] Janna, W. S., (2009), *Engineering Heat Transfer.* Boca Raton, FL: Taylor & Francis Group, LLC.

[9] Magee, J.W., 1991, Journal of Research of the National Institute of Standards and Technology, 96:725.

[10] Marquardt, E.D., Le, J.P., and Radebaugh, R., 2000, *Cryogenic Material Properties Database.* Boulder, CO: National Institute of Standards and Technology.

[11] Nellis, G. and Klein, S.A., (2009). *Heat Transfer.* New York, NY: Cambridge University Press.

[12] Parker, W. J., et.al., 1961, *Flash Method of Determining Thermal Diffusivity, Heat Capacity, and Thermal Conductivity*. Journal of Applied Physics, 32:9.

[13] Penco, G., et.al., 2001, *Thermal Properties Measurements Using Laser Flash Technique at Cryogenic Temperature.* Particle Accelerator Conference, Chicago.

[14] Perea Solano, B., 2004, *Cryogenic Silicon Microstrip Detector Modules for LHC*. Technical University of Catalonia.

[15] Pillai, S. O., (2005) *Solid State Physics*. Daryaganj, New Delhi, India: New Age International Ltd.

[16] Radebaugh, R, 2000, *Development of the Pulse Tube Refrigerator as an Efficient and Reliable Cryocooler*. National Institute of Standards and Technology, Institute of Refrigeration.

[17] Ventura, G., and Risegari, L., (2008) *The Art of Cryogenics: Low-Temperature Experimental Techniques*. Daryaganj, Burlington, MA: Elsevier Ltd.

2 Modeling

2.1 The Need for an In-Depth Analysis

The operating conditions associated with this experiment are atypical of most cryogenic property measurements. Normally, to measure the specific heat of any substance a controlled and measurable amount of thermal energy is added to a substance and the resulting temperature change is measured in a calorimeter. This type of experiment would be performed in a near-vacuum to ensure that the energy totally transfers to the substance in question. However, for the UW experiment the adsorbed-helium plates must be contained in a high pressure helium environment in order to work correctly; therefore the use of a vacuum to measure the specific heat is impossible. Additionally, it is desirable to carry out the tests at the expected operating temperature and pressure of the helium within a pulse tube cryocooler in order to capture the correct behavior of the plates during the test. The predicted conditions of the regenerator under operating conditions are a warm temperature of 20 K, a cold temperature of 4 K, and a helium pressure of 1 MPa; note that helium 4 is supercritical at these conditions. The regenerator and its microchannels will be immersed in the pressurized helium. A model was necessary to establish a test method that would ensure that heat capacity could be measured within the required accuracy under these conditions.

2.2 Thermal Diffusive Time Constant

The model that will be described in this section is based on the thermal diffusive time constant of the regenerator material at derived in Section 1.2.3. The general equation for this time constant is shown below:

$$\tau = \frac{\delta^2 \rho c}{k} \tag{2.1}$$

where τ is the time constant, δ is the length of the material in the heat flow direction, ρ is density, c is specific heat, and k is the thermal conductivity. The approximate amount of time it takes a thermal wave to travel through the material is the time τ. In other words, if a heat source is applied to one side of a piece of material of length δ with the other respective properties shown above, the time it will take the opposite side's temperature to rise is the time on the left hand side of Equation 2.1. Note that the time constant does not show the magnitude of temperature rise or heat transfer rate. The regenerator material is a composite of different materials and therefore the properties in Equation 2.1 must be volume-weighted averages.

2.3 Composite One-Dimensional Geometry

The first part of the one-dimensional model was the determination of the effective properties for the regenerator material. The actual geometry of each disk is shown in Figure 2.1. In addition to determining the regenerator's effective properties, it is known that only five disks will be provided for the final experiment; this is significant because with only five disks, initial models showed a time response too small to conveniently measure. For reference, a fully operational new type of regenerator is projected to operate with 140 plates. Therefore, to accommodate such a short test regenerator length, nylon spacers were added into the model to add thermal resistance without adding much capacitance; these spacers will lengthen the thermal diffusive time constant. Adding these nylon spacers necessarily complicates the model, as will be shown. The geometry of a single plate is a disk made of silicon with a hollowed center portion filled with the proprietary adsorbent material. The outer silicon ring is composed of finely

machined involute microchannels to promote heat transfer between the helium in the pulse tube and the regenerator adsorbent core.

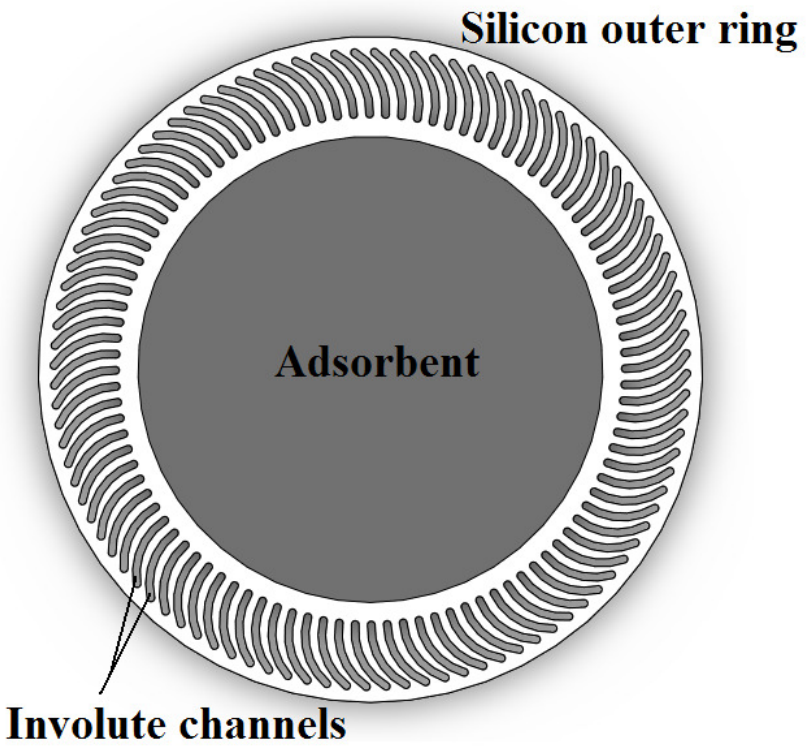

Figure 2.1: A detailed drawing of the silicon disks that will be used in the test**.**

The width of each channel in Figure 2.1 is exaggerated; in the actual disks the channels will be narrower and more numerous. The adsorbent is shown by the shaded dark center area. The silicon ring is the lighter colored outside material. The silicon is 250 μm thick, and the adsorbent is 150 μm thick; this discrepancy is mitigated by an extra 100 μm of silicon underneath the adsorbent. Therefore, the silicon forms a cup that holds the center adsorbent material as shown in Figure 2.2.

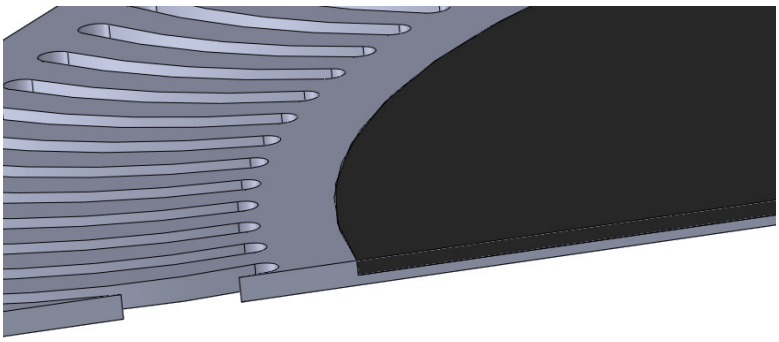

Figure 2.2: A diametric sectional view of the silicon plates being used. The dark area is the adsorbent center; the lighter area is the silicon.

The one dimensional model can be thought of as three separate pieces, as shown in Figure 2.3. The first part is the silicon outer ring with the center composed of the proprietary matrix. The next layer is only silicon. The last portion is the nylon spacer.

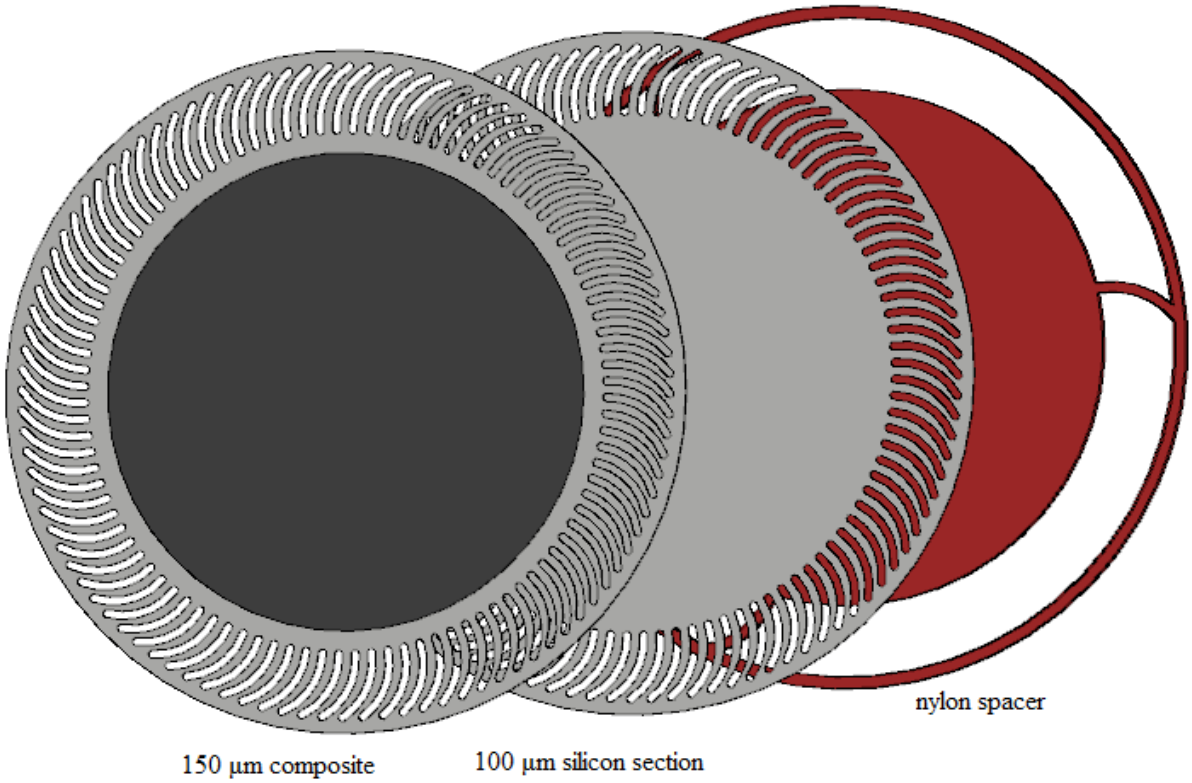

Figure 2.3: A cutaway view of the composite structure of the silicon disk and nylon spacer.

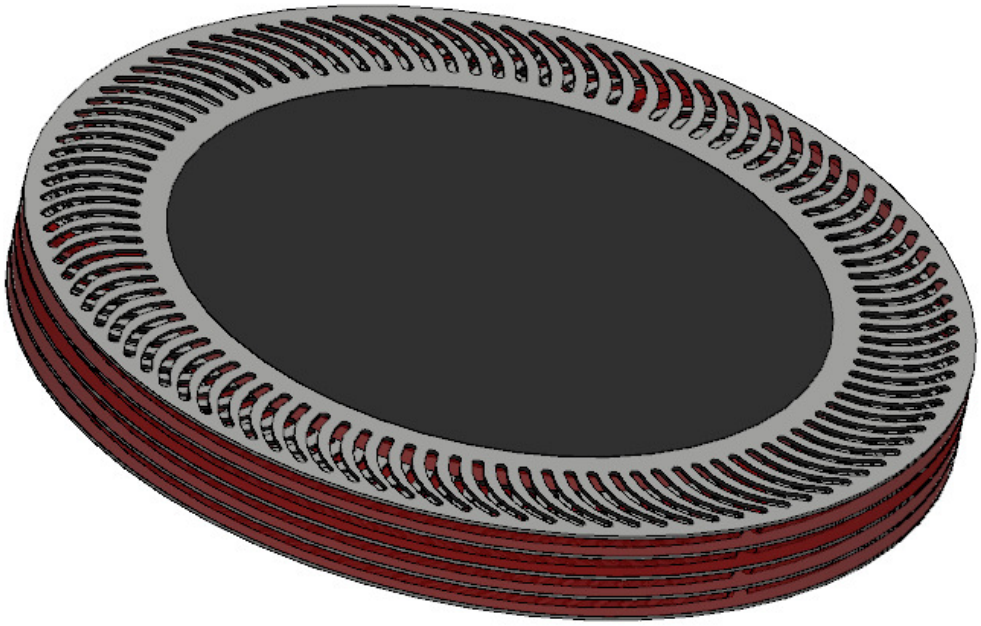

Figure 2.4: A final view of what the entire test stack will look like with five proprietary material plates and four spacers.

2.3 Effective regenerator properties

Property data for substances were obtained from a few sources. The conductivities and specific heats of nylon were determined from the National Institute of Standards and Technology's (NIST's) online cryogenic material database using polynomials (Marquardt 2012). The adsorbent's estimated properties were obtained from Weibo Chen at Creare Incorporated. Engineering Equation Solver (Klein 2012) was used to obtain the helium properties and parameterize the polynomials from NIST. The thermal conductivity of silicon was found in the Journal of Applied Physics (Slack 1964). An article from Solid State Communications was used to find the specific heat of silicon (Mertig 1984). Table 2.1 shows the main material properties.

Table 2.1

Material	Specific Heat (J/kg-K)	Conductivity (W/m-K)
Silicon	0.016	100
Adsorbent	143.9	1
Nylon PA66	1.56	0.01245
Helium	2872	0.0227

As shown in Table 2.1, the conductivity of the silicon is 100 times larger than that of the adsorbent at these temperatures, which would make distinguishing the conductivity of the adsorbent relative to any other material difficult. Also, the specific heat of the adsorbent is high relative to silicon and nylon, but it is actually less than helium at these temperatures. The ideal experiment will differentiate between which heat capacity is actually being measured.

The determination of effective regenerator properties begins by first modeling a single composite of silicon and adsorbent. EES was used for most of these calculations. Since conductivity is per unit length and cross sectional area in the first composite section in Figure 2.3 is constant, an area-weighted estimation of the conductivity that takes into account the thermal conductivity of the silicon, the helium contained in the microchannels, and the adsorbent is calculated:

$$k_p = \frac{A_o k_{si} + A_{chan} k_{he} + A_{ads} k_{ads}}{A_{total}} \tag{2.2}$$

Property values are shown in Table 2.2. The result of Equation 2.2 is that the combined conductivity of the silicon plate is estimated to be k_p = 38.7 W/m-K.

Table 2.2

Symbol	Definition	Value
k_p	Overall average conductivity of a composite plate	38.7 W/m-K
k_{he}	Conductivity of the helium	0.0227 W/m-K
k_{ads}	Conductivity of the adsorbent	1 W/m-K
k_{si}	Conductivity of the silicon	100 W/m-K
A_{chan}	Cross sectional area (void space) of the involute channels	0.0009 m^2
A_{ads}	Cross sectional area of the adsorbent center	0.000346 m^2
A_o	Cross sectional area of the outer ring of just silicon	0.00027 m^2
A_{total}	Total cross sectional area of the channels, silicon, and adsorbent	0.0007 m^2

Next, the conductivity of the 100 µm silicon section $k_{si,pl}$ is modeled:

$$k_{si,pl} = \frac{(A_{total} - A_{chan})\ k_{si} + A_{chan}\ k_{he}}{A_{total}} \tag{2.3}$$

the result is that $k_{si,pl}$ = 87.3 W/m-K.

To add thermal resistance without adding significant thermal capacitance, a nylon polymer was inserted between the silicon plates. Nylon polyamide PA66 was selected in this application because of its well-documented cryogenic behavior from the NIST database. To model the effective conductivity of the plate and spacer materials in series, the equations below were used. These equations were taken from Heat Transfer (Nellis 2009), which computes the effective conductivity of a non-homogeneous material. To begin, Equation 2.4 shows that the heat flux through the center of disks is equal to the temperature difference from one end of the stack to the other, ΔT, divided by a thermal resistance R.

$$\dot{q} = \frac{\Delta T}{R} \tag{2.4}$$

Equation 2.5 is the resistance due to conduction through the stack of disks, where L is the total length of the disks, k_{eff} is the effective homogeneous conductivity, and A_{total} is the total cross sectional area of the cylinder.

$$R = \frac{L}{k_{eff}\, A_{total}} \tag{2.5}$$

The result of the combination of Eq. 2.4 and Eq. 2.5 is shown in Eq. 2.6.

$$\dot{q} = \frac{k_{eff}\, A_{total}\, \Delta T}{L} \tag{2.6}$$

Next, the total resistance through a variable number of plates is calculated using a series resistance network as shown in Eq. 2.7. Most of the variables for Eq. 2.7 are designated in Table 2.2. The thickness of the nylon spacer used, although variable, is th_{nyl} = 80 µm, the thickness of the composite plate is th_p = 150 µm, and the thickness of the silicon section is th_{sil} = 100 µm. N is the number of silicon plates, which is one more than the number of nylon plates. In this calculation N = 5 silicon plates. The conductivity of the nylon is k_{nyl} = 0.0125 W/m-K. The combined resistance will be denoted R' and is shown below:

$$R' = \frac{N\, th_p}{k_p\, A_{total}} + \frac{N\, th_{sil}}{k_{si}\, A_{total}} + \frac{(N-1)\, th_{nyl}}{k_{nylon}\, A_{total}} \tag{2.7}$$

The result is that R' = 45.5 K/W. Equation 2.8 shows that the heat transfer rate through the disks is also equal to the temperature difference from one side of the plates to the other divided by this new resistance R':

$$\dot{q} = \frac{\Delta T}{R'} \tag{2.8}$$

Combining Eq. 2.7 and Eq. 2.8 arrives at this result:

$$\dot{q} = \frac{\Delta T}{\frac{N\,th_p}{k_p\,A_{total}} + \frac{N\,th_{sil}}{k_{si}\,A_{total}} + \frac{(N-1)\,th_{nyl}}{k_{nylon}\,A_{total}}} \tag{2.9}$$

Since Eq. 2.6 and Eq. 2.9 are both referring to the same heat transfer rate, they can be combined into a new equation:

$$k_{eff} = \frac{L}{\frac{N\,th_p}{k_p} + \frac{N\,th_{sil}}{k_{si}} + \frac{(N-1)\,th_{nyl}}{k_{nylon}}} \tag{2.10}$$

Equation 2.8 calculates the effective conductivity of the composite stack. Using the provided numbers, it results in an effective conductivity of a regenerator test stack of k_{eff} = 0.051 W/m-K.

Densities of the solids were referenced at low temperatures, although these values at 4 K were difficult to find. The density of helium at 4 K and 1 MPa was available using EES. The total effective volume-weighted average density of the plates and nylon spacers is determined using this equation:

$$\rho_{eff} = \frac{(N-1)V_{spacer}\,\rho_{nyl} + N\left(V_o\,\rho_{si} + V_{ads}\,\rho_{ads} + V_{chans}\,\rho_{he} + V_{sil,sp}\,\rho_{si}\right)}{(N-1)V_{spacer} + N\,V_{total}} \tag{2.11}$$

The total effective density of the material using Equation 2.11 is approximately ρ_{eff} = 1823 kg/m^3.

Table 2.3

Symbol	Definition	Value
ρ_{eff}	Total effective density of plates and spacer	1823 kg/m^3
ρ_{nyl}	Density of nylon	1100 kg/m^3
ρ_{si}	Density of silicon	2330 kg/m^3
ρ_{ads}	Density of adsorbent	2330 kg/m^3
ρ_{he}	Density of helium	152.4 kg/m^3
V_{spacer}	Volume of nylon spacer	7.07E-08 m^3
V_o	Volume of outer silicon	4.06E-08 m^3
V_{ads}	Volume of inner adsorbent	5.20E-08 m^3
V_{chan}	Volume of the involute channels	2.25E-08 m^3
V_{total}	Volume of adsorbent, silicon, and channels	1.77E-07 m^3
$V_{sil,sp}$	Volume of just the silicon in the 100 μm silicon section	6.17E-08 m^3
N	Number of plates	5

A mass-weighted average was used to determine the effective specific heat of the composite layers. Equation 2.12 below shows that with the specific heat of the silicon as c_{si}, the adsorbent as c_{ads}, the helium in the channels as c_{he}, and the nylon spacers as c_{nyl}, the total heat capacity C can be determined. The values used for specific heats are from Table 2.1:

$$C = N(V_o \rho_{si} c_{si} + V_{ads} \rho_{ads} c_{ads} + V_{chans} \rho_{he} c_{he} + V_{sil,p} \rho_{si} c_{sil}) + (N-1) V_{spacer} \rho_{nyl} c_{nyl} \qquad (2.12)$$

Equation 2.12 results in an effective heat capacity of C = 0.137 J/K. The total volume of the stack of plates can be represented by:

$$V_{stack} = N(V_{total}) + (N-1) V_{spacer} \qquad (2.13)$$

where V_{stack} is the total volume of the stack. Using previously stated values, V_{stack} = 11.7E-07 m^3. If one considers a homogeneous material, the total heat capacity can be written in terms of V_{stack}, the previously calculated effective density ρ_{eff}, and an effective specific heat called c_{eff}:

$$C = V_{stack} \rho_{eff} c_{eff} \qquad (2.14)$$

Since Eq. 2.14 refers to the same heat capacity as Eq. 2.12, these can be combined to form a new equation that calculates the effective specific heat c_{eff}:

$$c_{eff} = \frac{N(V_o \rho_{si} c_{si} + V_{ads} \rho_{ads} c_{ads} + V_{chans} \rho_{he} c_{he} + V_{sil,p} \rho_{si} c_{sil}) + (N-1) V_{spacer} \rho_{nyl} c_{nyl}}{V_{stack} \rho_{eff}} \quad (2.15)$$

Using previously stated values, the overall effective specific heat is c_{eff} = 64.4 J/kg-K. The total thermal resistances of the nylon and silicon plates were calculated separately, though they were not to be used in the final derivation of the thermal diffusivity; they are used to form dimensionless ratios that govern the model. The nylon resistance is shown below:

$$R_{nylon} = \frac{(N-1)\, th_{nyl}}{k_{nyl}\ A_{nylon}} \quad (2.16)$$

This resistance is R_{nylon} = 45.49 K/W. The total resistance of the composite silicon/adsorbent plate is:

$$R_{pl} = \frac{N\ th_p}{k_p\ A_{total}} \quad (2.17)$$

This resistance is R_{pl} = 0.0274 K/W.

The total resistance of the plain silicon section is calculated:

$$R_{si,pl} = \frac{N\ th_{sil}}{k_{si}\ A_{total}} \quad (2.18)$$

This resistance is $R_{si,pl}$ = 0.007 K/W. As can be observed and as desired, the resistance of the nylon is much greater than any other resistance in the stack of disks. The thermal capacitance of the nylon, composite silicon plate, and plain silicon plate were calculated but were not to be used in the final thermal diffusive equation; they were used to establish dimensionless ratios. The capacitance of the nylon is shown:

$$Cap_{nylon} = (N-1)\, V_{spacer}\, \rho_{nylon}\, c_{nylon} \tag{2.19}$$

This capacitance is Cap_{nylon} = 0.00049 J/K. The capacitance of the composite silicon is shown:

$$Cap_p = N\,(V_o\, \rho_{si}\, c_{sil} + V_{chans,p}\, \rho_{he}\, c_{he} + V_{ads}\, \rho_{si}\, c_{ads}) \tag{2.20}$$

The capacitance of the silicon plate is Cap_p = 0.12 J/K. The capacitance of the plain silicon section is shown by the equation below, where the volume of the involute channels in this section is represented by the variable $V_{chans,sil}$ = 9.01E-09 m^3.

$$Cap_{si,pl} = N\,(V_{chans,sil}\, \rho_{he}\, c_{he} + V_{sil,sp}\, \rho_{si}\, c_{sil}) \tag{2.21}$$

This capacitance of the plain silicon plate is $Cap_{si,pl}$ = 0.02 J/K. As can be observed and as desired, the capacitance of the nylon is significantly lower than the capacitance of the composite and plain silicon sections.

An equation that can relate the effective material properties is the thermal diffusive time constant derived in Equations 1.9-1.11. After substituting in the effective properties determined previously, the useable form of the equation is:

$$t = \frac{L^2 \rho_{eff}\, c_{eff}}{4 k_{eff}} \tag{2.22}$$

Equation 2.22 can be used in many different ways. For example, controlling the nylon thickness can alter the magnitude of the time. If two materials have extremely fast time responses, nylon resistance can be added to lengthen the time response to a point where a comparison is easier. This is shown in Figure 2.5.

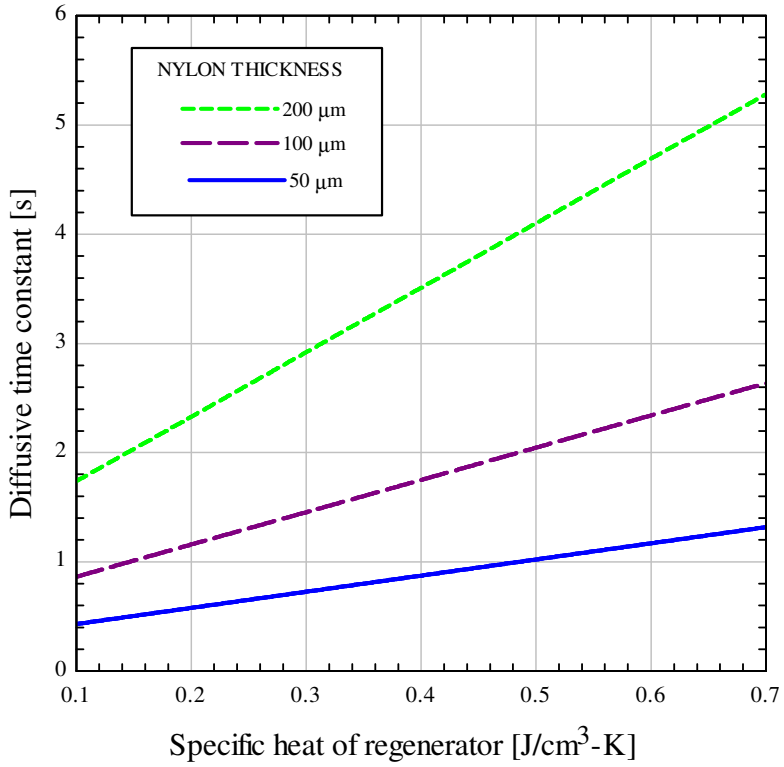

Figure 2.5: Shown is the diffusive time constant as a function of the effective specific heat of the regenerator for various nylon spacer thicknesses. The time constant is the time it takes a thermal wave to travel through a 5-plate stack of the novel regenerator disks with nylon spacers added. As can be seen, the magnitude of time can be easily controlled by varying the thickness of nylon spacers. Altering the magnitude of time will allow easier comparison between center materials.

2.4 Practical Uses of the 1-D Model

A test that propagates thermal waves through two different materials can reveal which has the higher heat capacity, making it the better regenerator. The time response of each material is a function of the variables in Eq. 2.22. A preliminary uncertainty propagation of this response time as a function of the conductivity, heat capacity, and density of just the inner puck adsorbent material reveals that if each of these is allowed to vary 10%, the heat capacity is responsible for nearly 100% of the resulting time response uncertainty. This is important because the center portion of the regenerator plates can be replaced by different materials that may not have similar densities or conductivities as the proprietary disks, but their heat capacity can still be compared

to the new disks. To illustrate this further, take the ratio of the thermal response times of two regenerator stacks with nylon spacers:

$$\frac{t_{regen}}{t_{control}} = \frac{\frac{\delta^2 \rho_{eff} c_{regen}}{4 k_{eff}}}{\frac{\delta^2 \rho_{eff} c_{control}}{4 k_{eff}}} \tag{2.23}$$

where t_{regen} is the time response of the novel regenerator and $t_{control}$ is the is the time response of a stack with the proprietary center matrix replaced by some other material (e.g., pure silicon). The overall length δ is the same in both cases, thus it cancels out. As described previously, the density and conductivity of the center material barely affect the time response. Therefore, all other things besides the center puck being equal, the density and conductivity of both materials would still be very similar and can cancel out, leaving this approximate ratio:

$$\frac{t_{regen}}{t_{control}} = \frac{c_{regen}}{c_{control}} \tag{2.24}$$

Equation 2.24 directly compares the ratio of specific heats of the proprietary regenerator to either a control or any other similar regenerator. With plain silicon used as the control specimen and the regenerator model constructed previously, the ratio of response times $t_{regen}/t_{control}$ in Eq. 2.24 is 1.9, which is also the estimated ratio of specific heats.

Equation 2.22 is also useful for analyzing a single regenerator. With the thickness of nylon spacers as th_{nylon} = 0.0001 m, the total number of silicon plates as 5, and the total length of the stack of plates totaling δ = 1.47 mm, the time response of a thermal wave is t = 1.895 s. Note that this is the expected time response of the actual test specimen as shown in Figure 2.6. If the heat capacity of the adsorbent center portion changes by a large magnitude, for example it doubles, this time response changes to t = 2.78 s. The change in response time here between the two heat capacities is 0.89 s or approximately 47% of the original time. Figure 2.6 shows this

relationship over a range of reasonable specific heats:

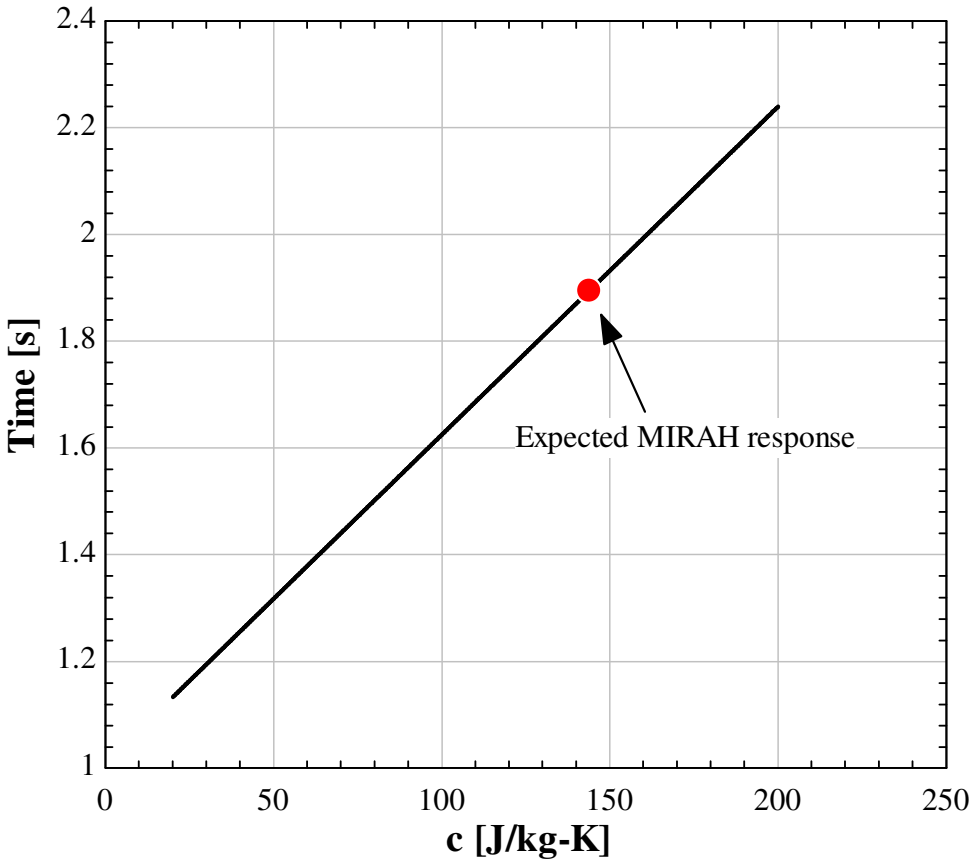

Figure 2.6: Shown is the thermal response time as a function of specific heat of the center puck. Note that this time response is linearly related to the specific heat.

As described in Figure 2.6, the nylon thickness can be changed to alter the magnitude of the time responses. For instance, with the thickness of nylon spacers as th_{nylon} = 0.0001 m, the total number of silicon plates as 5, and the total length of the stack of plates totaling δ = 1.47 mm, the time response of a thermal wave is t = 1.895 s**.** Doubling the thickness of the nylon to 0.0002 m, the time response of the thermal wave increases to 5.72 s. This is a 2.94 s time difference or approximately 106% of the original time.

An uncertainty analysis was performed on Equation 2.22 in order to investigate the impact of a variety of parameters. The uncertainty of all variables in Table 2.4 except the specific

heat of the proprietary adsorbent was assumed to be known within 5 % accuracy. The specific heat of the adsorbent was assumed to be known within 10 % accuracy. Shown in Table 2.4 is the result of this uncertainty analysis. Note that the response time t is very sensitive to both the specific heat of the adsorbent and the conductivity of the nylon spacers. Thus, it is imperative that the conductivity of the nylon spacers used in lengthening the regenerator test specimen is accurately known.

Table 2.4

Variable ± Uncertainty	**Partial derivative**	**Value**	**% of uncertainty**
t = 1.895 ± 0.137 s			
c_{ads} = 143.9 ± 14.39 J/kg-K	$\partial t / \partial c_{ads}$	0.00615	32.91 %
c_{nyl} = 1.56 ± 0.078 J/kg-K	$\partial t / \partial c_{nyl}$	0.003158	0.00 %
c_{sil} = 0.016 ± 0.0008 J/kg-K	$\partial t / \partial c_{sil}$	0.005334	0.00 %
c_{he} = 2882 ± 144 J/kg-K	$\partial t / \partial c_{he}$	0.0003487	10.60 %
k_{ads} = 1 ± 0.05 W/m-K	$\partial t / \partial k_{ads}$	-0.0000443	0.00 %
k_{nyl} = 0.0125 ± 0.0006 W/m-K	$\partial t / \partial k_{nyl}$	-152.1	37.66 %
k_{sil} = 100 ± 5 W/m-K	$\partial t / \partial k_{sil}$	-0.000023	0.00 %
k_{he} = 0.0227 ± 0.0011 W/m-K	$\partial t / \partial k_{he}$	-0.000023	0.00 %
ρ_{ads} = 2332 ± 117 kg/m^3	$\partial t / \partial \rho_{ads}$	0.0003796	8.23 %
ρ_{nyl} = 1100 ± 55 kg/m^3	$\partial t / \partial \rho_{nyl}$	4.48E-6	0.00 %
ρ_{sil} = 2332 ± 117 kg/m^3	$\partial t / \partial \rho_{sil}$	3.66E-8	0.00 %
ρ_{he} = 152.4 ± 7.62 kg/m^3	$\partial t / \partial \rho_{he}$	0.006593	10.60 %

The specific heat of the regenerator can be determined if one knows or can predict the effective density and conductivity from Equation 2.22; this is assuming a test has been performed and the time response is known. Equation 2.25 shows this relationship:

$$c_{calc} = \frac{4 k_{eff} t_{meas}}{\delta^2 \rho_{eff}} \tag{2.25}$$

An uncertainty analysis on the estimated specific heat of a complete novel regenerator was performed. The analysis assumed that time was measured within 5 % accuracy and the overall specific heat of the regenerator c_{calc} was solved for. Note that the other perimeters were assumed to be known within 10 % accuracy.

Table 2.5

Variable ± Uncertainty	**Partial derivative**	**Value**	**% of uncertainty**
c_{calc} = 126.4 ±16.81 J/kg-K			
k_{ads} = 1 ± 0.05 W/m-K	$\partial c_{calc} / \partial k_{ads}$	0.00295	0.00 %
k_{he} = 0.0227 ± 0.00227 W/m-K	$\partial c_{calc} / \partial k_{he}$	0.001536	0.00 %
k_{nyl} = 0.0125 ± 0.00125 W/m-K	$\partial c_{calc} / \partial k_{nyl}$	10142	56.41 %
k_{sil} = 100 ± 10 W/m-K	$\partial c_{calc} / \partial k_{sil}$	0.00154	0.00 %
ρ_{ads} = 2332 ± 233 kg/m^3	$\partial c_{calc} / \partial \rho_{ads}$	-0.00445	0.38 %
ρ_{he} = 152.4 ± 15.2 kg/m^3	$\partial c_{calc} / \partial \rho_{he}$	-0.0193	0.03 %
ρ_{nyl} = 1100 ± 110 kg/m^3	$\partial c_{calc} / \partial \rho_{nyl}$	0.0242	2.51 %
ρ_{sil} = 2332 ± 233 kg/m^3	$\partial c_{calc} / \partial \rho_{sil}$	-0.0371	26.5 %
t_{meas} = 1.895 ± 0.0948 s	$\partial c_{calc} / \partial t_{meas}$	66.71	14.14 %

Note that the three largest sources of uncertainty in the calculation of specific heat are the conductivity of the nylon spacers, the density of the silicon, and the measurement of time for the temperature to rise on the opposite side of the regenerator stack. The overall estimated specific heat for a proprietary regenerator composite is c_{calc} = 126.4 ± 16.81 J/kg-K. Even though this specific heat includes the specific heat of the nylon spacers, Table 2.4 showed that this specific heat is negligible at 4 Kelvin. Thus, c_{calc} is the actual estimated specific heat of the novel material regenerator as long as the conductivity of nylon, the density of silicon, and the time response are known accurately.

References

[1] *Cryogenic Reference Tables.* 2004, Lake Shore Cryogenics, Inc.

[2] *Heat Capacity of Amorphous Polymers at Low Temperatures.*1962, Nature Publishing Group, 1280-1281(193).

[3] Klein, S.A. (2012). Engineering Equation Solver [Computer Software]. Madison, WI: F-Chart Software.

[4] Mertig, M., Pompe, G., Hegenbarth, E., *Specific Heat of Amorphous Silicon at Low Temperatures.* 1984, Great Britain: Solid State Communications, 369-372(49).

[5] Nellis, G. and Klein, S.A., (2009). *Heat Transfer.* New York, NY: Cambridge University Press.

[6] Marquardt, E.D., Le, J.P., and Radebaugh, Ray, *Cryogenic Material Properties Database.* 2000, Boulder, CO: National Institute of Standards and Technology.

[7] Perea Solano, Blanca, *Cryogenic Silicon Microstrip Detector Modules for LHC*. 2004, Technical University of Catalonia.

[8] Slack, G. A., *Thermal Conductivity of Pure and Impure Silicon, Silicon Carbide, and Diamond.* 1964, Schenectady, New York: General Electric Research Laboratory.

3 Construction of the Facility

3.1 Cryostat

A test facility had to be constructed that could simulate the conditions found inside of a pulse tube cryocooler regenerator during operation; specifically, temperatures near 4 K and pressures of 1 MPa in a pure helium environment. These conditions are necessary to ensure that the adsorptive proprietary center material behaves as intended. To obtain these test conditions, a cryostat was designed within a liquid nitrogen jacketed Dewar manufactured by Cryofab, Inc. for superconducting magnets. The Dewar has an insulating vacuum space between the inner wall and the liquid nitrogen jacket. The liquid nitrogen chamber is insulated from the ambient using a solid material such as multilayer insulation in an outer vacuum space. The Dewar is designed to hold a bath of liquid helium with minimum heat leak.

Figure 3.1: Shown is the Cryofab, Inc. superconducting magnet Dewar that will serve as the insulating chamber for the experiment.

A top plate will be installed on the Dewar to create an enclosed chamber and an inner vessel hanging near the bottom will be thermally isolated from the top plate by a long, slender

neck. The inner vessel will be pressurized to the operating condition of 1 MPa and immersed in liquid helium within the Dewar that exists at approximately atmospheric pressure.

3.2 Top Plate

A top plate was designed to seal off the cryostat of liquid helium from the environment. It had to fulfill several requirements. First, the top plate had to be hermetic because as the inner chamber of the experiment cools down, cryopumping can occur. Cryopumping occurs when air from the ambient is pulled into the experiment; any entrance for this air would be frozen shut with water vapor. If this is not accounted for, a large and dangerous pressure increase can occur during warm-up (Elkin 2006). Next, as liquid helium boils off positive pressure typically occurs inside the Dewar. The top plate must be able to vent this pressure. Additionally, a vacuum may be pulled on the inner chamber during operation or at some future time, therefore the top plate was designed to withstand this absence of pressure. Electronics and pressure line feed-throughs had to be incorporated as well. The design of the top plate is shown in Figure 3.2.

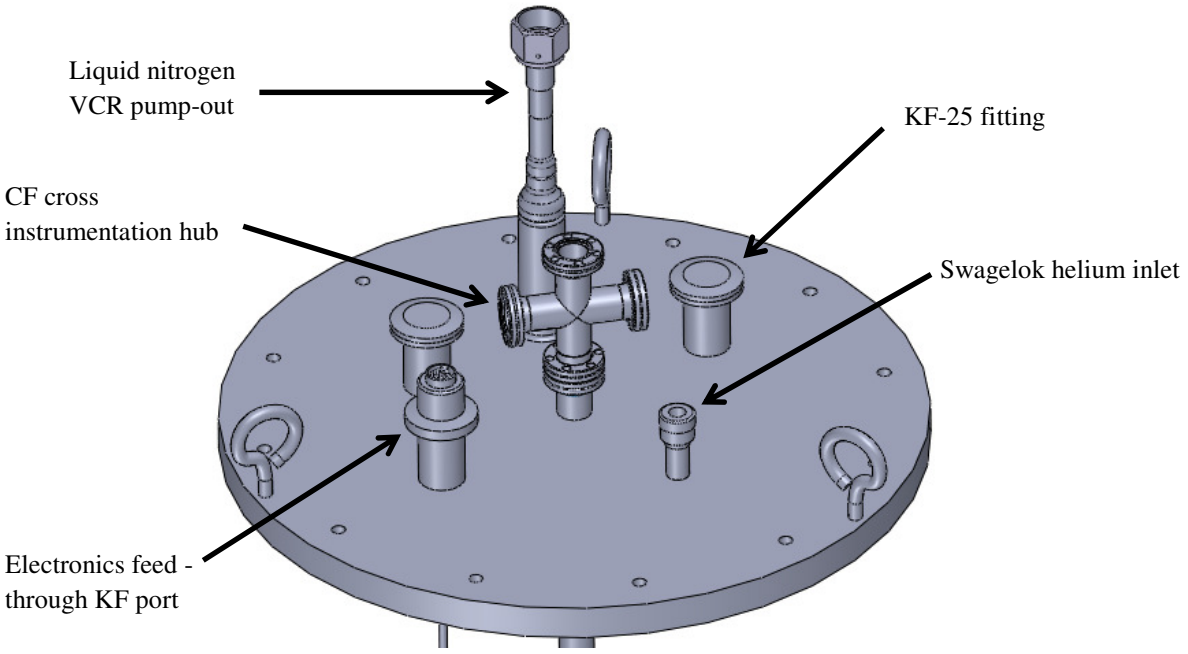

Figure 3.2: A detailed view of the top plate showing some of its initial features.

The top plate has the following features:

- Assembled from 304L stainless steel with gas tungsten arc welds located on the inner side in case a vacuum is used
- Three KF-25 flanges installed for electronics, vacuum equipment, hoses, leveling indicators, and other devices
- A Swagelok Ultra-Torr bored-through 3/8” liquid helium insertion port that is used to accommodate a helium transfer line
- A Conflat cross flange that serves as the instrumentation hub for the inner pressure vessel
- A 1/2” VCR feed-through that serves as a pump-out for liquid nitrogen used in precooling the system; this is explained in Section 3.3

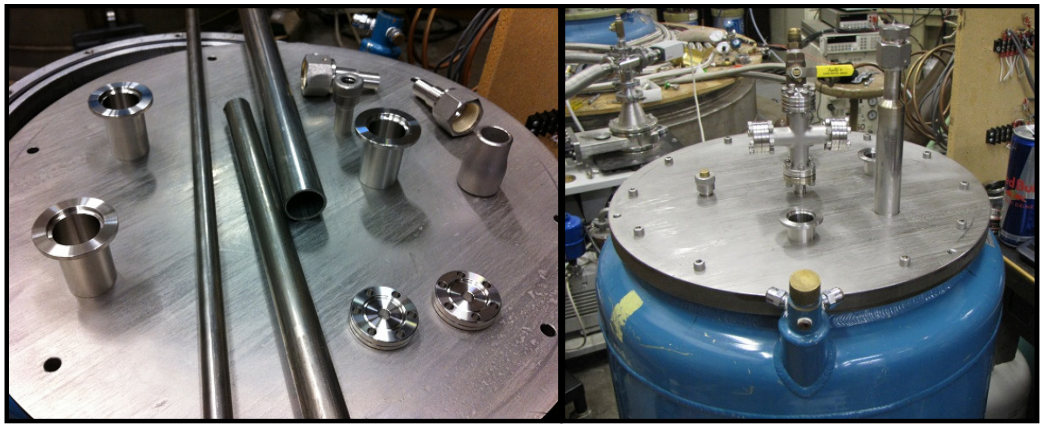

Figure 3.3: Shown is the initial stainless steel 304L plate before any machining on the left. The final plate with welded fittings is shown on the right.

Figure 3.4: A bottom view of the top plate. The machined surface is where the steel plate meets a Viton rubber gasket of the Dewar.

3.3 Thermal Standoff

As mentioned in Section 3.2, a thermal standoff was built into the top plate to pump out the liquid nitrogen. A thermal standoff minimizes frost on the top plate when pumping out liquid nitrogen used in precooling components inside the Dewar. If the top plate becomes too cold, the seals on the top plate could be compromised. The standoff is essentially a fin that makes the conduction resistance to heat transfer along the standoff high, yet the convection resistance between the standoff and the ambient low. This means that there will be a large temperature difference between the cold tip of the standoff and the base, preventing the top plate from developing a significant amount of frost. A standoff is typically designed using a thin-walled material; in this case, stainless steel 304L. If the standoff were a more important piece of the experiment, the resistance due to the frost layer on the fin during operation would have been added to the model. In the model shown in Figure 3.5, only free convection from the steel and conduction along the axis of the steel cylinder were considered.

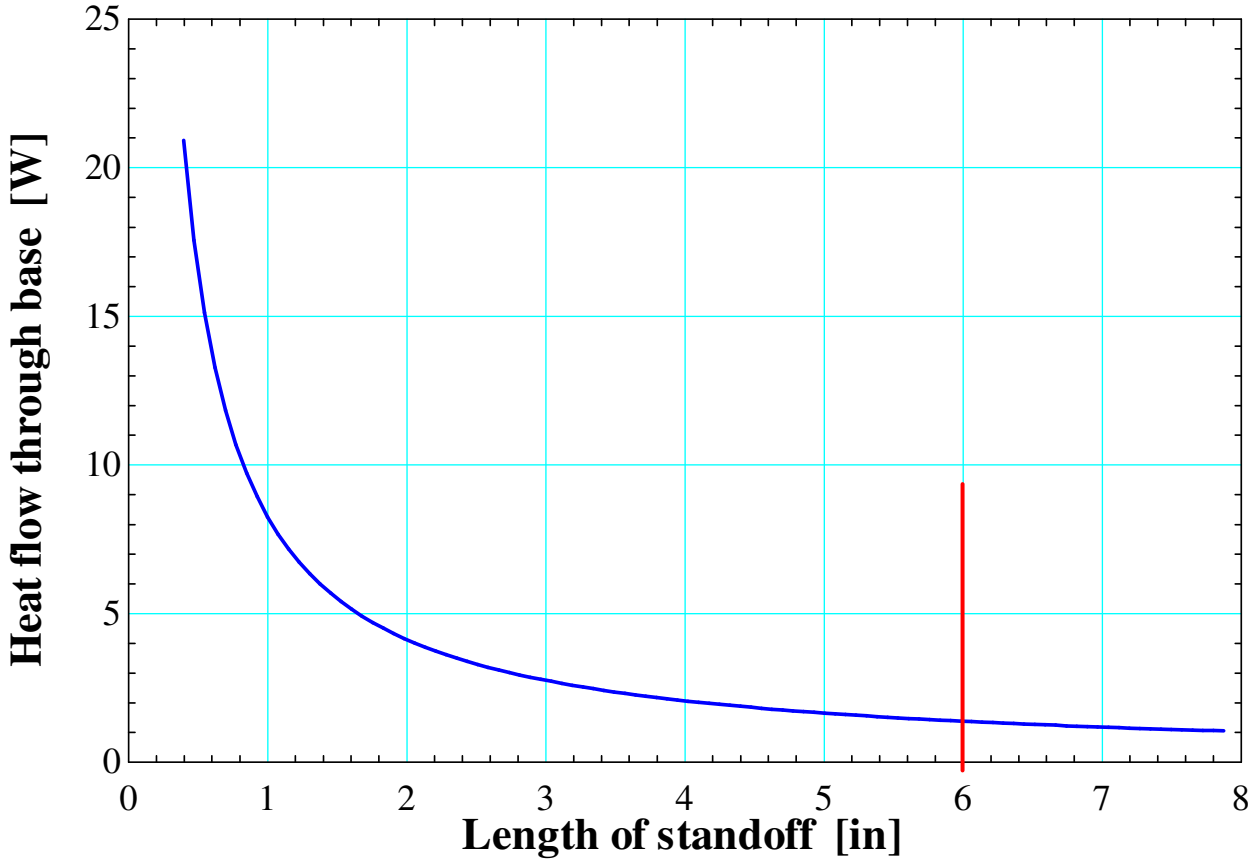

Figure 3.5: This shows the heat flow through the base of the standoff as a function of its length. As the heat flow through the base decreases, more heat transfer occurs between the ambient and the standoff by way of convection. Note that after around five inches of length, the heat flow does not change significantly. Therefore, the fin was made 6 inches.

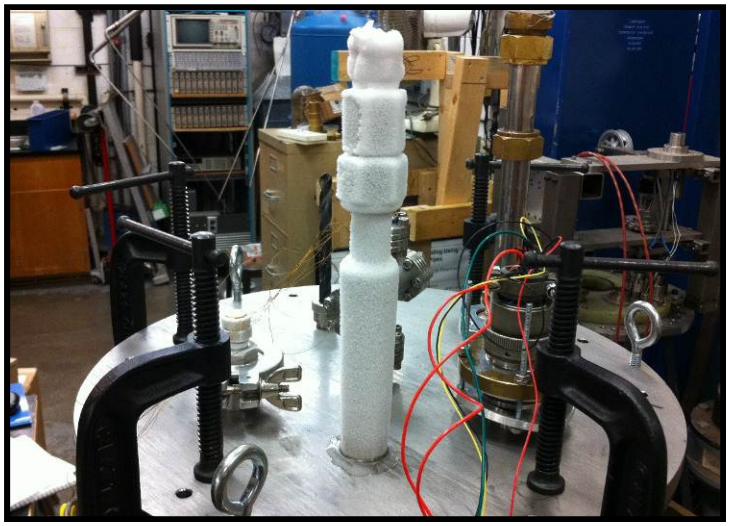

Figure 3.6: The thermal standoff that is designed to minimize frost on the top plate during pump-out. In this picture, it has been fitted with a pressure relief valve for liquid boil off and as can be seen, is working to prevent the top plate from developing a cold frost layer.

A pressure relief valve was installed on top of the standoff to prevent cryopumping and allow liquid nitrogen used in precooling system components to escape. Additionally, the thermal standoff was used to relieve liquid helium boil-off during operation of the experiment. The standoff is shown performing as intended in Figure 3.6.

3.4 Radiation Shields

Although the experiment is submerged in a well-insulated helium Dewar, the helium radiates to the top plate which is approximately at room temperature (in the absence of any shielding). The heat leak assuming no shielding was calculated and the resulting boil off rate was unacceptably high at approximately 0.2 l/min just due to radiation. Using heat transfer relations shown in Equations 3.1-3.4, radiation heat loss was considered through the vertical axis of the cylindrical experiment with the addition of radiation shields. The resistance network used in the model is shown in Figure 3.7. The expected radiation heat transfer using temperature differences combined with the enthalpy of vaporization of helium were used to create Figure 3.9 which

compares the boil off rate as a function of the number of heat shields using aluminum shields with an estimated emissivity $\varepsilon = 0.18$. The estimated emissivity of the stainless steel ends was $\varepsilon = 0.35$.

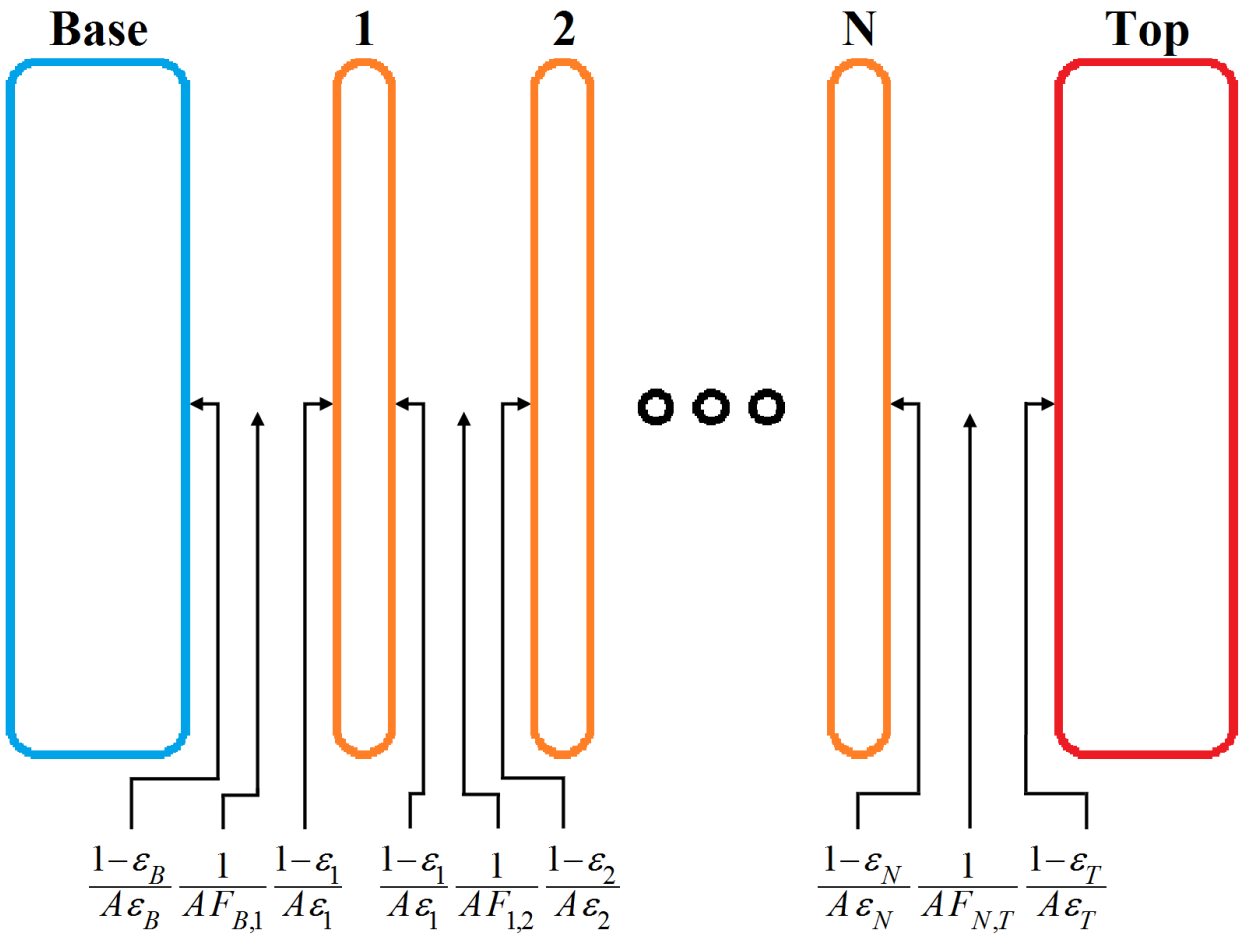

Figure 3.7: The radiation resistance network that governs the model. Surface resistances are shown on each aluminum heat shield and on the stainless steel base and top plate. Space resistances are shown in between each surface with a corresponding view factor F. Emissivity is denoted by ε. The cross sectional area of each section, which is the same for every section, is A. N is a variable representing the number of heat shields (Jahromi 2011).

Equation 3.1 shows that the heat flow through the network of Figure 3.7 is a resistance calculation driven by the difference in blackbody emissive powers of the stainless steel base and top plate Eb_B and Eb_T.

$$Q = \frac{Eb_B - Eb_T}{R_{total}} \tag{3.1}$$

The resistance R_{total} is a function of the surface emissivities and view factors between surfaces, as shown in Equation 3.2.

$$Q = \frac{\sigma(T_{Top}^4 - T_{Bottom}^4)}{\frac{1-\varepsilon_B}{A\varepsilon_B} + \frac{1}{AF_{B,1}} + \frac{1-\varepsilon_{1,B}}{A\varepsilon_{1,B}} + \frac{1-\varepsilon_{1,2}}{A\varepsilon_{1,2}} + \ldots + \frac{1-\varepsilon_{N-1,N}}{A\varepsilon_{N-1,N}} + \frac{1-\varepsilon_N}{A\varepsilon_N} + \frac{1}{AF_{N,T}} + \frac{1-\varepsilon_T}{A\varepsilon_T}} \tag{3.2}$$

Equation 3.2 is represented in Figure 3.7; the equation is the expanded form of the resistance with σ being the Stefan-Boltzmann constant. Combining like-terms provides:

$$Q = \frac{A\sigma(T_{Top}^4 - T_{Bottom}^4)}{\left(\frac{1}{\varepsilon_T} + \frac{1}{\varepsilon_B} - 1\right) + \left(\frac{1}{\varepsilon_{1,B}} + \frac{1}{\varepsilon_{1,2}} - 1\right) + \ldots + \left(\frac{1}{\varepsilon_{N-1,N}} + \frac{1}{\varepsilon_{N,T}} - 1\right)} \tag{3.3}$$

Simplifying Equation 3.3 produces the relationship for the radiation heat transfer between a top plate and a bottom plate that are at different temperatures but have the same cross sectional area with spacers of emissivity ε as shown by Eq. 3.4. T_{Top} is the temperature of the upper surface, and T_{Bottom} is the temperature of the bottom surface. ε_T is the emissivity of the top surface, and ε_B is the emissivity of the bottom surface.

$$Q = \frac{A\sigma(T_{Top}^4 - T_{Bottom}^4)}{\left(\frac{1}{\varepsilon_T} + \frac{1}{\varepsilon_B} - 1\right) + N\left(\frac{2}{\varepsilon} - 1\right)} \tag{3.4}$$

Equations 3.1-3.4 neglect the fact that the shields also "see" a part of the walls of the Dewar in order to make the analysis simpler. Equation 3.4 is an approximation that will work for any large cross section, as long as the end points and the spacers are the same surface area. The corresponding EES program is:

```
$unitsystem K, kg, Pa, s, J, m
"Boil-off of Helium using radiation shields"
epsilon_s =0.18                                   "Emissivity of aluminum plates"
epsilon_o = .35                                   "Emissivity of stainless steel ends"
{N = 1                                            "Number of radiation shields"}
sigma = sigma#                                    "Stefan boltzmann constant"
T_h = 300[K]                                      "Hottest temperature"
T_c = 4.2[K]                                      "Coldest temperature"
D  = 13[in]*convert(in,m)                         "Diameter of the plates and Dewar"
A = pi*(D/2)^2                                    "Cross sectional area"
Q = A*sigma*(T_h^4-T_c^4)/((1/epsilon_o+1/epsilon_o-1)+N*(2/epsilon_s-1))"Heat transfer through the
plates"
P = 1[atm]*convert(atm,Pa)                        "Atmospheric pressure"
h_fg = enthalpy(helium, x = 1, P = P) - enthalpy(helium, x = 0, P = P) "Enthalpy of vaporization"
rho = density(helium, x = 0, P = P)               "Density of liquid helium"
T_nbp = temperature(helium, x = .5, P = P)        "Normal boiling point of helium at this pressure"
E_req = h_fg                                      "Required energy to vaporize"
(q/E_req)*convert(kg/s,kg/min) = Rate             "Rate of boiloff"
V_rate= Rate/rho*convert(m^3/min, l/min)          "Volumetric rate of boil off"
height_rate = (Rate/rho/A)*convert(m/min, in/min) "Height rate"
Cost = 8.5[$/l]                                   "Cost of helium"
D_rate = Cost*V_rate     "Cost rate"
```

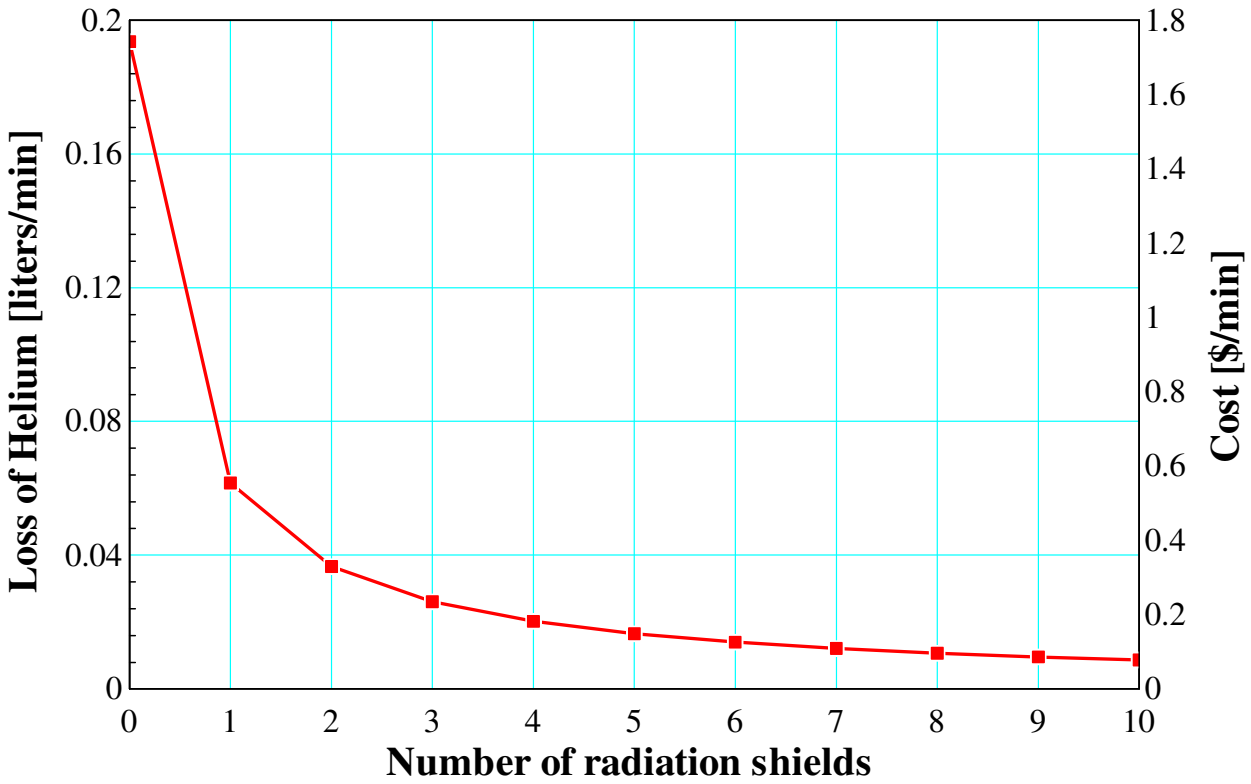

Figure 3.8: Loss of helium and cost as a function of the number of radiation shields. For this experiment, three shields were chosen because after this point each additional shield does not lessen the heat leak significantly. A typical cost of 8.50 $/liter was chosen, although the cost will probably be even higher at the time of this publication.

Approximately 20 layers of multilayer insulation were placed on the warm side radiation shield where it is most effective. Multilayer insulation (MLI) is composed of alternating layers of reflective foil layered with an insulating material such as fiberglass fabric. The foil layers work to reduce radiation heat transfer while the poor-conductivity alternating sheets reduce solid conduction heat transfer. MLI will allow gaseous conduction unless a vacuum is used (Barron 1985). Thus, in this experiment the MLI will not be as effective as possible because the inner chamber is at nearly atmospheric pressure. The installed MLI is shown in Figure 3.9.

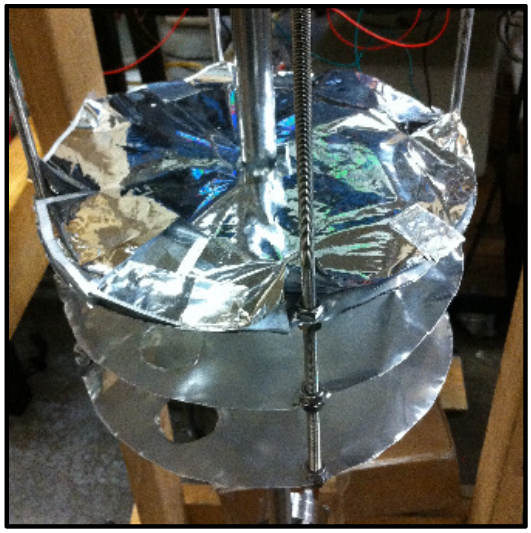

Figure 3.9: This shows the multilayer insulation that sits atop three radiation shields to limit radiation heat transfer to the bath of liquid helium that will sit below.

3.5 Axial Conduction Through Supports

Axial conduction through support members and the pressure chamber neck had to be investigated because too much heat flow here could mean the cryostat would be unable to hold liquid helium. One end of each stainless steel structural member was at 300 K and the other was at the 4.2 K saturation temperature of liquid helium. The conductivity varies greatly for most materials in this temperature range.

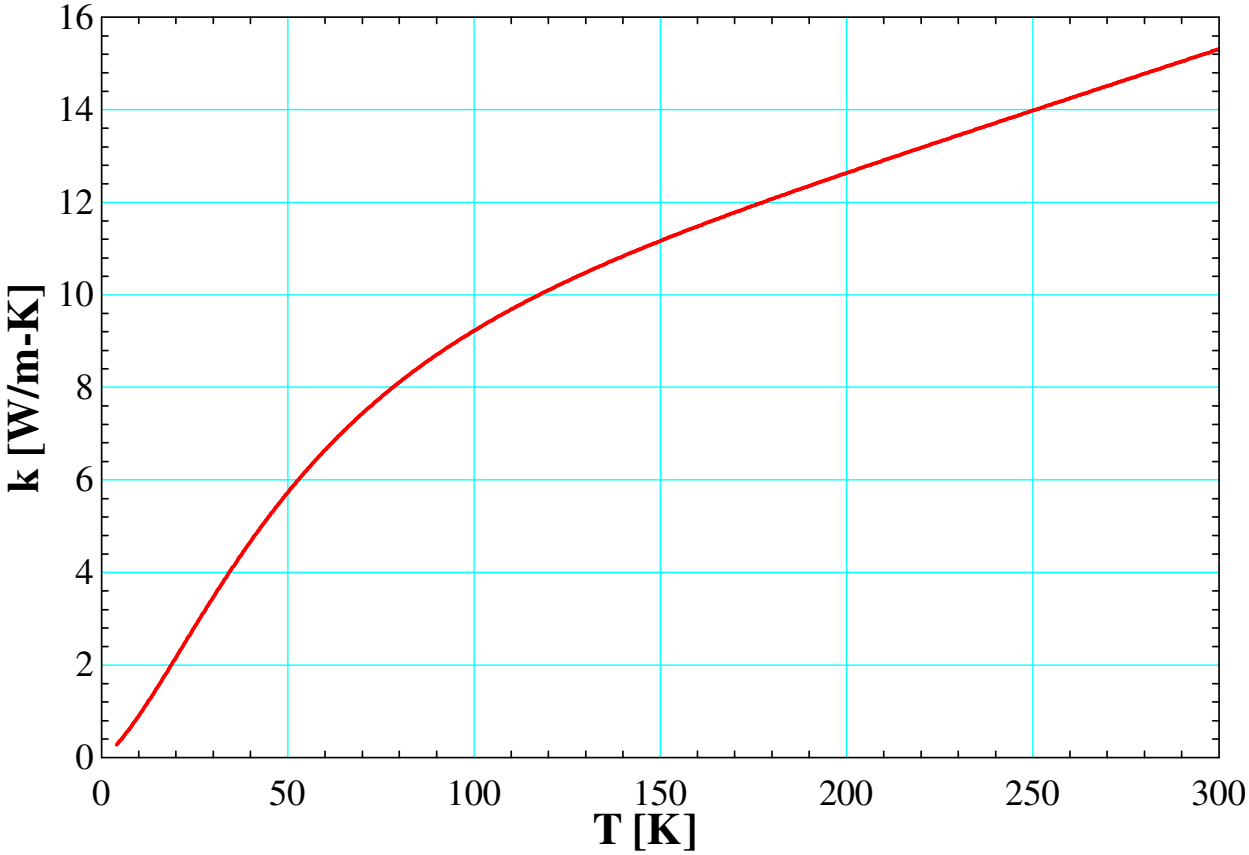

Figure 3.10: Conductivity of stainless steel 304L as a function of temperature.

The conductivity curve shown in Figure 3.10 is for stainless steel 304L. The conductivity can be integrated with respect to temperature and used to compute the rate of conduction heat transfer according to:

$$q_{cond} = \frac{k_{\text{int}} A_{tot}}{L} \tag{3.5}$$

where k_{int} is the integrated thermal conductivity between cold and hot temperatures, A_{tot} is the total cross sectional area of supports in thermal communication with the ambient and liquid helium, L is the length of a support, and q_{cond} is the resultant conduction heat leak associated with the members. Integrated thermal conductivity is useful in any case where there is a large temperature gradient through a material with temperature-dependent conductivity when heat

transfer is occurring only in one direction. Using a typical cross sectional area per support of 0.0004 m^2 and a length of each support of 3 m, the boil off losses of helium attributable to axial conduction were determined as a function of the number of supports, as shown by the following EES code and in Figure 3.11.

```
"Program that calculates axial conduction heat leak through supports"
"Conductivity polynomial for stainless steel"
k = 10^(-1.4087+1.3982*(log10(T*1[1/K])) + 0.2543*(log10(T*1[1/K]))^2 + -0.6260*(log10(T*1[1/K]))^3 +
0.2334*(log10(T*1[1/K]))^4 + 0.4256*(log10(T*1[1/K]))^5 + -0.4658*(log10(T*1[1/K]))^6 +
0.1650*(log10(T*1[1/K]))^7 + -0.0199*(log10(T*1[1/K])) ^8)*1[W/m-K] "From NIST (Marquardt  2000)"
k_int = integral(k,T, 4.2[K], 300[K])                    "Integrated thermal conductivity"
N = 1[-]                                                 "Number of supports"
A_c = 0.0004[m^2] *N                                     "Cross sectional area of supports"
L = 3[m]                                                 "Length of support"
q_cond = k_int*A_c/L                                     "Conduction heat leak"
DELTA_hfg =enthalpy(helium, T = 4.2[K], x = 1) -enthalpy(helium, T = 4.1[K], x = 0) "Latent heat of
helium"
Loss_He = (q_cond/DELTA_hfg)*convert(kg/s, kg/min)       "Loss of helium in kg/s"
rho_helium = density(helium, T = 4.2[K], x = 0)          "Density of helium"
Loss_He_v = (Loss_He/rho_helium)*convert(m^3/min, l/min) "Loss of helium in l/s"
```

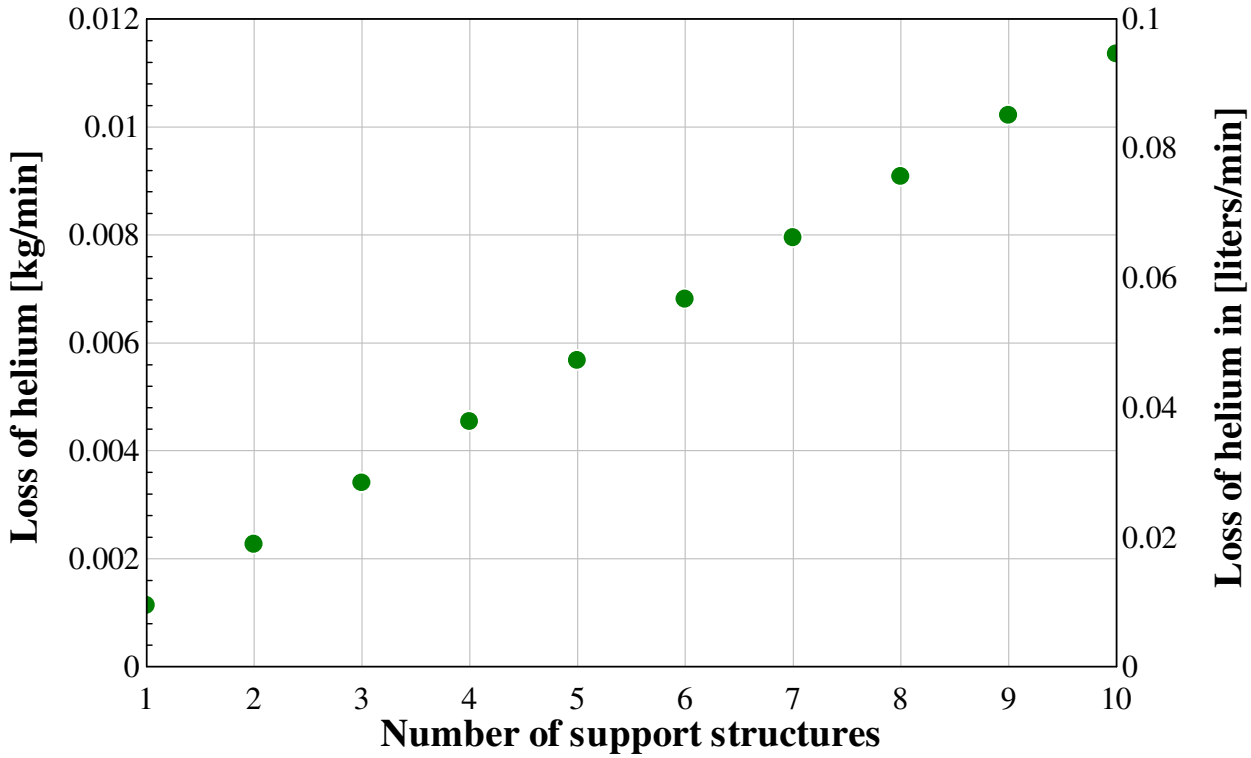

Figure 3.11: The loss of helium as a function of the number of support structures connected between the liquid helium bath and the top plate.

Similar analyses were used to verify that a liquid helium transfer guide tube, threaded rods for radiation shields, the tube connecting the test chamber to the top plate, and a thin-walled pipe used in calibration would not create too much heat leak (e.g., more than a few inches of helium lost per hour). The heat leak analysis for each component is shown in Table 3.1.

Table 3.1

Component	Quantity	Area (m^2)	Leak (l/min)	Leak (in/min)	Leak (in/hr)
Calibration tube	1	0.000158	0.00797	0.00366	0.2196
Guide tube	1	0.000158	0.00797	0.00366	0.2196
Radiation shields	1	0.0856	0.026	0.01197	0.7182
Threaded rods	4	0.000116	0.00586	0.00269	0.1614
Chamber tube	1	0.000158	0.00797	0.00366	0.2196
Total:		0.086032	0.0478	0.02198	1.3188

Note that in Table 3.1, the quantitative results for the threaded rods have been multiplied by a factor of four. Also, the calibration tube is not included in any of the totals because it is not part of the final experiment.

3.6 Helium Pressure Bottle and Line

A helium gas cylinder was needed for transferring liquid helium, pumping out liquid nitrogen used in precooling, and for pressurizing the test chamber. A size 300 (50 liter) bottle was chosen from Airgas and filled with high purity grade helium gas. An Airgas dual stage pressure regulator with an adjustable outlet pressure between 0 and 250 psig was chosen to accommodate the required 1 MPa (~150 psig) of the experiment.

A pressure line was needed to connect the helium bottle to the experiment. The Conflat cross on the top plate was machined and tapped with 1/4” National Pipe Thread Tapered Thread (NPT), and then a brass fitting was attached. A 150 psig Circle Valve Technology pressure relief

valve was installed on the fitting to ensure that on warm-up any excess pressure would be vented.

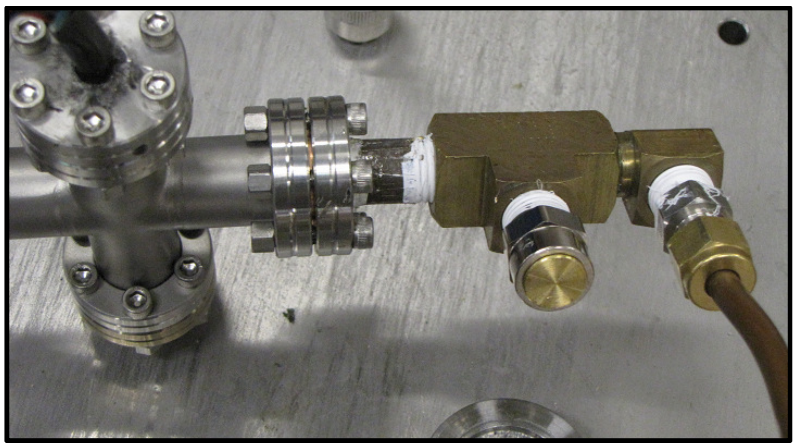

Figure 3.12: Shown is the 1 MPa helium pressure line connected to the Conflat cross using a brass fitting equipped with a relief valve. The stainless steel Conflat flange was tapped to 1/4" NPT.

3.7 Custom Connections

Multiple types of custom connections were required for the experiment. Wires must enter the CF cross on the top plate from atmospheric pressure to 1 MPa, thus a feed-through is necessary. A hole was drilled in a CF flange of the cross, wires were inserted, and the hole was filled with Stycast 2850 epoxy to create a plug that could withstand moderate pressures. This is shown:

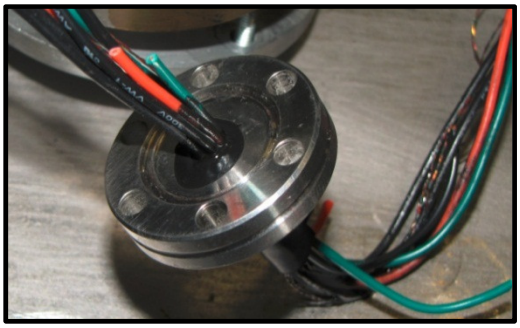

Figure 3.13: A wire feed-through made from Stycast 2850. The high pressure side is shown in this picture. Note that with rubber insulated wires, this feed-through is not vacuum ready and would leak. The rubber must be stripped and the wires have to be individually varnished if a vacuum is to be pulled on this piece.

Another custom wire feed-through that was fabricated was a KF-25 wire port for the liquid helium level meter and a plate heater that sits at the bottom of the Dewar. This port runs into the main experiment bath, so it only has to withstand the moderate pressures used in pump-outs and possibly vacuum in the future. This feed-through works by compressing a KF rubber seal:

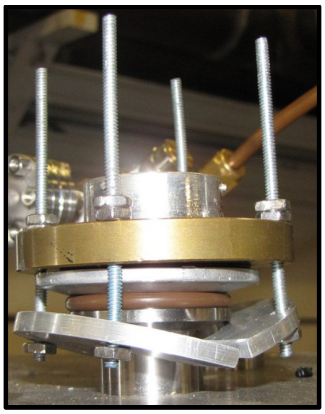

Figure 3.14: A KF-25 wire feed-through that can withstand moderate pressures and vacuum.

The last type of connection created was purely mechanical (i.e., no electronics were involved). It is an adaptor fitting that converts 3/4" Swagelok to KF-25. A seal was needed between a thin-walled stainless steel tube and the KF-25 port that it was fed through. Although many types of connections can be purchased from companies, this one could not. Thus, a brass KF flange was brazed to a Swagelok fitting:

Figure 3.15 A custom brazed 3/4" Swagelok to KF-25 fitting. This fitting can withstand moderate pressures used in pump-out applications.

3.8 Temperature Sensors and Measurement

Temperature sensors that were rugged, accurate between 4.2 K and 20 K, and had small thermal mass to ensure a fast time response were needed to track changes in the transient temperature of a test regenerator. The Cernox-1050-SD was chosen; it is relatively inexpensive and fulfills all of these requirements. The SD package has a mass of only 30 mg, making it much lighter than any package that has a threaded housing. Although light, the package is still durable because it was designed to be clamped to surfaces. It has two leads with visible solder joints to the chip; therefore in the worst case that a solder joint breaks it can still be repaired.

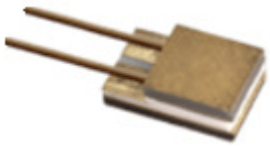

Figure 3.16: Shown is a Cernox-1050 with the SD package. The sensor width measures 1.9 mm.

One calibrated and three uncalibrated sensors were obtained for the experiment. The variable resistance behavior of the sensors at different temperatures makes it possible to accurately measure temperature within certain ranges. The temperature behavior of the calibrated Cernox is shown:

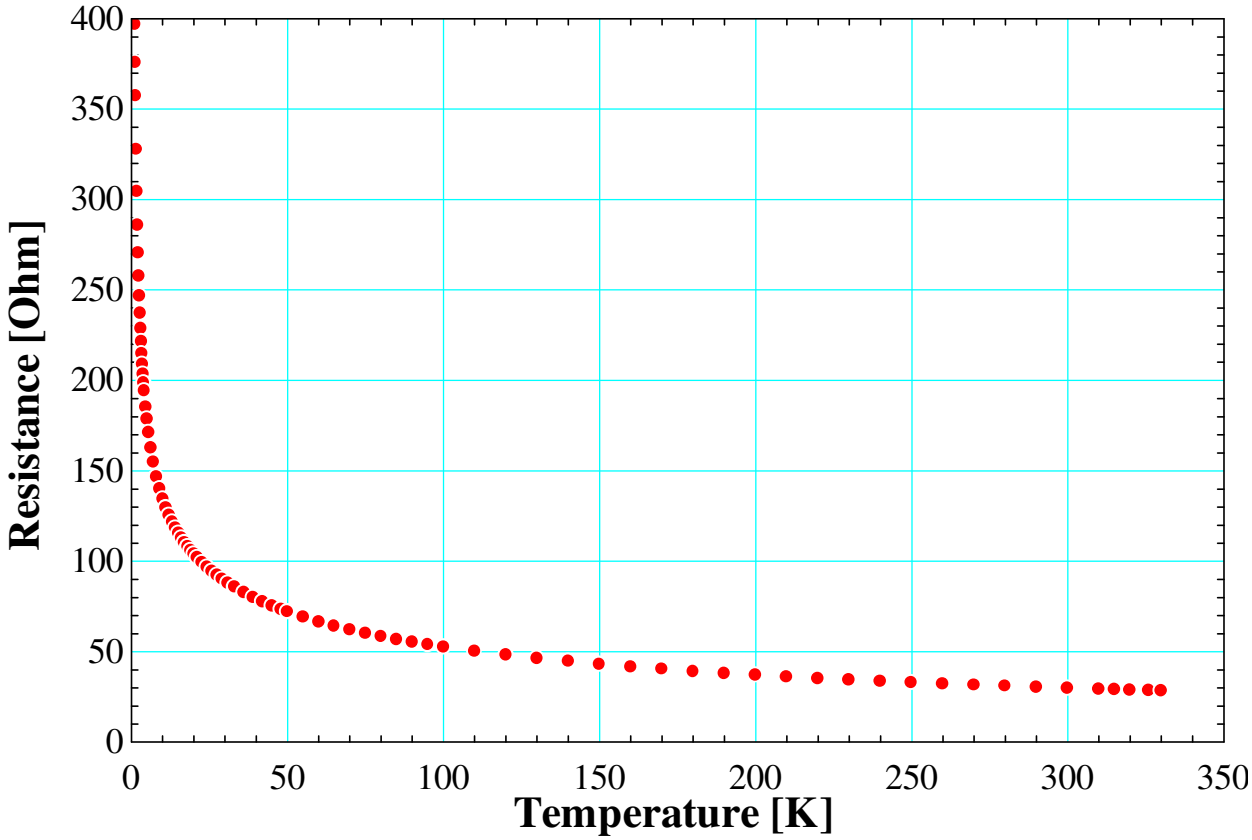

Figure 3.17: The resistance of the calibrated Cernox as a function of temperature from 1.2 K to 330 K.

As shown in Figure 3.16, the Cernox sensor is difficult to use above around 100 K because even when temperature changes by a large amount, the resistance of the Cernox does not change much. To account for this, some experiments use variable DC current sources so that a higher voltage can be obtained at higher temperatures using a greater current. This experiment uses a fixed current source, so high accuracy at room temperatures is unobtainable.

The method of measuring temperature using a current source needs explaining. One might think that since wires are attached to sensors and this wire has resistance, backing out the resistance change of the sensors would be arduous because the measured voltage would capture the voltage drop over the attached leads as well. Figure 3.18 shows the method of measuring temperature that avoids the voltage drop over the current leads.

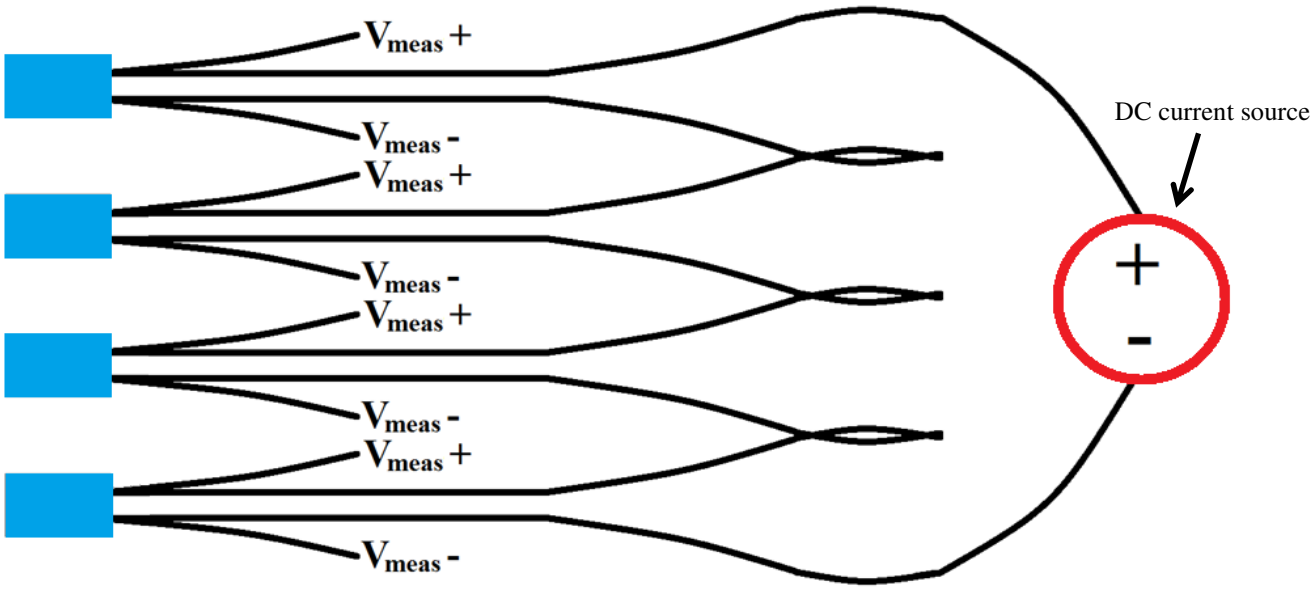

Figure 3.18: The method of creating and measuring a voltage with four Cernox sensors. The current source is located on the right side.

The sensors are wired in a series circuit and a DC current is sent through the leads. Each sensor has its own set of two additional leads that only measures the voltage across the resistive sensor; this voltage is labeled V_{meas} in Figure 3.18. The voltage measurement leads can be extended to any length and still will only measure the voltage drop across the sensor since there is no current in these leads. The leads in this experiment are connected to a LabVIEW data acquisition board, which is discussed more in Section 3.9. One drawback to measuring temperature with a series-resistance network of sensors is that if a current lead in one sensor breaks, none of the other sensors will have any voltage drop across them, therefore temperature cannot be measured by any of the sensors in this case. Care must be taken to protect wire connections.

The wiring used to connect the sensors is important to reduce the noise of measured signals. If sensor wires are just individual wires, electromagnetic interference from the surroundings can induce errors in measurements taken by the wires by a small amount. Twisting two wires of opposing current around each other cancels out this interference and thus, twisted

pairs are used and the pair is split apart where a connection is needed. Lake Shore Quad-Twist is used in this experiment; this cable consists of two twisted pairs of insulated non-ferromagnetic phosphor bronze wires.

3.9 Data Acquisition

Data acquisition is accomplished using LabVIEW with minimum filtering, as shown:

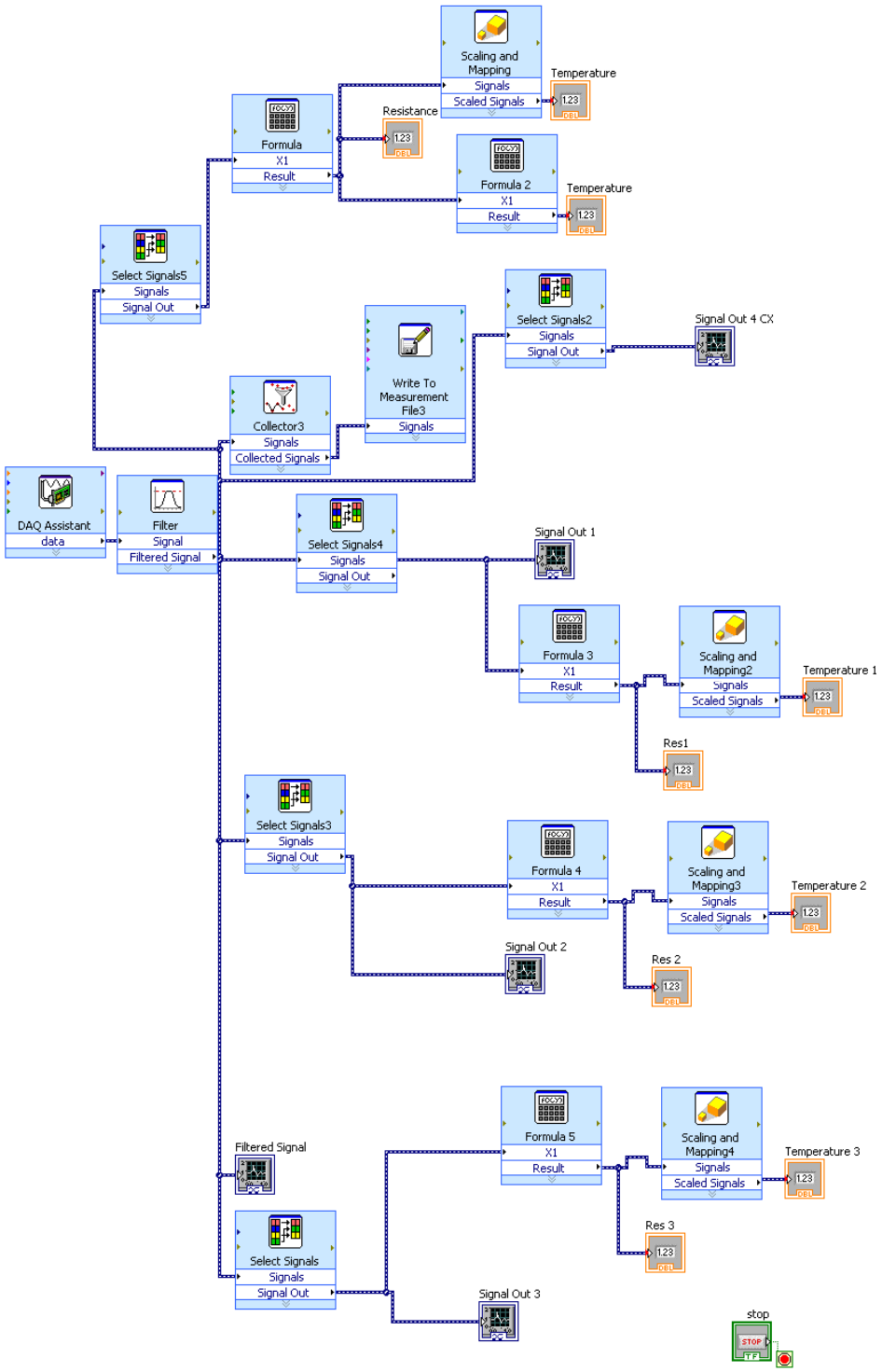

Figure 3.19: The LabVIEW block diagram showing mapping functions for four Cernox temperature sensors. Minimum filtering is used to preserve the signal quality.

Voltage data from the four temperature sensors enter a National Instruments CB-68LP 68 pin connector block. This block is received by a NI PCI-6221 data acquisition board. The LabVIEW program shown in Figure 3.19 reads voltage data from the temperature sensors. Using a known electrical current from the current source, the resistance of each sensor is calculated. The resistance of each sensor varies based on temperature. Using the manufacturer's calibration curve for the main Cernox sensor and acquired calibration curves of the other sensors, the temperature of each sensor can be interpolated using its resistance. Mapping functions in the LabVIEW block diagram achieve this. The main panel is shown below:

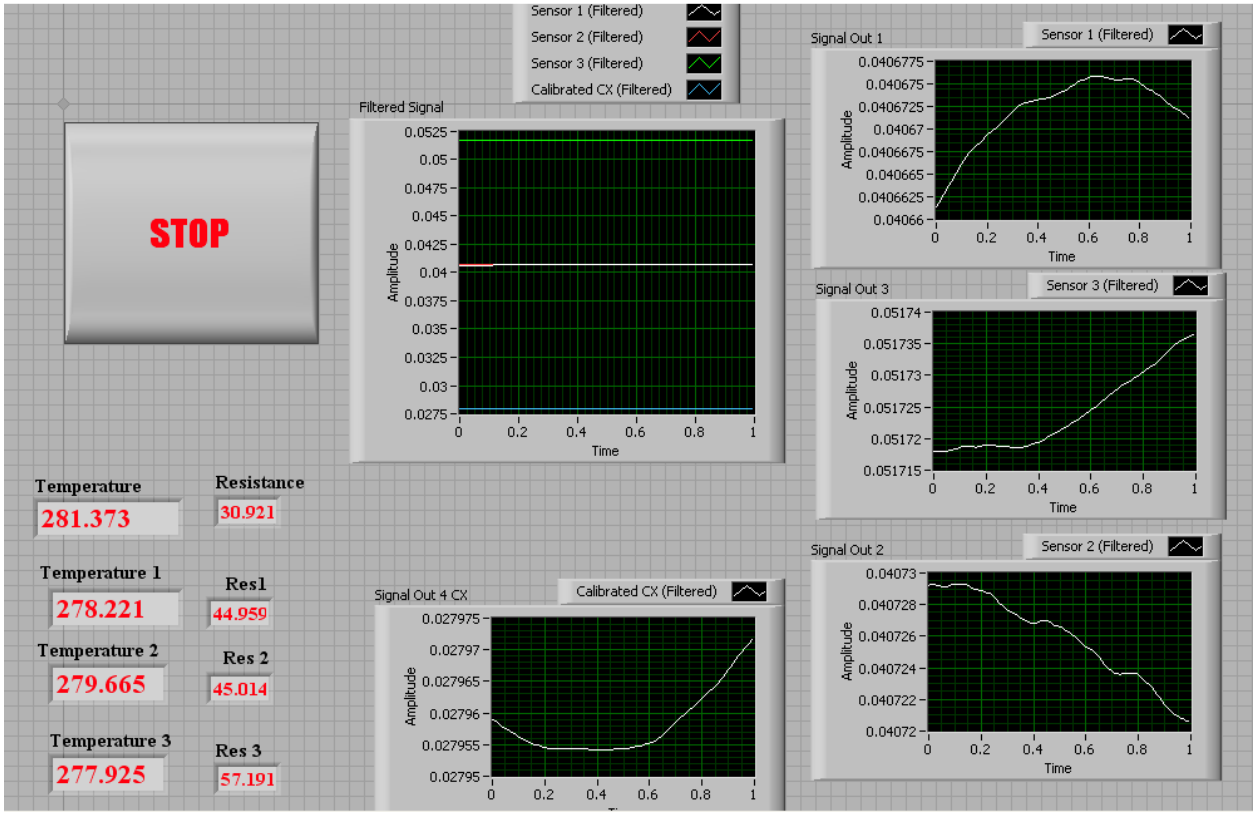

Figure 3.20: The front panel of the LabVIEW program for the temperature sensors. The center graph shows the sensors' voltages in relation to each other. The other four graphs show the highly magnified voltage of individual sensors. The instantaneous temperatures are shown at the lower left; note that Cernox sensors are inaccurate at ambient temperatures; this is discussed in Section 3.8.

3.10 Other Electronics

-Level indicator-

An American Magnetics Model 110A liquid helium level meter was chosen to monitor the amount of helium in the Dewar. This had to be calibrated to accommodate the active sensor length and was wired through the top plate of the experiment using the connector shown in Figure 3.14. The actual sensor has 18 inches of active length.

Figure 3.21: The liquid helium level meter. The level of helium is shown as a percentage of the 18 inch sensor.

-Current sources-

Lake Shore Cryotronics Model 101 and Model 102 current sources are used in the experiment. Both of them had to be internally calibrated by re-soldering a resistor inside to increase the output current. Although the output current should not change much once it is set, a 1 kΩ resistor was used to back-out the current by measuring the voltage across the resistor to verify the operation. This method was useful in identifying slight deviations in current and also to check if the battery of the Model 101 current source was providing constant power. The Model 101 current source, which is used predominantly, is set at 0.00090459 A, or approximately 0.9 mA. The other current source is set a factor of ten lower and is only useful below temperatures of

around 20 K; with higher resolution data acquisition than currently is used, this lower current would be more accurate because it would avoid any self-heating error of the Cernox sensors.

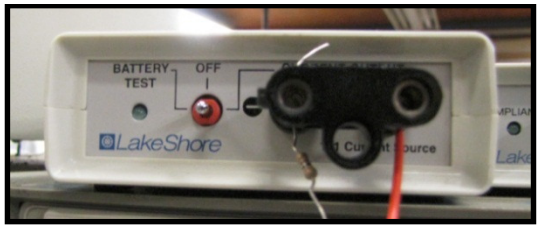

Figure 3.22: A DC current source used in the test setup. The resistor seen in the photo is the 1 kΩ verification resistor. The resistor and the red wire complete the four-Cernox-sensor circuit that is described in Figure 3.18.

-Heaters-

Two Lake Shore Cryotronics HTR-25-100 nickel-chromium resistance wire cartridge heaters are used in the test apparatus to send out various heating functions. The heaters are rated at 100 W but can withstand much more power than this when either mounted to a “thermal reservoir” or immersed in a cryogen such as LN2 or liquid helium. A third resistance plate heater is used to boil off either LN2 used in precooling components or liquid helium if a certain level is desired; the heater lays flat on the bottom of the Dewar.

-Digital multimeter and power supply-

Data acquisition is verified by a Hewlett Packard 3468B digital multimeter. Power is sent to various heaters using an HP power supply.

References

[1] Barron, R.F. (1985). *Cryogenic Systems.* New York, NY: Oxford University Press, Inc.

[2] Ekin, J.W. (2006). *Experimental Techniques for Low-Temperature Measurements*. Great Clarendon Street, Oxford: Oxford University Press.

[3] Jahromi, A. (2011). *Development of a 1K facility and modeling of a superfluid magnetic pump with no moving parts*. Thesis, the University of Wisconsin - Madison.

[4] Marquardt, E.D., Le, J.P., and Radebaugh, Ray, *Cryogenic Material Properties Database.* 2000, Boulder, CO: National Institute of Standards and Technology.

[5] Nellis, G. and Klein, S.A., (2009). *Heat Transfer.* New York, NY: Cambridge University Press.

[6] Ventura, G., and Risegari, L., (2008). *The Art of Cryogenics.* Jordan Hill, Oxford: Elsevier Ltd.

4 Test Runs and Experimental Results

4.1 Diagnosis and Resolution of a Problematic Dewar

At the beginning of the design phase of the experiment, the Dewar that was being used to hold the test setup was assumed to be in good working order. This meant the Dewar would hold liquid nitrogen for a long period of time and provide a cold thermal jacket between a vacuum space and an inner helium space. A simplified illustration of the Dewar is shown:

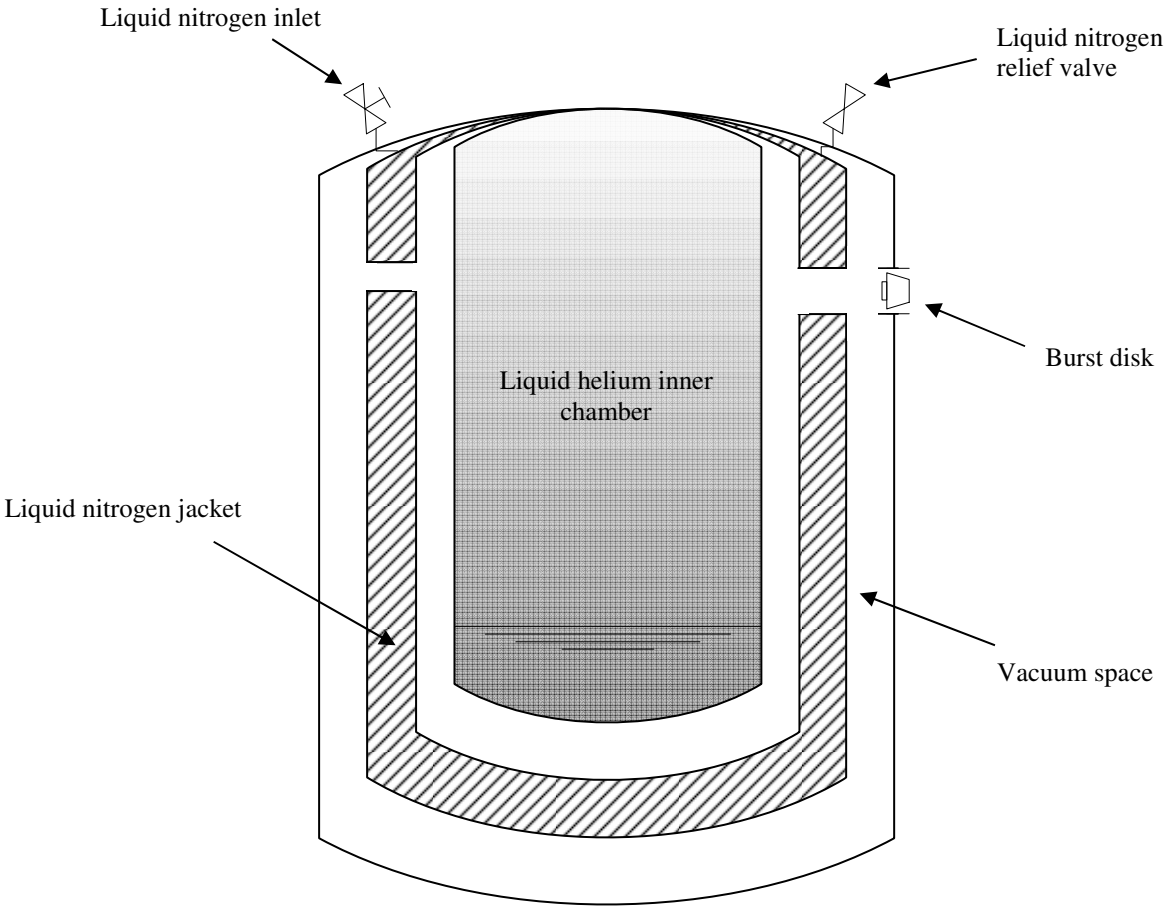

Figure 4.1: A simplified illustration of the Dewar. Note that there is a vacuum space on the outside and inside of the container. Although the vacuum chambers are connected, there is a jacket of liquid nitrogen that is in between the vacuum spaces. The function of the liquid

nitrogen space is that the helium bath only has to be insulated from thermal communication with a 77 K reservoir instead of the much hotter 300 K ambient temperature.

In proper working condition, the outside of the Dewar should not be very cold. The liquid nitrogen should remain in the Dewar for a few days based on some basic heat leak calculations.

Unfortunately, upon running the experiment, it was found that the Dewar was not functioning as anticipated. The liquid nitrogen boiled off in less than one day and water condensed on the side of the cold Dewar and pooled on the floor. Losing liquid nitrogen quickly is not a serious problem because it is relatively inexpensive at around $0.60/liter. The more important problem was that these behaviors are symptoms of a poor vacuum and therefore any liquid helium placed in the Dewar would boil off extremely quickly. The current cost of helium is around $9/liter; therefore, a bad vacuum in the Dewar would be costly.

A vacuum leak in a Dewar can be due to a few different sources. Common locations are where materials are bonded including any valves and burst disks. Sometimes instead of welding, dissimilar materials must be bonded using some type of glue; over the lifetime of a Dewar, these connections can develop leaks. A valve is used to pull the vacuum on the Dewar; sometimes a bellows valve is used. This valve can potentially leak. Burst disks are used in case there is an inadvertent, large positive pressure inside of the vacuum space. This event can occur in the case of warm-up after cryopumping (introduced in Section 3.2). Burst disks can develop leaks as well.

Troubleshooting of the Dewar began with the easiest of potential problems. The vacuum valve was removed and connected directly to a roughing and a turbomolecular vacuum pump and an extremely low pressure was achieved and maintained. Therefore, this valve was not the problem. Next, the two pump configuration was used to evacuate the entire Dewar with the valve, as shown:

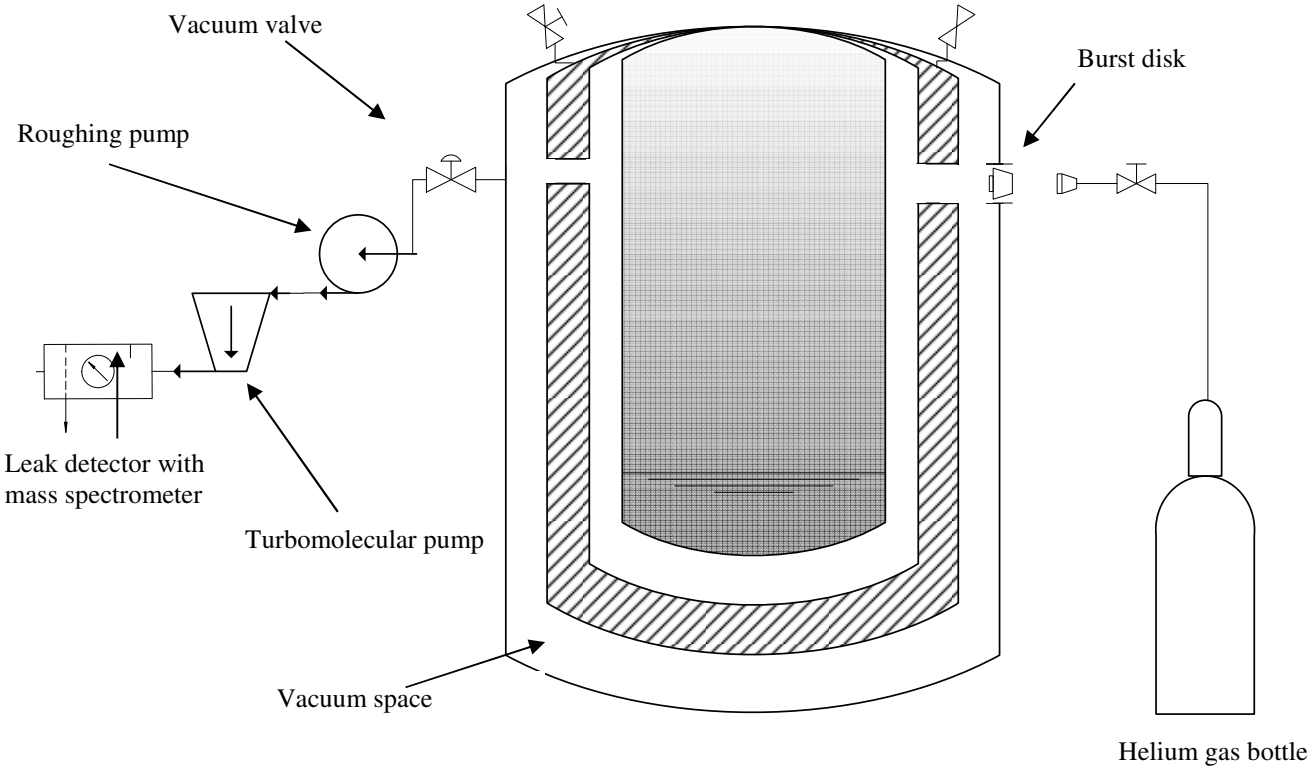

Figure 4.2: An illustration showing the Dewar in vacuum troubleshooting configuration. A roughing pump is used to pull a moderate vacuum on the Dewar and a turbomolecular pump is then activated to achieve a much stronger vacuum. A mass spectrometer is used to identify helium particles pulled from the vacuum space to check for leaks.

A helium gas bottle was used with a nozzle to apply helium gas into different areas of the Dewar. The leak detector registered helium molecules when the gas was dispersed near the burst disk. Therefore, it was concluded that the burst disk was the reason for the bad vacuum. Unfortunately, to repair the burst disk required cutting out the old disk and welding in a new one. This solution was abandoned due to time constraints and the old Dewar was replaced by the Cryofab superconducting magnet Dewar shown in Section 3.1. This new Dewar had a smaller

diameter than the old Dewar; therefore, the experiment had to be disassembled in order to modify the radiation shields, top plate, and stainless steel support structures to fit the new Dewar. Fortunately, the Cryofab Dewar worked well.

4.2 Calibration

Temperature sensors were calibrated using a transient process, which will be described in this section. All four sensors had to be mounted to a material that was isothermal. One sensor was calibrated from the manufacturer, therefore the temperature of the isothermal material at any time was known because the resistance of the sensor could be measured and used to look up the corresponding temperature. All of the other sensors had unknown resistance/temperature curves. Therefore, a transient process that captured the sensor resistances for each sensor over a temperature range of 4.2-300 K was used.

A copper cylinder was chosen as the isothermal mass and used to calibrate three Cernox temperature sensors against the reference sensor. The block had to be machined to accommodate the sensors; 10 centimeters of wire were wrapped around the block to thermally ground the leads, reducing measurement error. The copper cylinder was suspended in liquid helium using a thin-walled stainless steel tube to limit conduction heat leak.

The calibration was performed in the Dewar and used a modified version of the final test setup. After one botched run due to a bad transfer line, the test setup readily accepted liquid helium. The space that held liquid helium under the radiation shields was so well insulated that a plate heater had to be used initially to boil off a few inches of helium so that the block was not completely submerged in liquid helium. The calibration was essentially a trial run for many of the components, as this was the first time liquid helium was used. The calibration technique used

was transient; the test slowly boiled off helium while capturing the behavior of the sensors as the copper block's temperature increased. The block rested at the surface of the helium liquid. Controlled amounts were boiled off using the plate heater. Temperature was allowed to come to nearly a plateau before calibration data were recorded at each point. The height of liquid helium at any moment was known by using the liquid helium level meter.

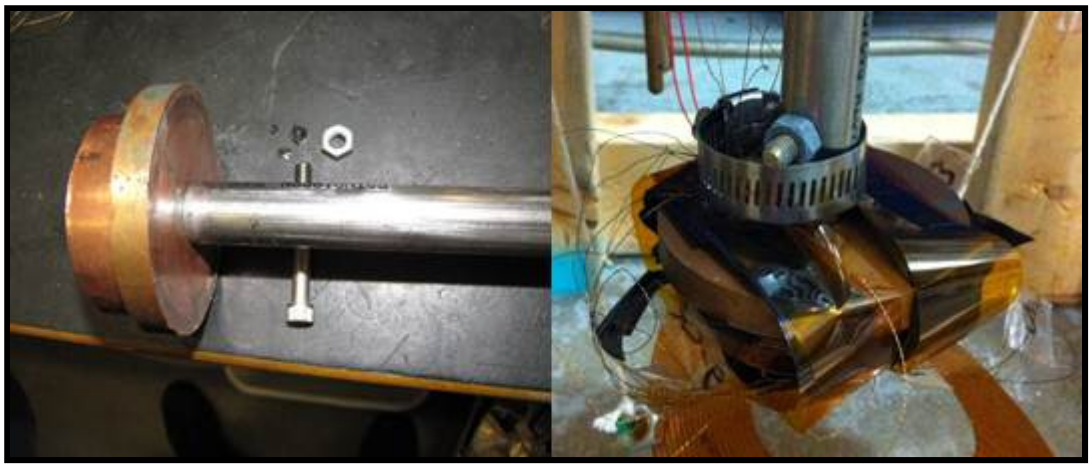

Figure 4.3: The copper mass attached to the thin-walled stainless tube is shown on the left. The copper cylinder that is rigged with the four sensors is attached to the stainless steel tube and fed through the custom flange from Figure 3.15; this is shown on the right.

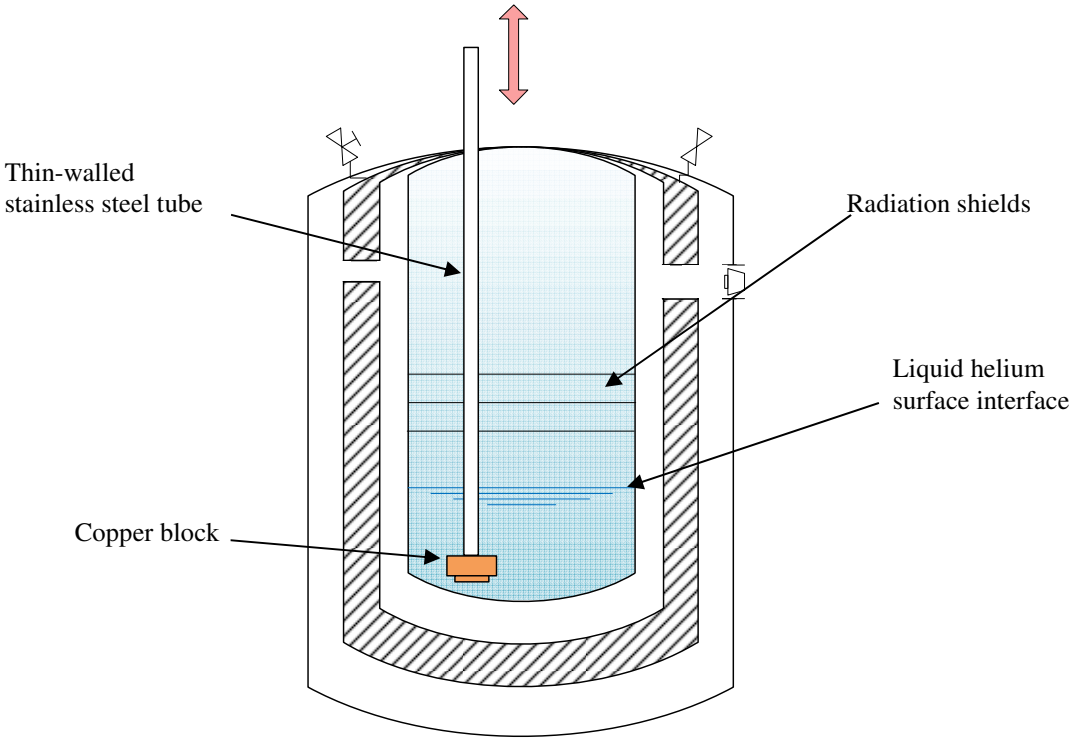

Figure 4.4: The transient calibration method. The thin-walled stainless steel can be raised or lowered. Although the calibration setup was designed for the thin-walled tube to be pulled slowly out of the helium, in the actual calibration a heater was used to boil off controlled amounts of helium, achieving the same result.

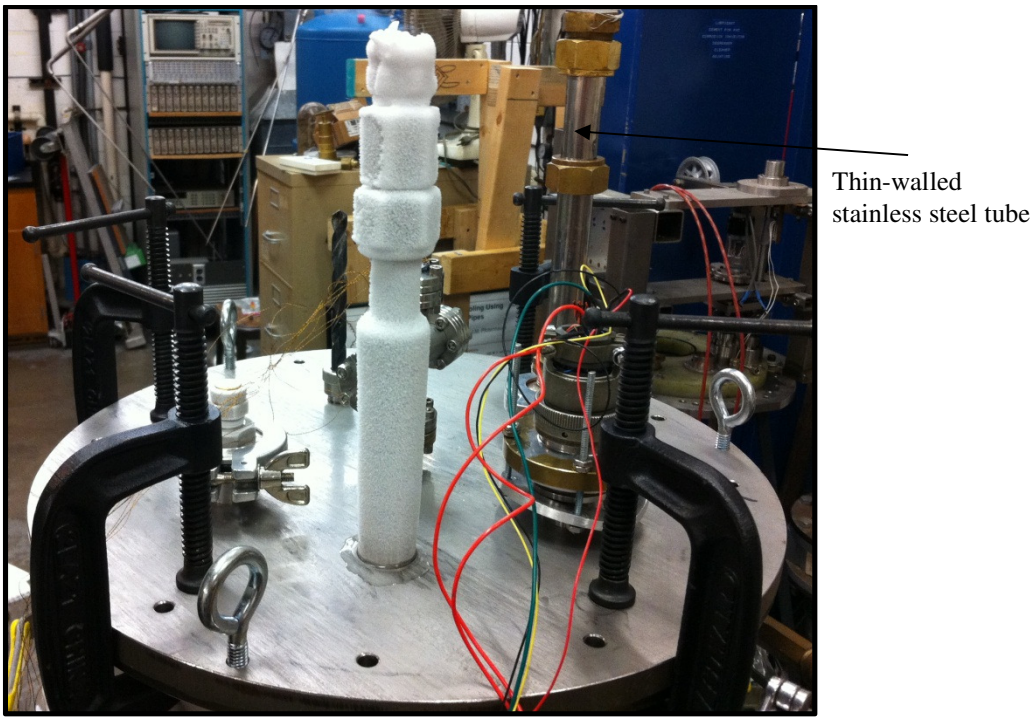

Figure 4.5: The top of the test facility during calibration.

The log-log calibrated results for each Cernox sensor are graphically shown on the following pages. Tabular results are available in the Appendix.

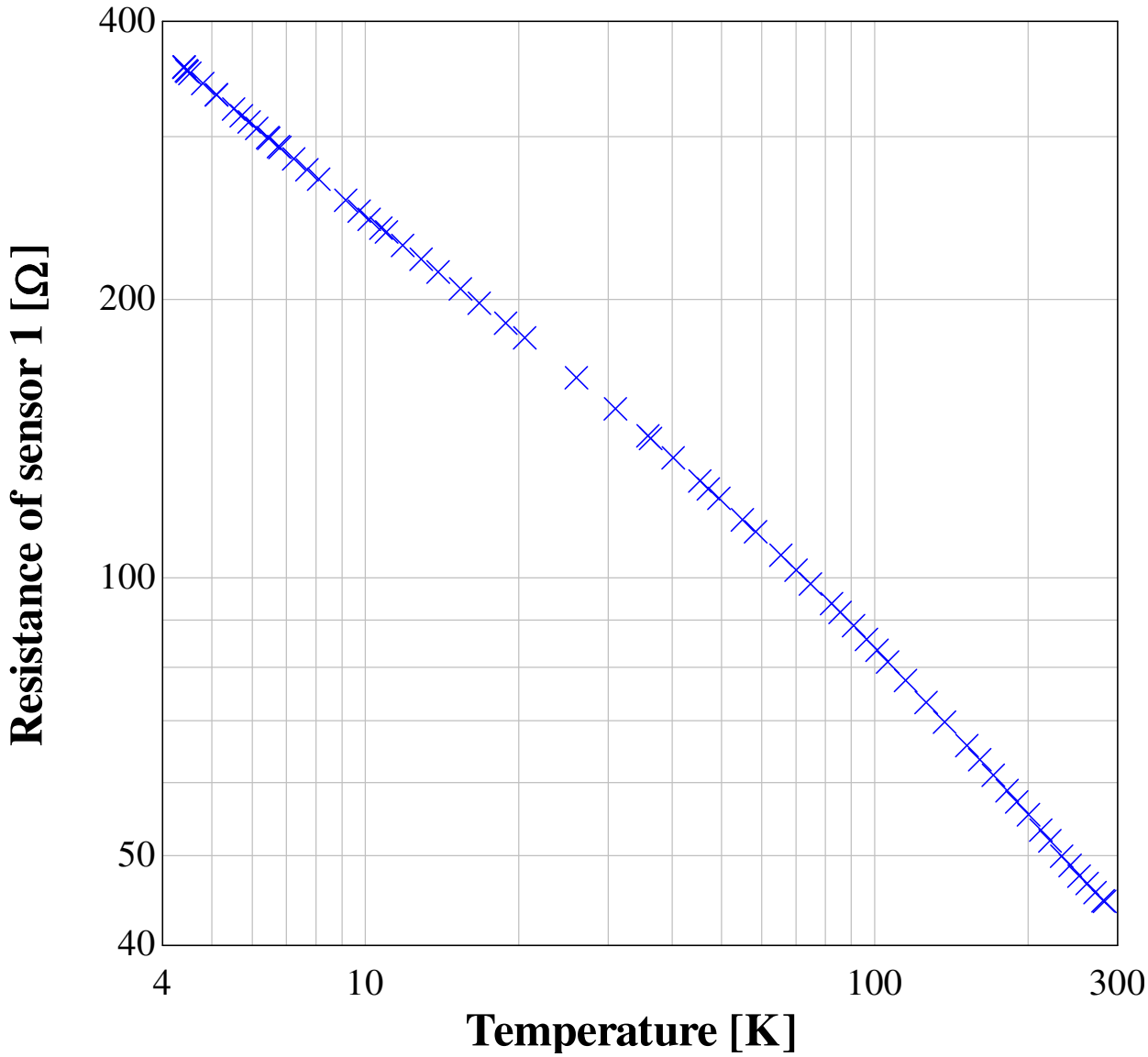

Figure 4.6: The calibration curve for the Cernox temperature sensor #1, showing resistance as a function of temperature.

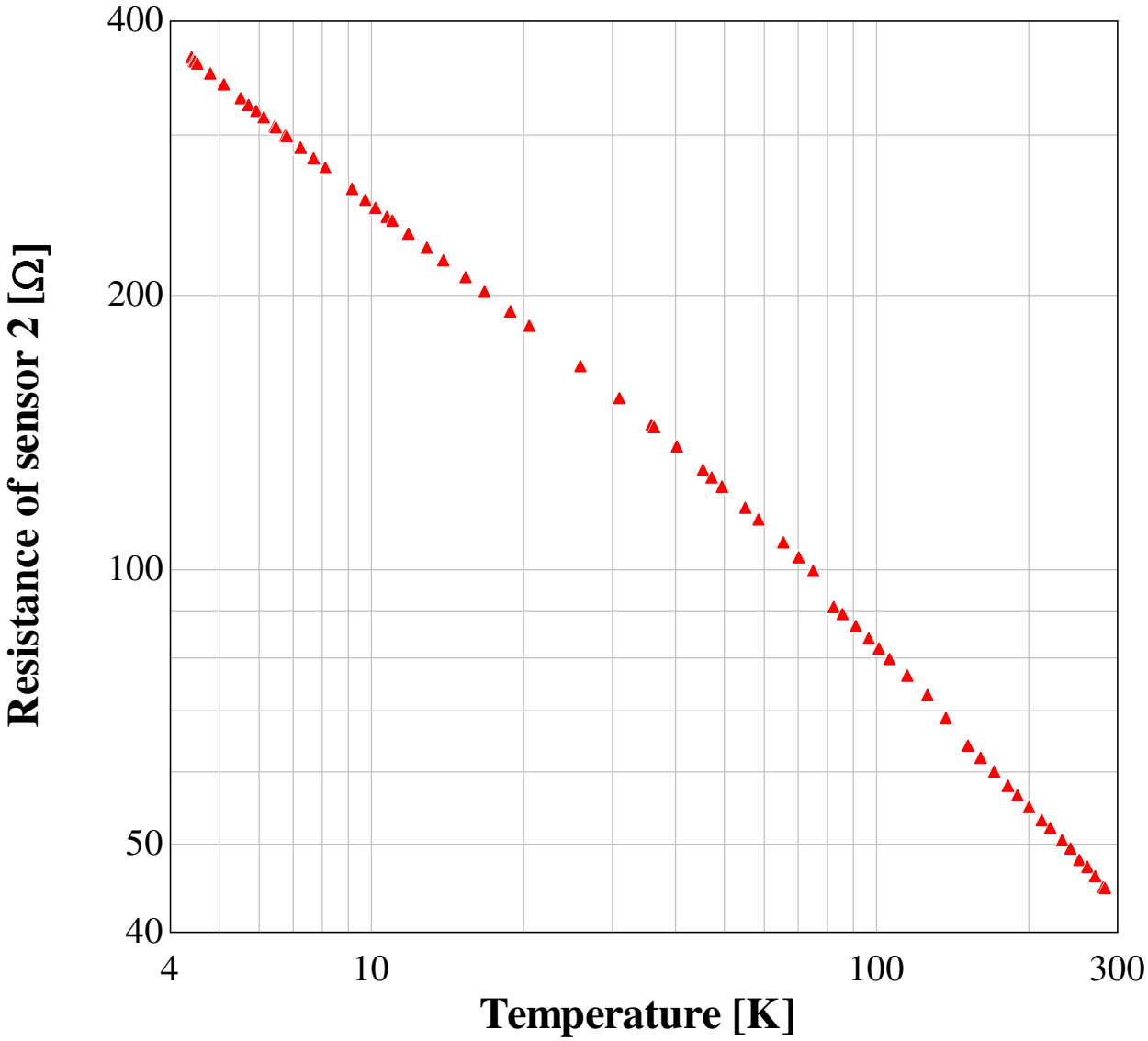

Figure 4.7: The calibration curve for the Cernox temperature sensor #2, showing resistance as a function of temperature.

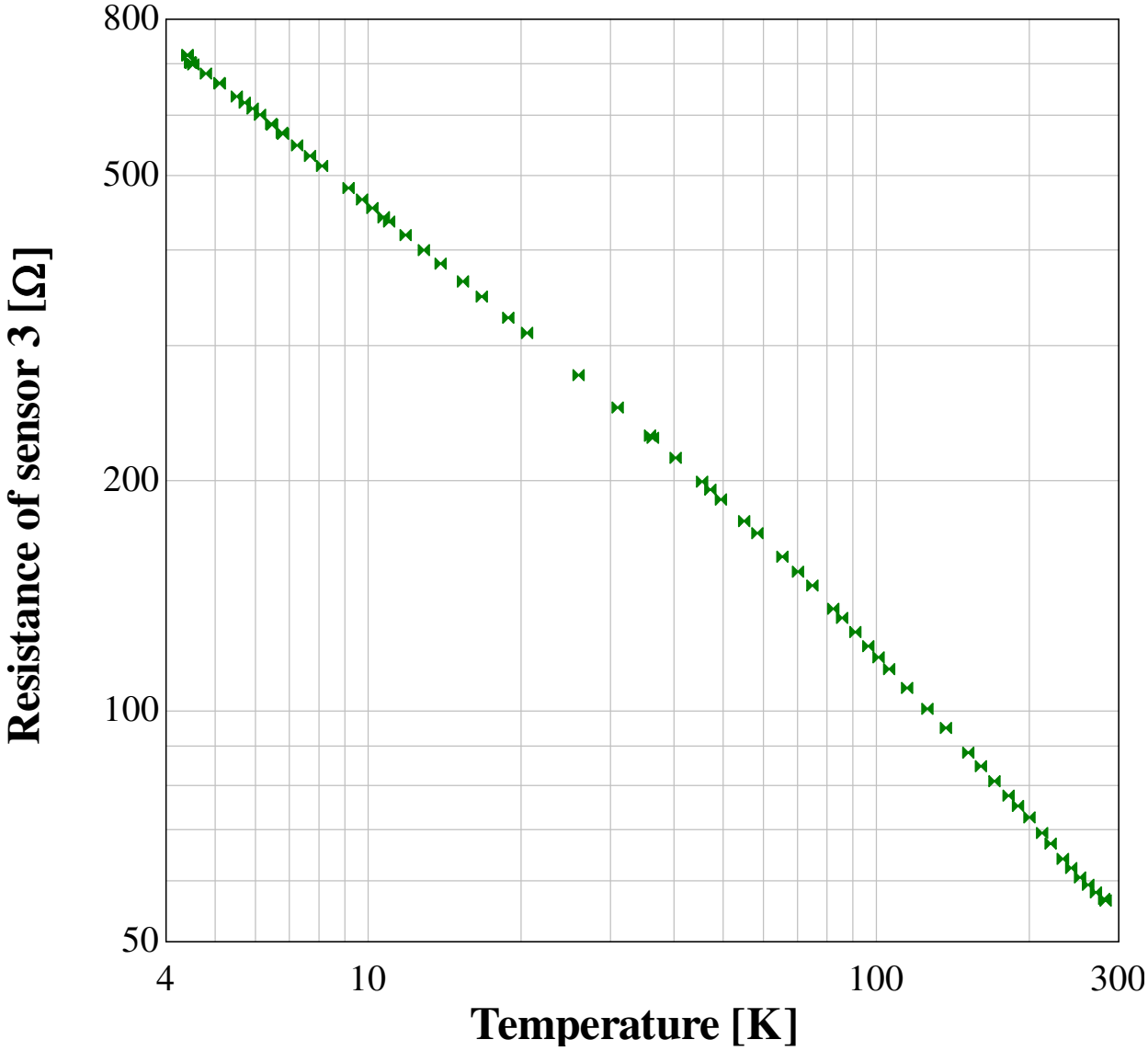

.

Figure 4.8: The calibration curve for the Cernox temperature sensor #3, showing resistance as a function of temperature.

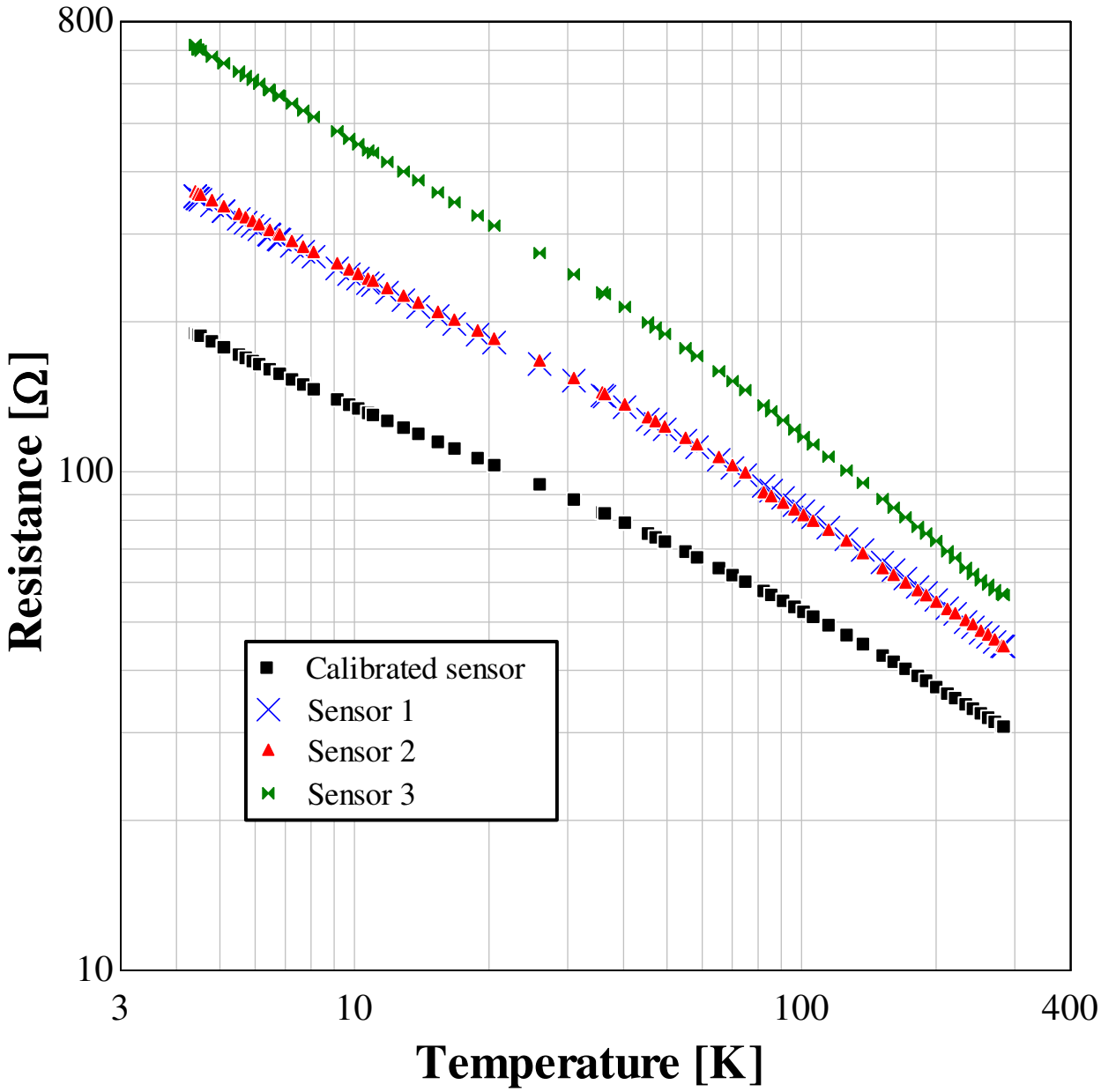

Figure 4.9: The calibration curve for all three non-calibrated sensors compared to the Cernox temperature sensor that was calibrated from the manufacturer between 4.2 K and 300 K.

4.3 Test Run Using Copper and Stainless Steel

A test run needed to be performed using the experiment in order to verify that it was capable of measuring the time required for energy to travel by conduction through materials (i.e., the thermal diffusive time constant). Although the proprietary new regenerator material is needed in order to accomplish the objectives of this project, other materials that have known properties can be used to initially check the equipment. For instance, stainless steel and copper have very different conductivities and specific heats at all temperatures. Therefore, their thermal diffusivities also vary at all temperatures, as shown:

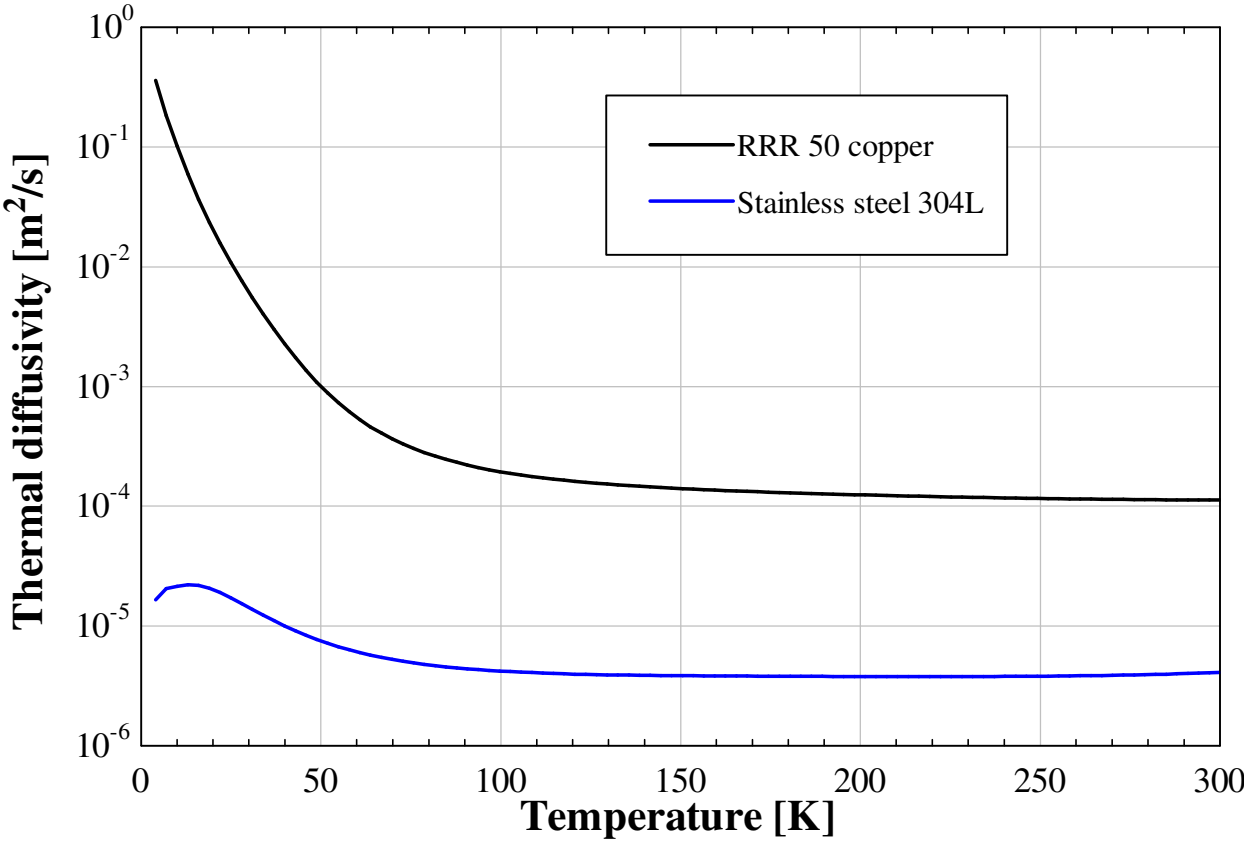

Figure 4.10: The thermal diffusivities of copper RRR 50 and stainless steel 304L as functions of temperature between 4 and 300 K. Note that the thermal diffusivity on the y axis is on a log scale (Marquardt 2012).

If conduction is the only heat transfer mechanism and the conduction process is one dimensional, then the equation from Section 2.3 can be used to estimate response times:

$$t = \frac{\delta^2}{4\alpha} \tag{4.1}$$

where t is the time required for a thermal wave to propagate through the material, δ is the length in the direction of heat flow, and α is the thermal diffusivity of the material. As shown in Figure 4.10, the thermal diffusivity difference exists at every temperature within the range of interest for copper and stainless. Therefore, a test showing a difference in these diffusivities using the facility could be performed at liquid nitrogen temperatures to verify that the experiment can measure time differences without the expense of the liquid helium. The design of the test that was performed is shown in Figure 4.11.

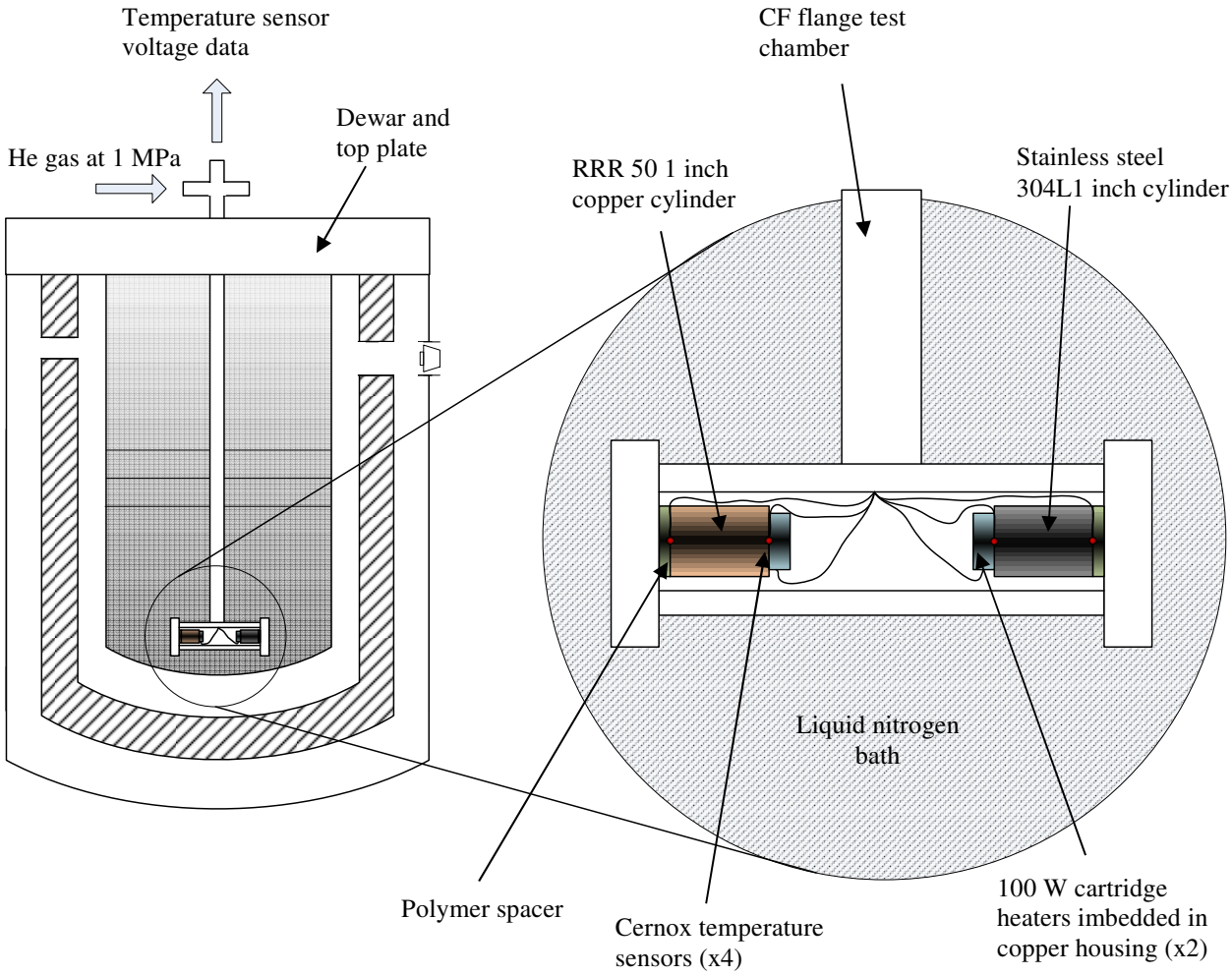

Figure 4.11: The test that was performed to confirm the difference in thermal diffusivities of two well-known materials to verify the experiment and explore its capabilities. Polymer spacers thermally disconnect the test specimens from the 77 K isothermal chamber walls.

There are a few important things to note about the test. The predicted time it takes a thermal wave to travel through one inch of stainless steel 304L at 77 K is approximately 33 seconds. The predicted time it takes a thermal wave to travel through RRR 50 copper at this same temperature is approximately 0.5 seconds. Therefore, the copper should change temperature very quickly and for the stainless there should be a significant time delay before the

side opposite the heater experiences a temperature change. The ratio of the time response of the stainless steel to that of the copper at 77 K is estimated to be around 60.

In the basic mathematical modeling of the regenerator from Section 2, the regenerator is assumed to be much wider than it is long in the test direction. This means the shortest path for heat transfer is in the direction of interest. Although the regenerator test specimen will have layers of silicon that will change temperature nearly instantaneously, the insulating layers of nylon will not have time to interact with the outsides of the cylinder before the heat wave travels completely through the axis of the regenerator. This means that convection will be less of a concern in the actual regenerator test. In the trial test with the stainless steel and copper, the cylinders are longer than they are wide, and therefore convection will be present because heat will reach the outside edges of the cylinder before the thermal wave travels completely through the cylinder. Basically, some energy will be lost as the wave propagates through the material. This could affect the response time and it will affect the temperature rise experienced on the side opposite of the heater.

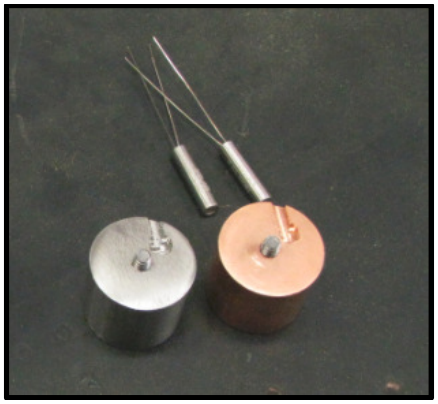

Figure 4.12: This shows the stainless steel 304L and the copper RRR 50 cylinders. Two slots were milled into the cylinders for sensor mounting as can be seen. Threaded rods are visible because the cylinders thread into the sides of the test chamber. The two 100 W Lake Shore cartridge heaters are shown above the metal test cylinders.

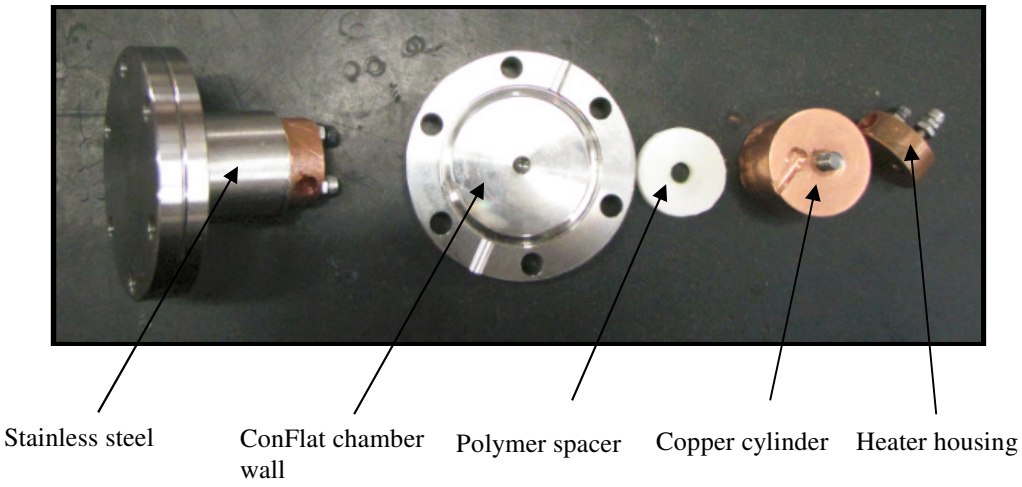

Figure 4.13: This shows the two metal test specimens created as intended in Figure 4.11.

Figure 4.14: The test sample configurations are placed in either end of the chamber for testing.

Figure 4.15: The setup after the two samples have been placed inside of the chamber and before the experiment has been lowered into the Dewar for testing in a liquid nitrogen bath.

A variety of different heat functions were sent through the two metal cylinders and the voltage data of the Cernox temperature sensors were captured by LabVIEW. The copper cylinder had such a high thermal diffusivity that its temperature predictably changed instantly, as shown in Figure 4.16 when 25 V was applied to each of the heaters. The heaters each provided 25 W in this condition.

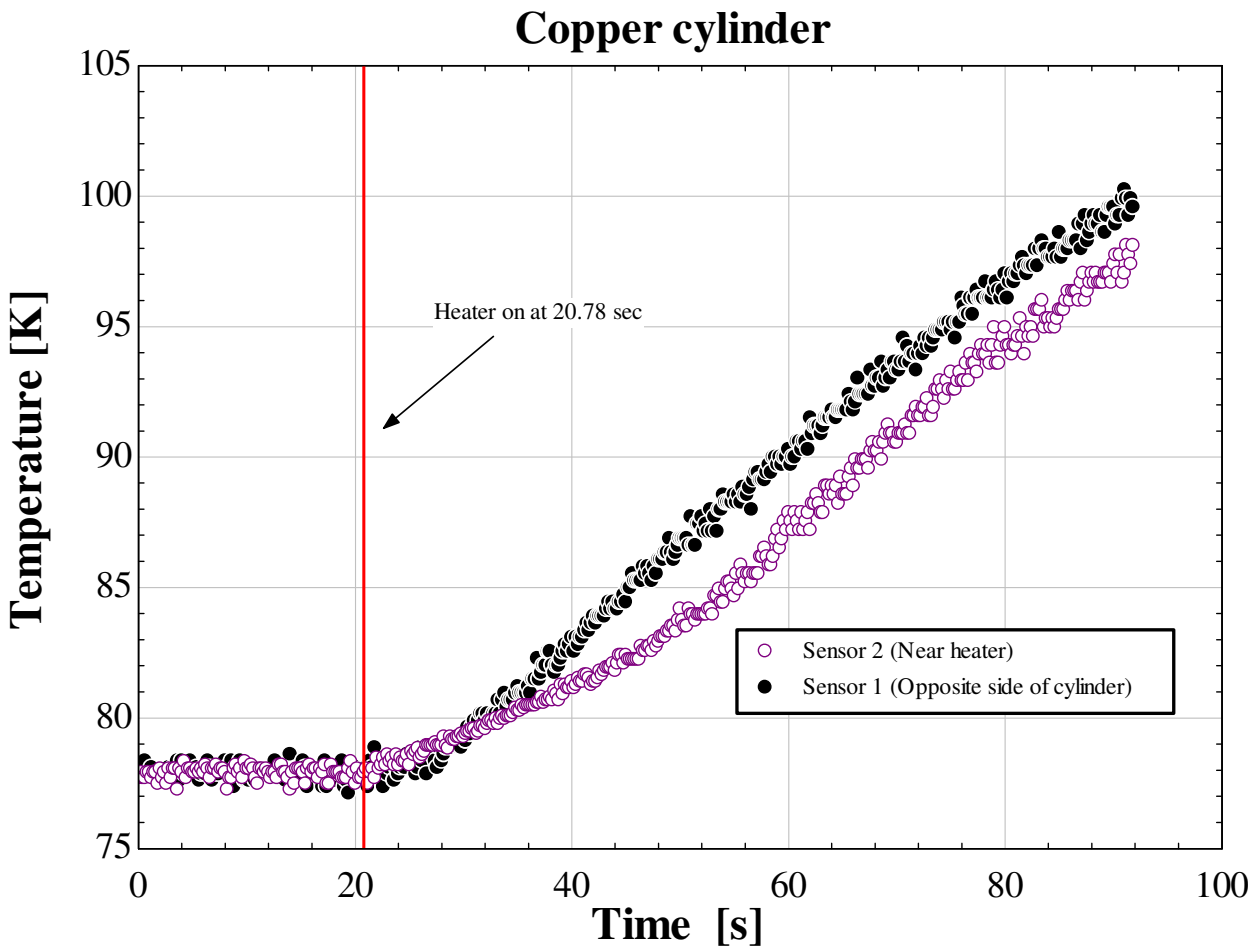

Figure 4.16: The temperature response of the copper cylinder with 25 W of heat applied. Sensor 2 is near the heater and sensor 1 is on the opposite side.

The heater in Figure 4.16 was activated at 20.78 seconds and as can be seen, both sensors changed at nearly the same time. Recall that the predicted thermal diffusive time constant was only 0.5 seconds for the copper piece, therefore a time this small is difficult to measure using the setup. One thing to note is that the temperature of the sensor on the far side of the cylinder from the heater actually reaches higher temperatures than the near side. This is likely due to a poor mounting of sensor 2 near the heater; the contact resistance was higher than the conduction resistance through the cylinder. But, the time response should still be faster for sensor 1 because it has no capacitance associated with it. A magnified plot is necessary to explain this behavior:

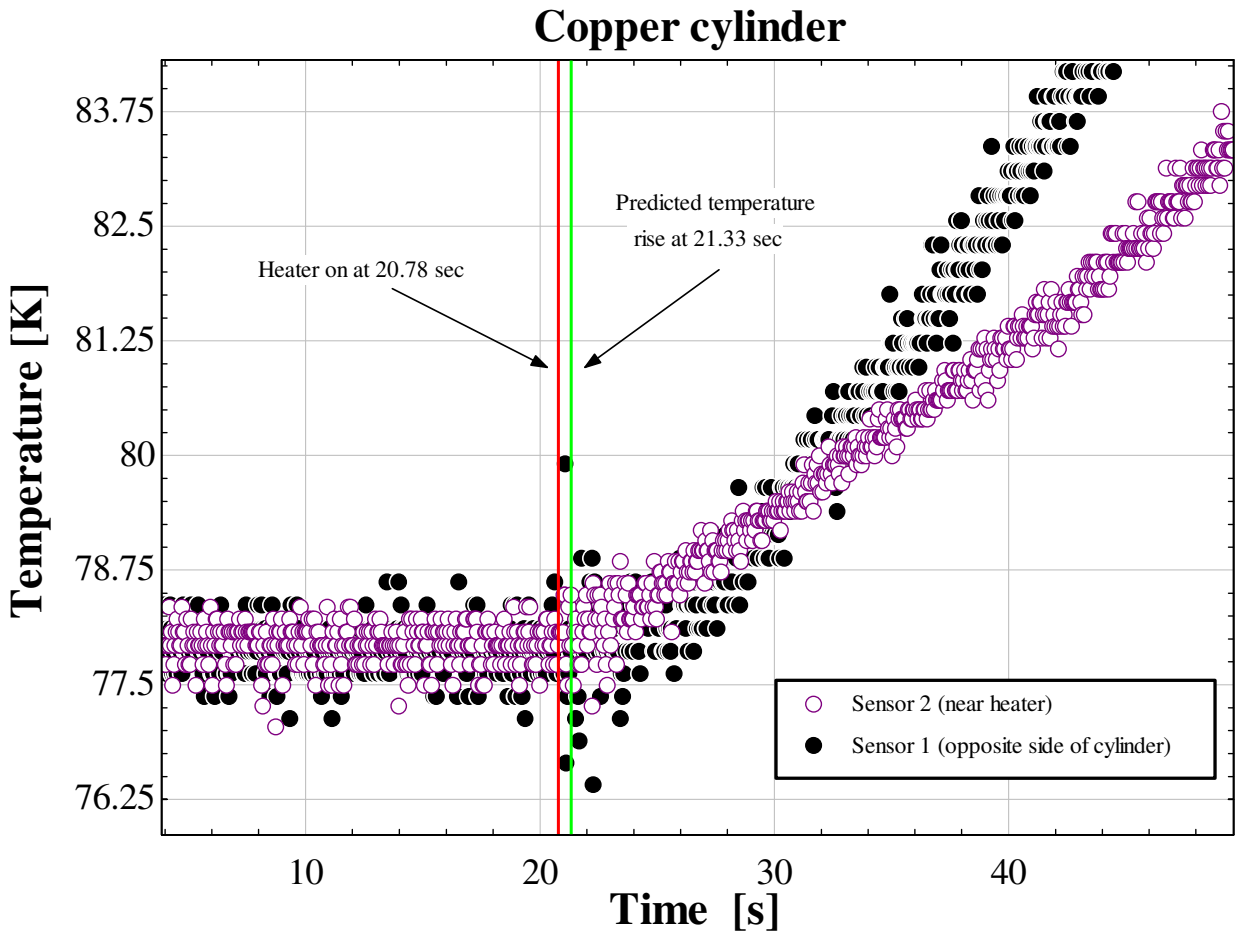

Figure 4.17: A magnified portion from Figure 4.16, showing the temperature rise in the copper cylinder as a function of time.

Figure 4.17 provides useful information that was previously not known. The temperature measurement resolution of the data acquisition is clearly visible. This resolution is approximately 0.05 K. Also, sensor 1 on the opposite side of the cylinder from the heater appears to remain at a lower temperature for a longer period of time, which is expected and confirms the behavior of the time constant. The red line shows where the heater was activated, the green line is the expected time at which the temperature should start to rise. It is evident that the temperature of sensor 2, which is near the heater, begins to change immediately. A plot of the stainless steel with the 25 W heat input is shown in Figure 4.18.

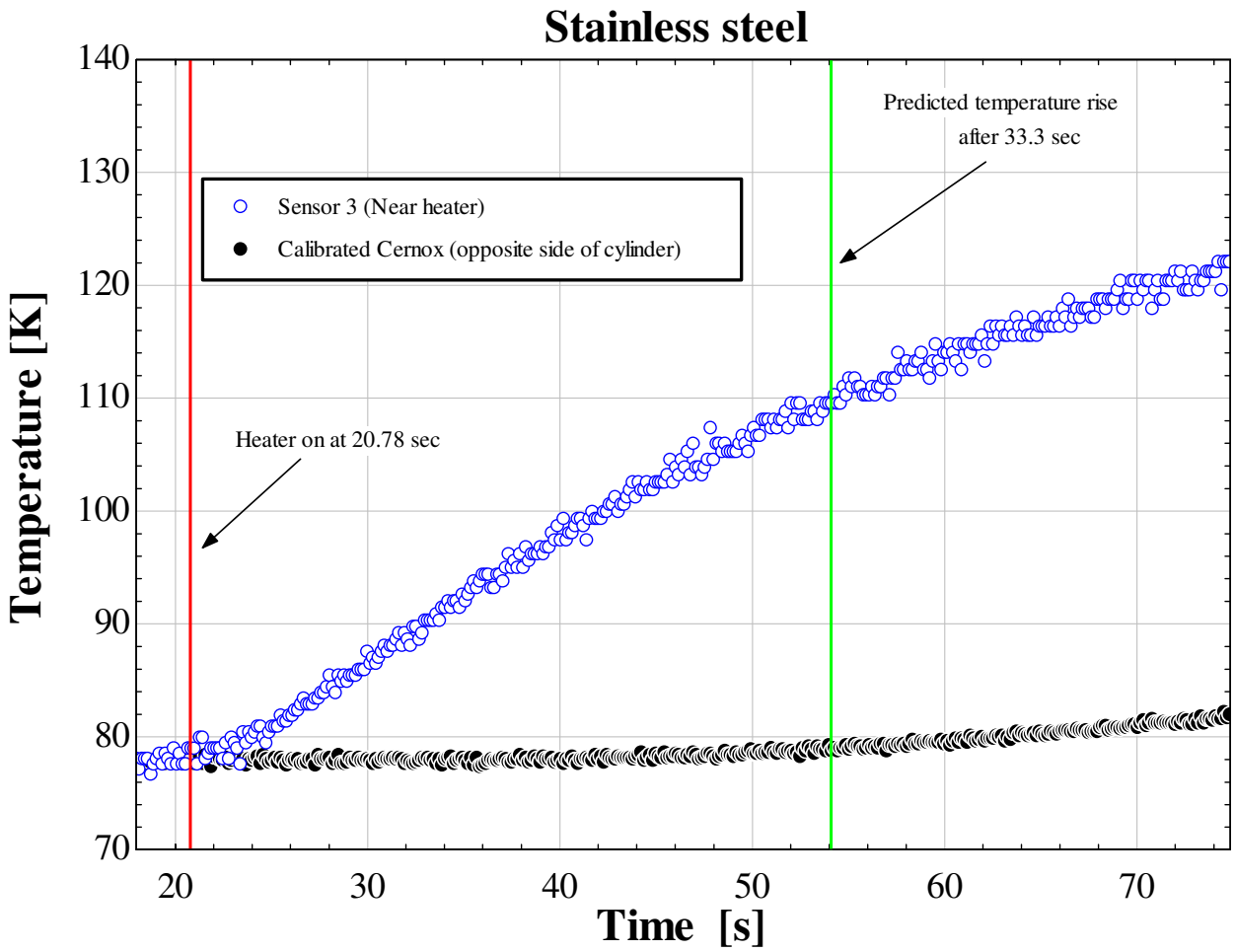

Figure 4.18: The temperature rise in the stainless steel with 25 W of heat applied as a function of time.

As can be seen in Figure 4.18, the side opposite the heater in the stainless steel is not as thermally connected to the heater as it is in the copper case; that is, there is both a large time delay and a much smaller temperature rise occurring than in the copper specimen. Convection from the sides of the cylinder probably influences the temperature rise as discussed previously. In a simple calculation, the resistance to convection from the sides of the cylinder was approximately four times higher than the conduction resistance through one inch of the stainless steel at 77 K, thus convection is certainly not the dominant path for heat. The predicted temperature rise time is shown by the vertical green line in Figure 4.18; the actual temperature

rise does appear to be somewhere around the green line. A plot that allows for a separate y axis for the opposite side of the stainless steel is shown to make analysis of the temperature rise clearer:

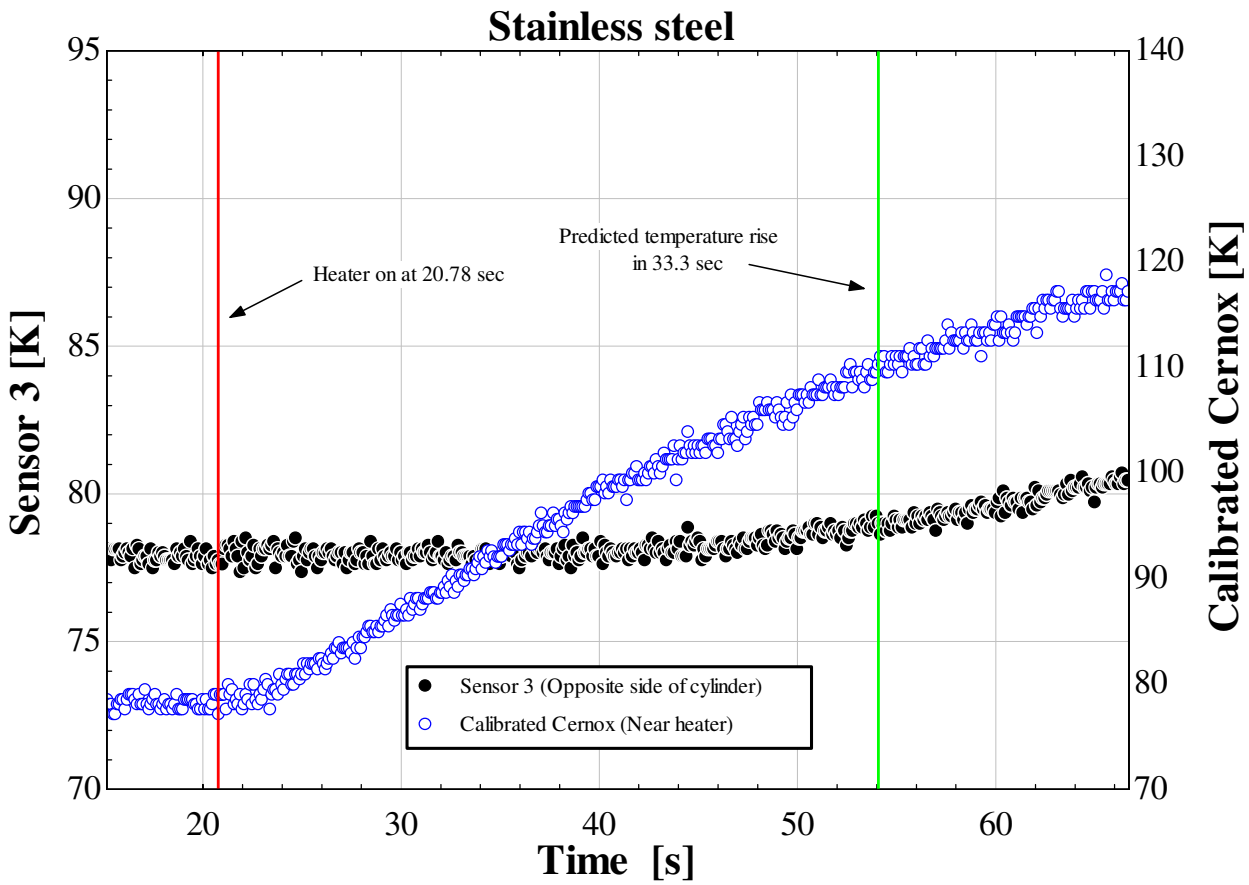

Figure 4.19: The temperature rise in the stainless steel with 25 W of heat provided as a function of time; this is the same information as shown in Figure 4.18. There are separate y axes here for each sensor to make the temperature rise in sensor 3 on the opposite side of the cylinder more visible.

With a basic heating function applied, the voltage resolution for the acquisition system was understood and the ability of the system to capture data at both small times and large times was now confirmed, as shown in Figures 4.16-4.19. More complicated heating functions were subsequently applied to the cylinders in order to explore the capabilities of the sensors. The first new heat function applied was one square wave:

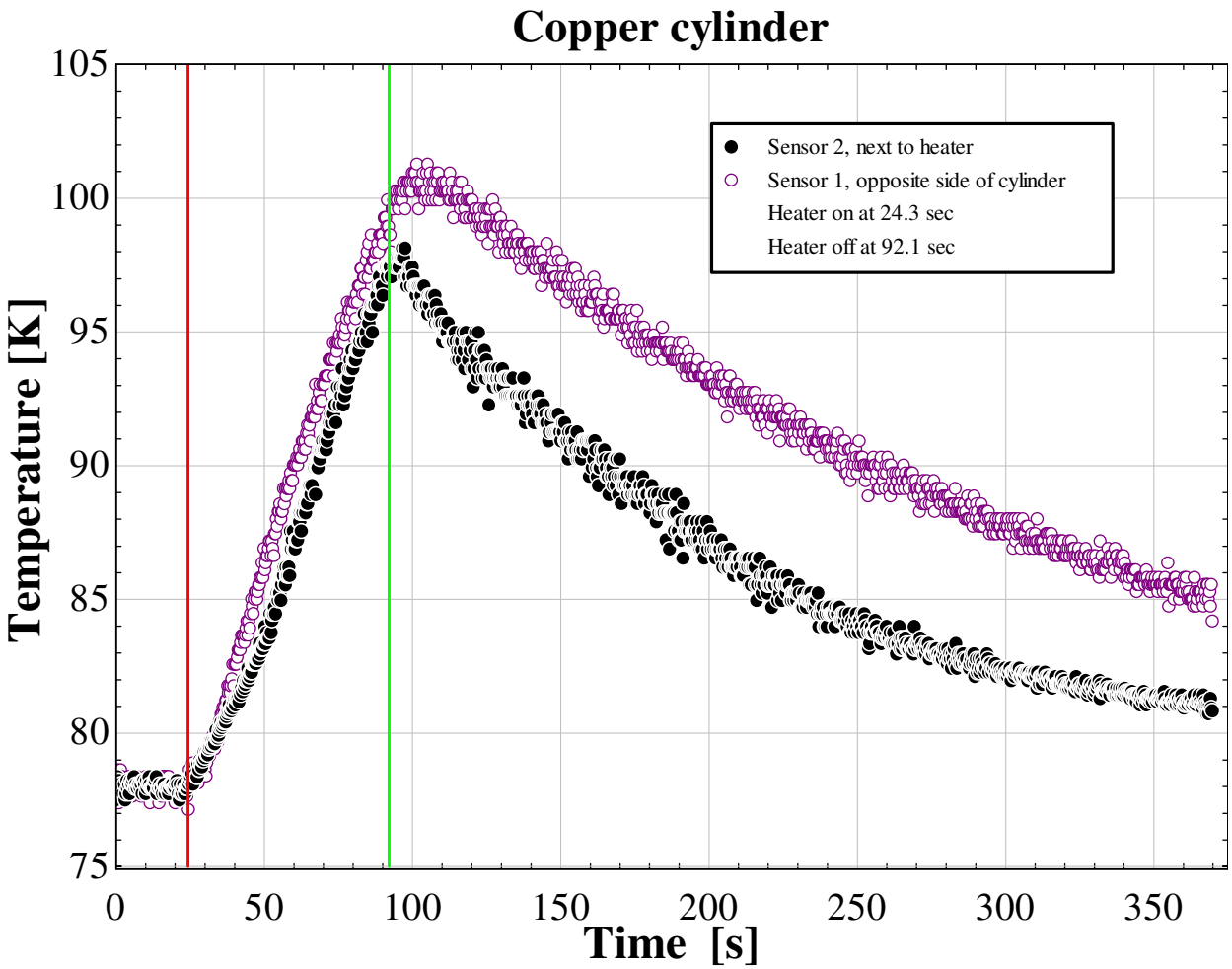

Figure 4.20: The temperature in the copper as a function of time with one square of 25 W heat applied. The heater was activated at 24.3 sec and turned off at 92.1 sec.

Figure 4.20 provides more useful information. The local maximum is noticeable and it is the exact point where temperature changes in the sample after the heater is turned off. As previously discussed in Figure 4.16, temperature rise is actually greater on the opposite side of the cylinder from the heater, probably because of a poorly mounted sensor, but it is clear in Figure 4.20 that sensor 2 still responds faster, as predicted. The approximate time change in the local maxima from each sensor is ~ 2.9 s, which represents the measurement of the thermal diffusive time constant of the copper. Recall that the actual predicted time response was ~0.5 s. The same 25 W square wave was simultaneously applied to the stainless steel cylinder, as shown:

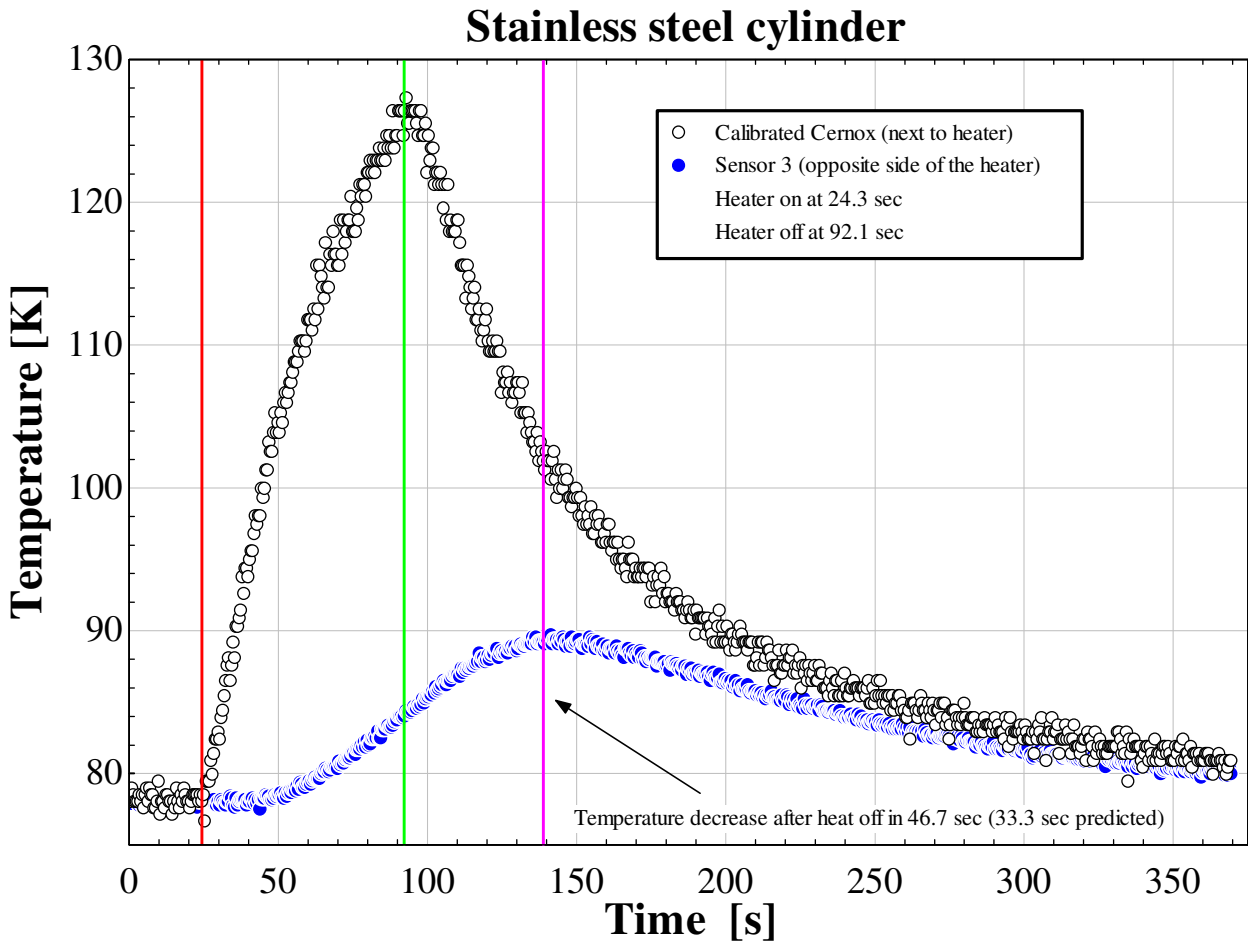

Figure 4.21: This shows the temperature rise and fall in the stainless steel with a 25 W square heat source applied as a function of time.

As can be seen in Figure 4.21, the same analysis of using local maxima to determine the diffusive time constant is useful even with the smaller temperature rise of stainless steel when a square heat wave is applied. By searching the data for the highest temperature experienced, the difference in time between the local maxima for the calibrated Cernox and sensor 3 is 46.7 s, which represents the approximate measurement of the diffusive time constant for the stainless steel. Recall that the predicted time response was 33.3 seconds. The ratio of measured thermal diffusive time constants for the stainless steel and copper is ~16, where the predicted ratio was ~60. To make this ratio closer to the prediction, sensors could have been mounted better and the

time response of the sensors themselves could be subtracted out of the response times. This will be discussed in Section 5. Next, an oscillating square wave of 25 W was applied to both cylinders. The response of the copper is shown:

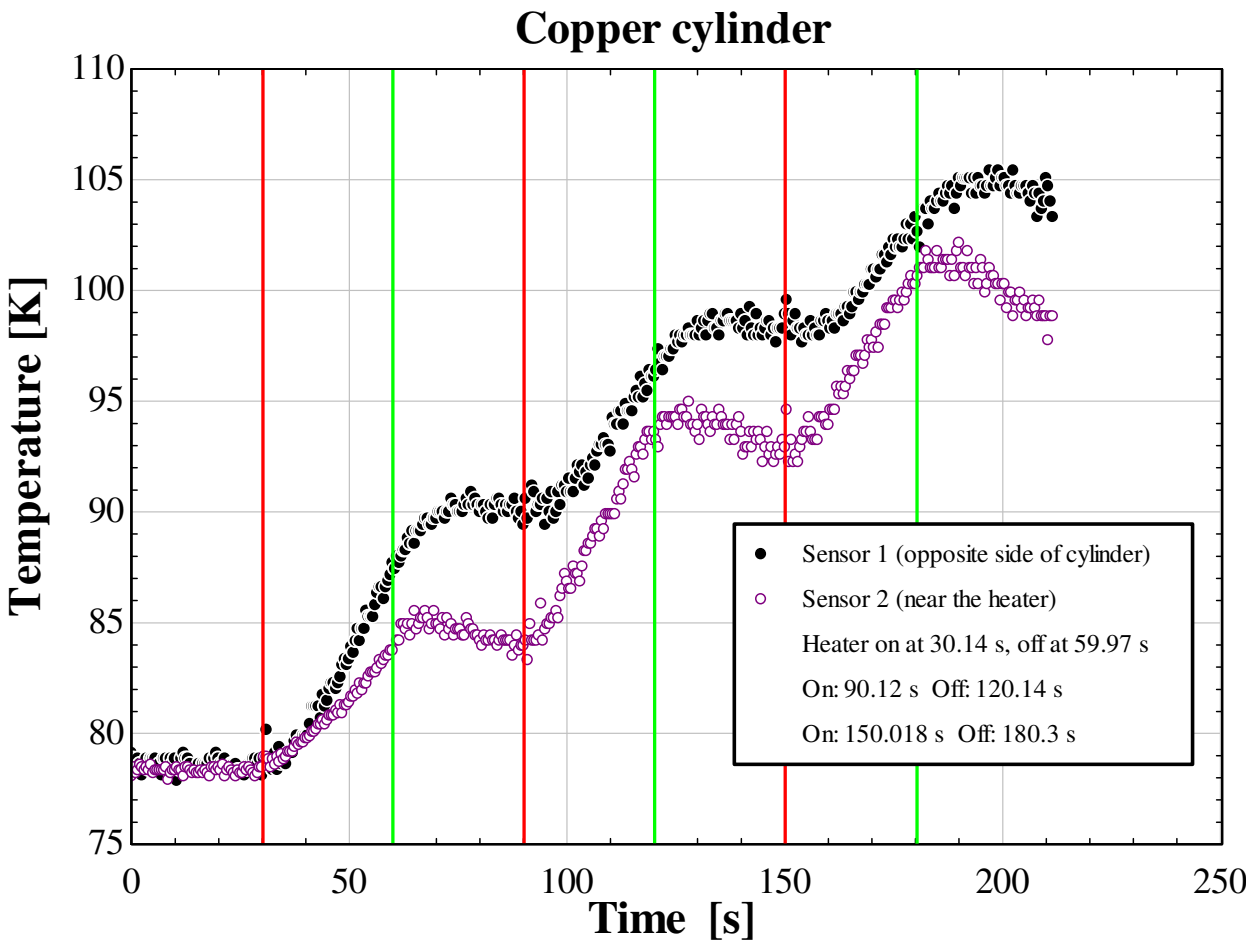

Figure 4.22: The temperature response of the copper cylinder with a 25 W periodic square wave applied at a frequency of approximately 1/min.

It is clear in Figure 4.22 that the opposite side of the cylinder lags behind the side of the cylinder near the heater. But, due to the high thermal diffusivity of the copper, the two sides still respond similarly. A comparison with the stainless steel response is perhaps more useful:

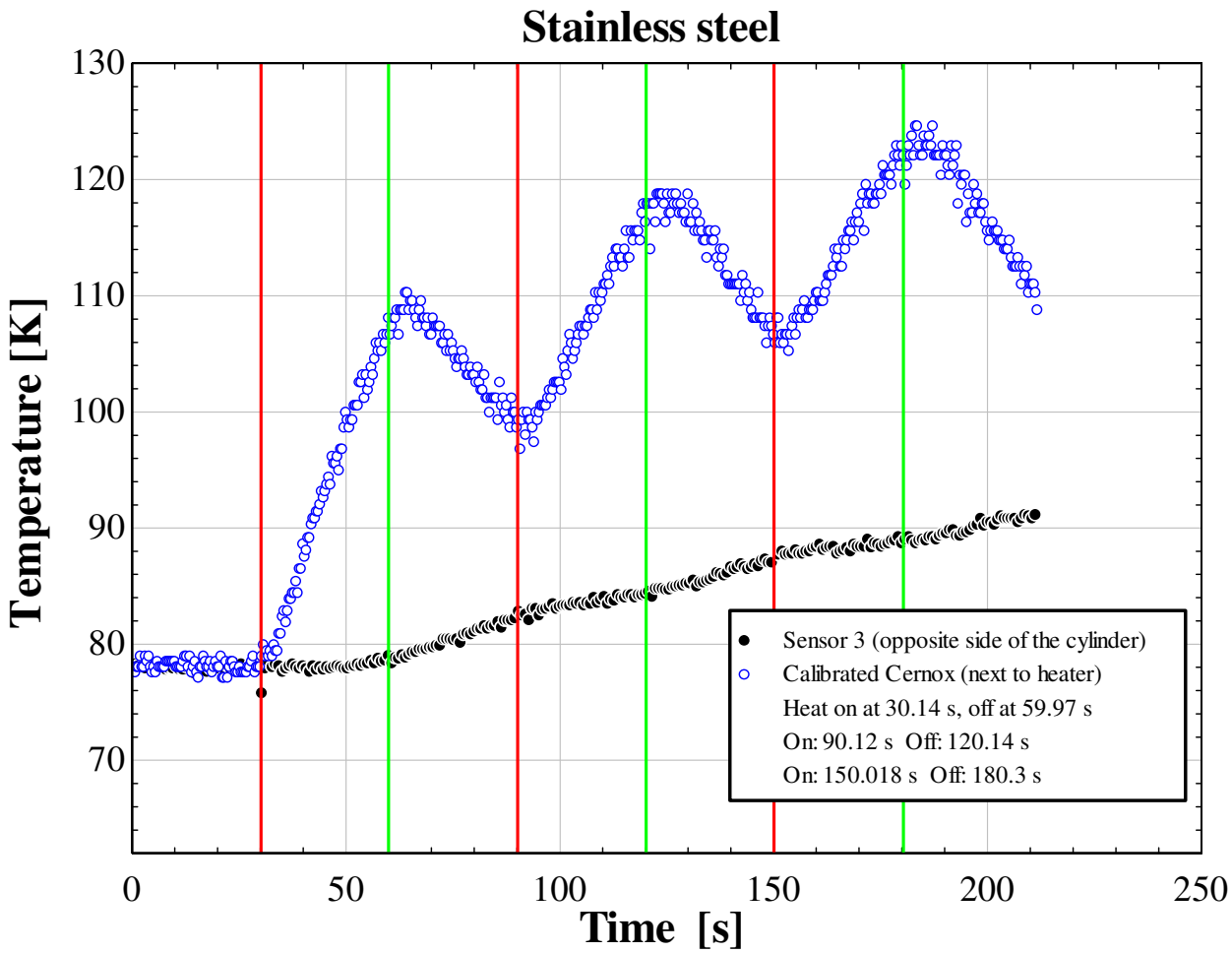

Figure 4.23: The temperature response of the stainless steel with a square heat function of 25 W applied as a function of time.

Figure 4.23 shows that it is difficult to apply a high frequency square wave to something like stainless steel which has a low thermal diffusivity and gain useful information. While the side near the heater responds cyclically as expected, the far side of the cylinder is so far removed from thermal communication that it simply rises in temperature. Recall that it was difficult to obtain useful information for the copper because of its extremely high thermal diffusivity. Therefore, a material with a thermal diffusive time constant somewhere within the range of ~0.5 s and ~33 s would be ideal in the test setup using this frequency of heat. Thermal resistance can

be added in layers as shown in Section 2 to control the diffusive time constant as long as the properties of the spacer material are well known.

The last test lowered the frequency of the square wave function. The temperature response of the copper is once again shown:

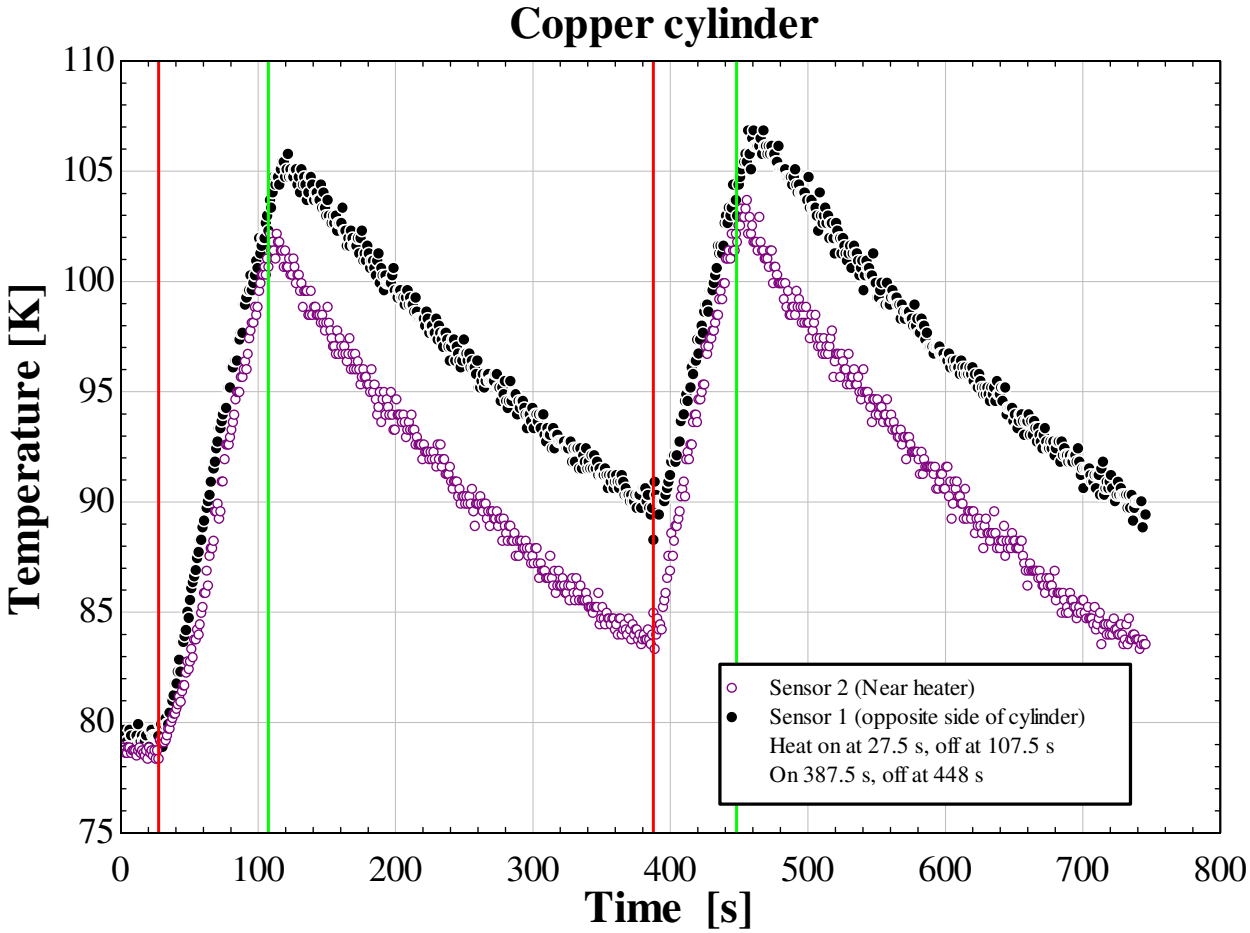

Figure 4.24: The temperature response of the copper with a square wave function of 25 W applied at a frequency of around 1/80 s.

Figure 4.24 is similar to Figure 4.20. Only, in this figure temperature has risen slightly in the second cycle. The delay in the side opposite the heater is clearly visible when the heater is turned off. With a lower frequency than in Figure 4.22, the difference in the temperature behavior is very noticeable. This heat function was applied simultaneously to the stainless steel cylinder and its response is shown:

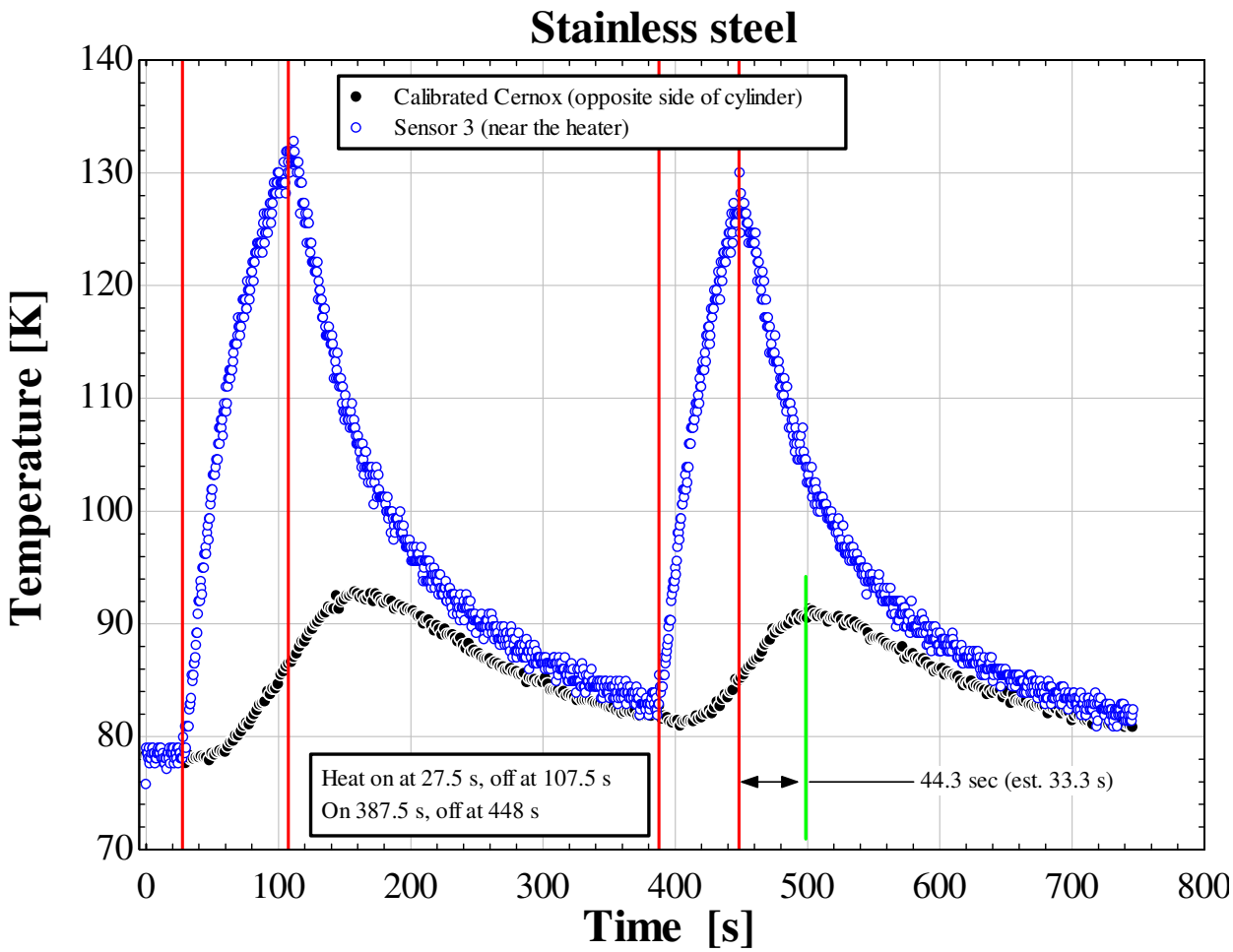

Figure 4.25: The behavior of the stainless steel as a function of time when a square heat wave of 25 W with an approximate frequency of 1/80 s is applied.

Figure 4.25 shows that a cyclic function of heat can be used to generate redundant measurements at each cycle that could be used to calculate an average thermal diffusive time constant over numerous cycles to obtain a more accurate number. As is shown in the figure, the measurement of the thermal diffusive time constant here is approximately 30% higher than the prediction.

As shown in Figures 4.16-4.25, it is evident that the thermal diffusive time constant of the stainless steel is greater, and therefore its thermal diffusivity is much lower, than that of the copper. Although these materials are very different in terms of their high and low thermal diffusivities, it is clear that time differences in a variety of materials could still be measured

using this test setup. Two regenerator materials with diffusive time constants that differ by only a few seconds could be analyzed using this method. Recall the governing equation for the thermal diffusive time constant from Section 2.1:

$$\tau = \frac{\delta^2 \rho c}{k} \tag{4.2}$$

If a poor conductivity spacer is used to control the magnitude of the time response τ, the overall conductivity k in Equation 4.2 will be nearly 100% the conductivity of the spacer. Thus, for two different regenerator samples this k will be the same number. If just the tiny center portion of the novel regenerator is replaced by some other material, ρ will barely change in the equation. A control regenerator material that has a similar density as the new material can be easily found as well, making ρ identical in both cases. δ is the length of the overall sample, which can easily be made the same for both regenerators. The novel regenerator is expected to have a specific heat c that is double or more than a traditional regenerator. Because the nylon and silicon used to hold the new regenerator material have effectively zero heat capacity at low temperatures, the diffusive time constant of a proprietary regenerator could be double that of a control specimen; this is directly attributable to the increase in heat capacity of the new regenerator material, and it can be readily measured in a similar manner as shown in Figures 4.16-4.25 in a liquid helium bath. This is the intention of the facility once the proprietary material is obtained.

References

[1] Barron, R.F. (1985). *Cryogenic Systems.* New York, NY: Oxford University Press, Inc.

[2] *Cryogenic Reference Tables.* 2004, Lake Shore Cryogenics, Inc.

[3] Nellis, G. and Klein, S.A., (2009). *Heat Transfer.* New York, NY: Cambridge University Press.

[4] Klein, S.A. (2012). Engineering Equation Solver [Computer Software]. Madison, WI: F-Chart Software.

[5] Marquardt, E.D., Le, J.P., and Radebaugh, Ray, *Cryogenic Material Properties Database.* 2000, Boulder, CO: National Institute of Standards and Technology.

5 Conclusions

5.1 Conclusions and Recommendations

The results described in Section 4 show that differences in thermal diffusivity can be measured using the setup. However, the thermal diffusivity calculated from the measurements for stainless steel was off by around 30% from the expected value. This error could result from a few different sources. First, the heater power was high at 25 W. The temperature near the heater was 130 K and on the side opposite of the heater the temperature was only 90 K; this is a 40 K difference created by the heater. The thermal diffusive time constant analysis was performed assuming constant temperature at the heater surface; in reality, this temperature was constantly increasing and energy had to be continuously transferred from the heater to the thermal wave front. This movement in energy is not instantaneous, and the thermal diffusivity through steel decreases as temperature increases, as shown in Figure 5.1.

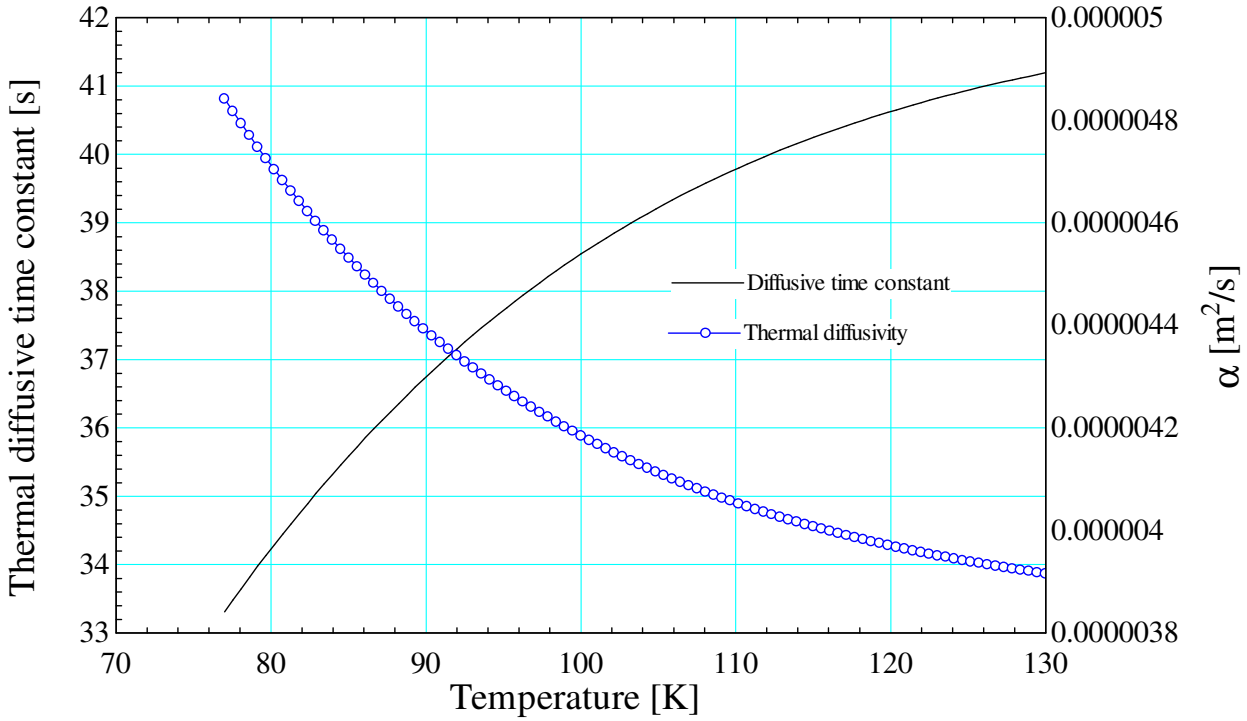

Figure 5.1: The thermal diffusive time constant and the thermal diffusivity of stainless steel 304L as a function of temperature.

With a smaller temperature rise on the heater-side of the test specimen, the diffusive time constant should be closer to the expected value. As shown in Figure 5.1, as greater temperatures occur in the stainless steel, the time constant in the figure becomes closer to the measured time constant from Section 4. Therefore, the heating should be reduced by some factor for the future runs; perhaps by a factor of five.

Another factor that may have influenced the results of the test runs was suggested in Section 4. The cylinders were much longer than they were wide, meaning that the resistance to conduction from the heater to the side of the cylinder was less than the resistance from the heater to the opposite end of the cylinder. This resistance network is shown in Figure 5.2.

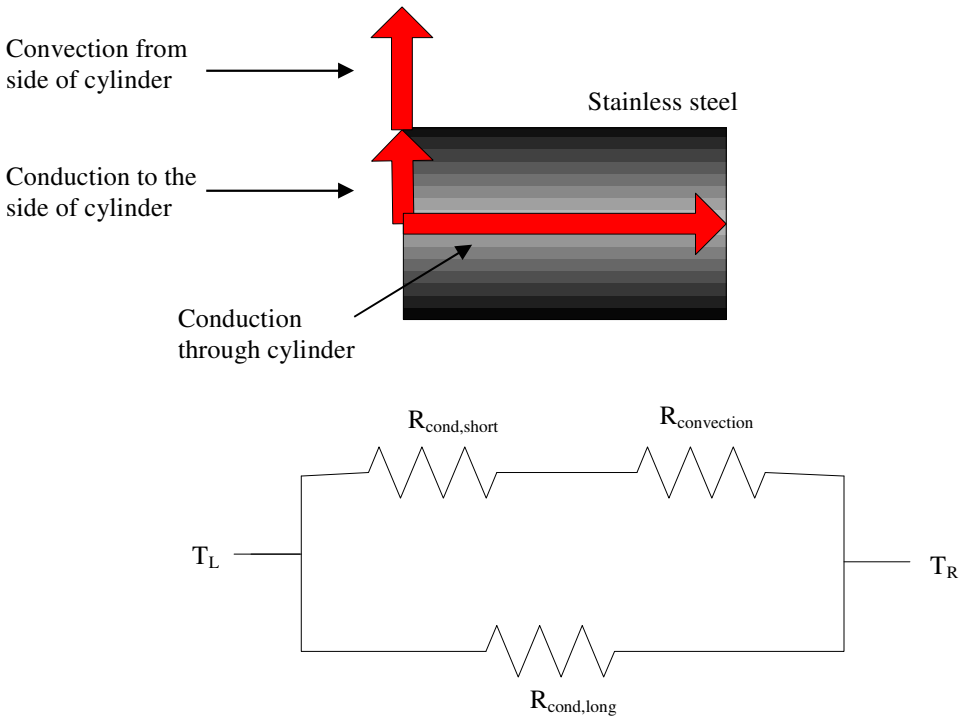

Figure 5.2: The resistant network for heat in the stainless steel.

As shown in Figure 5.2, the conduction path to the outside of the cylinder is much shorter than through the cylinder, which could influence the behavior of the thermal propagation. In a simple model using an average temperature for the stainless steel of 110 K in a medium of liquid nitrogen, the conduction resistance through the cylinder is $R_{cond,long}$ = 3.6 K/W. The resistance to the outside edge of the cylinder is approximately $R_{cond,short}$ = 1.8 K/W. The convection resistance is $R_{convection}$ = 31.2 K/W. Therefore, the combined resistances of the conduction to the side of the cylinder and convection are approximately 9 times higher than conduction through the cylinder, suggesting that heat loss due to convection is not a major concern. However, it still could be an influence on the temperature rise time. For future test runs the sample should be made with a radius that is larger than its length, ensuring that the shortest possible heat transfer path is through the axis of the cylinder.

Cernox sensors with the SD package were mounted by using over-sized washers on bolts combined with Apiezon-M grease to facilitate a better thermal contact. Although theoretically this is an adequate way to mount sensors, it is not convenient to assemble or disassemble components using this method. A better method of fastening the sensors is shown in Figure 5.3.

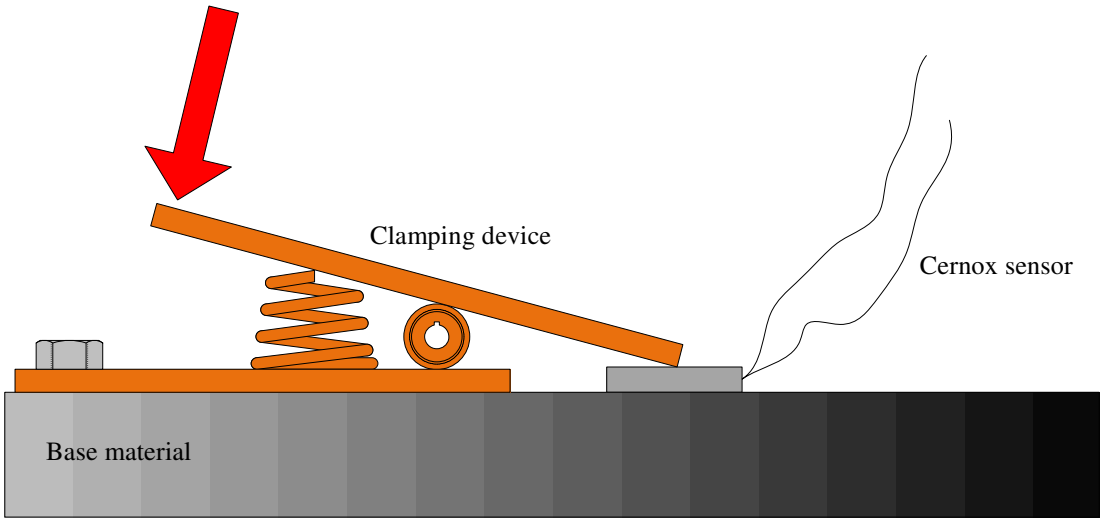

Figure 5.3: A clamping device used to mount a Cernox temperature sensor.

A clamping device as shown in Figure 5.3 would be a much better way to mount sensors because the clamping force is known and sensors can be easily connected and disconnected. In the figure, a bolt is shown that holds the clamp to the base material, but in reality many different methods could be used to attach the clamp. Another benefit of using this method is the tiny contact surface between the clamp and the Cernox sensor, reducing heat transfer between these parts.

The flash method for measuring thermal diffusivity is similar to the thermal diffusive method of this experiment, and it should be analyzed in more detail. The flash method and its associated mathematical theory allow predictions of thermal diffusivities given temperature rise times. The equations are slightly different than the ones presented in Section 2. For example, the

method in this experiment to measure thermal diffusivity uses the relation shown in Equation 5.1.

$$\alpha = \frac{L^2}{4t} \tag{5.1}$$

where α is the thermal diffusivity, L is the length of the material, and t is thermal diffusive time constant from Section 2. The flash method uses a similar function to measure thermal diffusivity as shown in Equation 5.2.

$$\alpha = \frac{1.38 L^2}{\pi^2 t_{\frac{1}{2}}} \tag{5.2}$$

where $t_{1/2}$ represents half the time it takes to reach the steady state temperature rise created by the heater (Parker 1961). In the previous tests, this half rise time was not measured, but it easily could be with more trials to compare the flash method to the thermal diffusive method. Since thermal diffusivities of common materials are known, both methods can be verified.

More inclusive models of the system can be constructed. To establish estimates for the proprietary system's behavior, many geometry simplifications were made and the entire regenerator was assumed adiabatic as discussed in Section 2. A 2-D or 3-D finite element analysis could be performed that included temperature dependent properties and accounted for convection from the sides of a composite material. A model could be constructed that incorporated a periodic forcing function to investigate phase lag between a heat function and the response of the opposite side of the material being measured; complex combination would work well here. The solution could be compared to measurements made in the lab using a function generator for the heater.

The electronics in the experiment could use an upgrade. Although the data acquisition has been adequate thus far, a higher resolution and more accurate system might be required for future

test runs. The current LabVIEW card, the basic and entry-level PCI-6221, can lose its calibration in a year; it is estimated to be ten years old. An oscilloscope with a signal generator that can be amplified to provide voltage to the heaters could also be useful, serving as a periodic forcing function.

Obtaining the proprietary material, then running the experiment at liquid helium temperatures is the most important future task. Resistive spacers might have to be added to the test sample before inserting it into the test chamber, but functionally the facility is capable of measuring the samples. With each experimental run, many data sets can be taken. If a difference in thermal diffusivity of the test sample and a control exists, this facility should be capable of measuring it. Using the model discussed in this thesis, and hopefully better ones developed in the future, thermal diffusivity can be inferred from the test data. Specific heat can be calculated from the diffusivity measurement provided that the conductivity and density are known. The method outlined in this thesis can be used to verify and quantitatively show a higher heat capacity in new types of regenerators.

References

[1] Parker, W. J., et.al., 1961, *Flash Method of Determining Thermal Diffusivity, Heat Capacity, and Thermal Conductivity*. Journal of Applied Physics, 32:9.

Appendix A

Cernox temperature sensor calibration data:

Cernox Sensor 1

Temperature (K)	Resistance (Ω)
4.405	357.3
4.405	357.2
4.41	356.9
4.456	354
4.472	353.3
4.525	351.5
4.797	342.6
5.097	333.5
5.104	333.3
5.515	321.6
5.714	316.3
5.919	311.5
6.127	306.5
6.441	299.7
6.47	299
6.759	293
6.801	292.3
7.243	284.1
7.683	276.6
8.112	270.1
9.155	256.2
9.731	249.4
10.19	244.3
10.73	239
11	236.7
11.84	229
12.88	221.2
13.89	214.3
15.37	205.4
16.74	198.2
18.85	188.6
20.55	181.9
25.96	164.6
30.97	152.4

Cernox Sensor 2

Temperature (K)	Resistance (Ω)
4.405	365.3
4.405	365.2
4.41	365.1
4.456	361.8
4.472	361.4
4.525	359.5
4.797	350.5
5.097	341.4
5.104	341
5.515	329.2
5.714	323.8
5.919	318.8
6.127	313.7
6.441	306.6
6.47	305.9
6.759	299.9
6.801	299.1
7.243	290.6
7.683	282.9
8.112	276.2
9.155	261.9
9.731	254.8
10.19	249.6
10.73	244.1
11	241.7
11.84	233.8
12.88	225.7
13.89	218.6
15.37	209.5
16.74	202
18.85	192.1
20.55	185.1
25.96	167.3
30.97	154.3

35.88	142.4
36.31	141.6
40.25	134.8
45.37	127.3
47.16	124.8
49.47	121.9
55.01	115.5
58.39	112.1
65.38	105.8
70.16	101.9
74.89	98.49
82.3	93.77
85.61	91.73
90.93	88.74
96.45	85.76
101.1	83.46
106.1	81.1
115	77.4
126.1	73.3
137.1	69.79
151.8	65.8
160.7	63.57
170.9	61.14
182	58.82
190	57.18
200.4	55.4
212.1	53.32
220.7	51.92
233	49.97
242	48.82
251.9	47.55
261.4	46.69
270.8	45.63
281	44.71
283	44.63

35.88	144.2
36.31	143.4
40.25	136.6
45.37	128.8
47.16	126.3
49.47	123.3
55.01	117
58.39	113.6
65.38	107.1
70.16	103.2
74.89	99.73
82.3	91.04
85.61	89.38
90.93	86.71
96.45	84.05
101.1	81.96
106.1	79.84
115	76.55
126.1	72.83
137.1	68.71
151.8	64.1
160.7	62.17
170.9	60.03
182	57.95
190	56.58
200.4	54.9
212.1	53.09
220.7	52.07
233	50.49
242	49.45
251.9	48.03
261.4	47.21
270.8	46.11
281	44.85
283	44.72

Cernox Sensor 3

Temperature (K)	Resistance (Ω)
4.405	718.5
4.405	718.3
4.41	718.1
4.456	703.1
4.472	702.2
4.525	698.5
4.797	679.9
5.097	660.6
5.104	659.8
5.515	634.6
5.714	622.6
5.919	611.8
6.127	600.3
6.441	584.5
6.47	582.8
6.759	568.9
6.801	567.2
7.243	547.9
7.683	530.3
8.112	514.9
9.155	481.9
9.731	465.7
10.19	453.7
10.73	441.3
11	435.7
11.84	418.1
12.88	399.8
13.89	384
15.37	363.8
16.74	347.4
18.85	326.4
20.55	311.7
25.96	274.5
30.97	249.1
35.88	229
36.31	227.3
40.25	214.1

Calibrated Cernox

Temperature (K)	Resistance (Ω)
4.405	189.8
4.405	189.8
4.41	189.7
4.456	188.8
4.472	188.5
4.525	187.5
4.797	182.7
5.097	177.9
5.104	177.8
5.515	171.8
5.714	169.2
5.919	166.7
6.127	164.3
6.441	160.9
6.47	160.6
6.759	157.7
6.801	157.3
7.243	153.3
7.683	149.7
8.112	146.5
9.155	139.7
9.731	136.4
10.19	134
10.73	131.4
11	130.2
11.84	126.6
12.88	122.7
13.89	119.3
15.37	114.9
16.74	111.3
18.85	106.5
20.55	103.1
25.96	94.33
30.97	88
35.88	82.92
36.31	82.51
40.25	79.05

45.37	199.4
47.16	194.6
49.47	188.9
55.01	177
58.39	170.7
65.38	159.1
70.16	152
74.89	145.9
82.3	136
85.61	132.2
90.93	126.8
96.45	121.5
101.1	117.5
106.1	113.4
115	107.2
126.1	100.6
137.1	95.07
151.8	88.22
160.7	84.77
170.9	81.04
182	77.58
190	75.22
200.4	72.64
212.1	69.33
220.7	67.16
233	64.15
242	62.38
251.9	60.62
261.4	59.34
270.8	57.95
281	56.86
283	56.58

45.37	75.17
47.16	73.94
49.47	72.43
55.01	69.17
58.39	67.38
65.38	64.09
70.16	62.08
74.89	60.27
82.3	57.73
85.61	56.68
90.93	55.11
96.45	53.6
101.1	52.4
106.1	51.21
115	49.24
126.1	47.06
137.1	45.13
151.8	42.84
160.7	41.6
170.9	40.28
182	38.97
190	38.09
200.4	37.03
212.1	35.93
220.7	35.17
233	34.17
242	33.49
251.9	32.78
261.4	32.15
270.8	31.55
281	30.94
283	30.83